

Dissertation  
submitted to the  
Combined Faculties for the Natural Sciences and for Mathematics  
of the Ruperto-Carola University of Heidelberg, Germany  
for the degree of  
Doctor of the Natural Sciences

Put forward by

**Dipl.-Phys. Claude Krantz**  
born in Luxembourg

Oral examination: 28th October 2009



**Intense Electron Beams from  
GaAs Photocathodes as a Tool for  
Molecular and Atomic Physics**

Claude Krantz

Referees:

Prof. Dr. Andreas Wolf  
Prof. Dr. Thomas Stöhlker



**Elektronenstrahlen hoher Intensität aus GaAs Photokathoden als Werkzeug der Molekül- und Atomphysik** — Cäsium-beschichtete GaAs Photokathoden werden als Quellen quasi-monoenergetischer Elektronenstrahlen in der Atom- und Molekülphysik vorgestellt. Im Langzeitbetrieb des Elektronen-Targets des Ionenspeicherrings TSR in Heidelberg konnten kalte Elektronenstrahlen stetig höherer Intensität und Zuverlässigkeit produziert werden. Durch gezielte Unterdrückung von Prozessen, die zur Verminderung der Quanteneffizienz führen, konnte der Extraktionsstrom – bei Kathodenlebensdauern von 24 h oder länger – auf über 1 mA erhöht werden. Die Vorzüge des kalten Elektronenstrahls bezüglich Elektronenkühlung und Elektron-Ion Rekombinationsexperimenten werden diskutiert. Dedierte Experimente zeigen, dass sowohl Kühlkraft als auch Energieauflösung des Photoelektronenstrahls einem thermisch erzeugten Strahl deutlich überlegen sind. Das Langzeitverhalten der GaAs-Kristalle, insbesondere bezüglich wiederholter Oberflächenreinigung mittels Wasserstoffradikalen, konnte untersucht werden. Ein Aufbau zur Elektronen-Emissions-Spektroskopie wurde der Präparationskammer am Elektronen-Target hinzugefügt. Diese Messapparatur erlaubte unter anderem, Untersuchungen an GaAs-Photokathoden durchzuführen, die zu einer neuartigen Anwendung letzterer als stabile Elektronenemitter im ultravioletten Spektralbereich führten. Der Prototyp einer auf diesem Prinzip basierenden Elektronenkanone zur Verwendung an der HITRAP-Anlage der GSI wurde konstruiert und erfolgreich in Betrieb genommen.

**Intense Electron Beams from GaAs Photocathodes as a Tool for Molecular and Atomic Physics** — We present cesium-coated GaAs photocathodes as reliable sources of intense, quasi-monoenergetic electron beams in atomic and molecular physics experiments. In long-time operation of the Electron Target of the ion storage ring TSR in Heidelberg, cold electron beams could be realised at steadily improving intensity and reliability. Minimisation of processes degrading the quantum efficiency allowed to increase the extractable current to more than 1 mA at usable cathode lifetimes of 24 h or more. The benefits of the cold electron beam with respect to its application to electron cooling and electron-ion recombination experiments are discussed. Benchmark experiments demonstrate the superior cooling force and energy resolution of the photoelectron beam compared to its thermionic counterparts. The long period of operation allowed to study the long-time behaviour of the GaAs samples during multiple usage cycles at the Electron Target and repeated in-vacuum surface cleaning by atomic hydrogen exposure. An electron emission spectroscopy setup has been implemented at the photocathode preparation chamber of the Electron Target. Among others, this new facility opened the way to a novel application of GaAs (Cs) photocathodes as robust, ultraviolet-driven electron emitters. Based on this principle, a prototype of an electron gun, designed for implementation at the HITRAP setup at GSI, has been built and taken into operation successfully.



Intense Electron Beams from GaAs Photocathodes  
as a Tool for Molecular and Atomic Physics

Claude Krantz



# Contents

<b>1</b>	<b>Introduction</b>	<b>1</b>
<b>2</b>	<b>GaAs Semiconductor Photocathodes</b>	<b>5</b>
2.1	Electron Emitters . . . . .	5
2.1.1	Field Emitters . . . . .	6
2.1.2	Thermionic Cathodes . . . . .	6
2.1.3	Photocathodes . . . . .	7
2.2	Negative Electron Affinity . . . . .	7
2.3	Handling of NEA Photocathodes . . . . .	9
2.3.1	Cathode Activation . . . . .	11
2.3.2	Cathode Lifetime . . . . .	13
2.3.3	Surface Cleaning . . . . .	14
2.4	Spectral Response . . . . .	16
2.5	GaAs Photocathodes in PEA Regime . . . . .	18
<b>3</b>	<b>The Photoelectron Target of the TSR</b>	<b>23</b>
3.1	The Electron Target . . . . .	23
3.2	Photocathode Setup . . . . .	26

3.2.1	Photoelectron Gun Chamber . . . . .	27
3.2.2	Cathode Preparation Chamber . . . . .	31
3.2.3	Cathode Loading and Atomic Hydrogen Chambers . . . . .	34
3.3	Photocathode Currents and Lifetimes . . . . .	36
3.3.1	Lifetime-limiting Effects . . . . .	36
3.3.2	Electron Target Beam Performance . . . . .	44
3.4	Long-Time Photocathode Behaviour . . . . .	48
3.4.1	Atomic Hydrogen Cleaning . . . . .	48
3.4.2	Calibration of the Atomic Hydrogen Source . . . . .	50
3.4.3	Spectroscopic Diagnostics of the Cleaning Procedure . . . . .	54
3.4.4	Stability of the GaAs Crystals . . . . .	56
<b>4</b>	<b>Merged-Beam Physics with Cold Electrons</b>	<b>61</b>
4.1	Electron Beam Temperature . . . . .	61
4.1.1	Statistical Energy Distribution . . . . .	62
4.1.2	Temperatures of Magnetised Beams . . . . .	63
4.1.3	Plasma Relaxation Effects . . . . .	67
4.1.4	Space-Charge Induced Velocity Distribution . . . . .	69
4.1.5	Misalignment Effects . . . . .	70
4.2	Low-Temperature Electron Cooling . . . . .	72
4.2.1	The Binary Collision Model . . . . .	72
4.2.2	Relaxation Time . . . . .	75
4.2.3	Electron Cooling of Slow Molecular Ions . . . . .	76
4.2.4	CF <sup>+</sup> as a Benchmark for Low-Energy Electron Cooling . . . . .	78

<i>CONTENTS</i>	iii
4.3 Electron-Ion Recombination Experiments . . . . .	84
4.3.1 Recombination at Low Collision Velocity . . . . .	86
4.3.2 Merged-Beams Energy Resolution . . . . .	87
4.3.3 Dielectronic Recombination of $F^{6+}$ . . . . .	90
4.4 Discussion . . . . .	96
<b>5 A Robust Pulsed Electron Source for HITRAP</b>	<b>99</b>
5.1 The HITRAP Facility . . . . .	99
5.2 The Electron Source . . . . .	101
5.2.1 Electric Considerations . . . . .	102
5.2.2 Electron Gun Design . . . . .	103
5.3 Tests of the Electron Gun Prototype . . . . .	106
5.3.1 Spectral Response . . . . .	106
5.3.2 Pulsed Operation . . . . .	109
5.4 Outlook . . . . .	112
<b>6 Summary</b>	<b>115</b>
<b>Bibliography</b>	<b>119</b>
<b>Acknowledgements</b>	<b>129</b>



# Chapter 1

## Introduction

For decades, electron beams have been valuable tools in atomic, molecular, nuclear and particle physics. Discovered as early as in the late 19th century, scientific interest in applications of the “cathode rays” is today more widespread than ever before. The electron is the prototype of a fundamental fermion. Hence, electron beam experiments have contributed to virtually all milestones of particle physics. Featuring the lowest mass among all charged particles, electrons are also ideal sources of high-energetic photons as produced in synchrotron radiation facilities or Free Electron Lasers. Collision experiments between electrons and other particles, atoms or molecules profit from the fact that electron beams can be produced relatively easily in an incomparably broad energetic spectrum, spreading from fractions of an electronvolt to hundreds of kiloelectronvolts. That is, obviously, not taking into account high-energy accelerators which produce electrons of energies still higher by many orders of magnitudes. This versatility and ease of use has established electron beams as standard projectiles used in atomic impact ionisation and excitation spectrometry. Electron Beam Ion Traps are extreme examples of this technique: Here, an ion plasma is trapped in the space charge potential of an intense, high-energetic electron beam, which leads to production of highly charged ions via multiple ionisation and allows to measure atomic transition energies inaccessible to classical optical spectroscopy.

Electron cooler ion storage rings embrace the same principle of mixing a single-pass electron beam with a stored ion plasma, but at zero or near-zero collision velocity between electrons and ions. “Electron cooling” means that heat is exchanged between the hot stored ion beam and a single-pass electron beam, which overlap in a dedicated beam-merging section of the storage ring. Originally developed as a technique to enhance the brilliance of proton colliders, electron coolers have evolved into valuable tools for atomic and molecular physics.

Facilities like the Test Storage Ring (TSR) of the Max-Planck-Institute for Nuclear Physics (MPIK) allow to cool, store and study atomic and molecular ion species under well-controlled conditions. Besides their application to ion cooling, electron beam merging sections can serve as electron *targets* if the velocity of the electrons is detuned with respect to that of the ions. In doing so, such merged-beam devices allow the generation of very low electron-ion collision energies in the order of 1 meV, which is not achievable in a systematically controlled way for laboratory-frame experiments. Reactions between electron and ions at such low energy play important roles in astrophysics. Ionisation balances in low-temperature plasmas of highly charged atomic ions and electrons are important input parameters for astrophysical models of media surrounding active galactic nuclei or novae [Sav03]. Molecular ions are known to drive the chemistry of cold interstellar clouds [Kre05]. Hence, their production and destruction rates by interaction with slow electrons play key roles in the chemical evolution of the cloud matter.

Both the efficiency of electron cooling and the energy resolution that can be achieved in electron-ion collision experiments crucially depend on the intensity and the velocity spread of the electron beam. Hence, significant efforts haven been undertaken, at the MPIK and elsewhere, to produce cold and intense electron cooler beams. While elaborate beam optics can reduce the temperature of the electron plasma in the rest frame of the ion beam, its temperature is defined thermodynamically by that of the cathode from which the electrons are extracted. Typically, electron beams used in merged-beam setups are produced by thermionic cathodes. While the latter are devices of proven reliability, they have to be heated to operational temperatures of normally (1000...1200) K. Hence, electron beams produced by conventional electron coolers have typical initial energy spreads of approximately 100 meV.

The use of colder electron sources, in particular photocathodes, opens up a large potential regarding lower beam temperatures, provided competitive emission currents and operational reliability can be achieved. Thus, for the dedicated Electron Target section of the TSR, an electron gun based on emission from Negative Electron Affinity GaAs semiconductor photocathodes has been designed in previous works [Pas96, Wei04]. Cooled to temperatures of (100...150) K by liquid nitrogen, the GaAs photocathodes emit electron beams of initial kinetic energy spreads that are at least ten times lower compared to thermionic cathodes [Orl04]. In this work, we present the first long-time operation of this new photoelectron gun, which has replaced its thermionic counterpart in 2006 and has been employed in a total of 25 experimental runs since.

Traditionally, electron-cooling has been applied to ion beams of relatively high charge-to-mass ratio as found e.g. in highly charged atomic ions. Extension of the

merged beams technique to large molecular ions is presently underway. Electron cooling of these beams is particularly challenging as the low charge-to-mass ratio of molecular ions severely reduces the electron cooling force. In addition, the low revolution velocity of these ions in the storage ring limits the available electron current density. Due to their high temperature, electron cooling of heavy molecular ions using standard thermionic cathodes is practically impossible. Especially for the Cryogenic Storage Ring presently under construction at the MPIK, designed to store large organic molecules at very low velocities, a cold electron source will be a strict necessity for successful application of electron cooling.

Besides their low electron beam temperature, photocathodes have the benefit of being able to operate in vacuum-critical environments. In contrast to thermionic emission, photoexcitation of electrons is possible without significant heating of the emitter material or any surrounding surfaces. While field-emitting cathodes provide the same vacuum-neutrality, their emission current is often severely limited at experimentally accessible extraction voltages. This work describes the development of a reliable electron gun based on the same semiconductor GaAs photocathodes as used in the TSR Electron Target. This source is able to emit intense electron pulses at low cathode voltages and will be used for electron filling of the Cooler Penning Trap of the HITRAP setup that is presently in construction at the Helmholtz Centre for Heavy Ion Research (GSI).

The upcoming chapter 2 of this text introduces the basic concepts of GaAs photocathodes. Special emphasis is placed on the state of Negative Electron Affinity (NEA) into which GaAs photocathodes can be prepared by deposition of a dipole layer of cesium and oxygen onto their surface. The experimental techniques involved in cleaning the GaAs surface as well as in application of the (Cs,O) layer are considered fundamental for the later chapters and are thus also introduced at this early stage. NEA is introduced as a way to obtain cryogenic cathodes of high quantum efficiency and narrow electron energy spread. Electron emission spectroscopy is presented as a versatile tool for diagnostics of the surface conditions of GaAs photocathodes. Analysis of the surface spectral response leads us to the use of GaAs as photocathodes of reduced Positive Electron Affinity (PEA). It is shown that, in this state, GaAs semiconductor cathodes can be operated as reliable, ultraviolet-driven electron sources. We demonstrate that the quantum efficiencies of PEA GaAs cathodes can be higher by at least one order of magnitude compared to metal photocathodes.

Chapter 3 is devoted to the photocathode setup as it is implemented at the TSR Electron Target section. We give a detailed description of the operation of the latter using GaAs photocathode electron sources. During this work, performance and reliability of the photoelectron beam have been improved significantly. We describe

how quantum efficiency degradation mechanisms limiting the usable photocathode lifetime have been isolated and brought under control, resulting in an enhanced maximum density and a much-improved overall availability of the photoelectron beam to TSR experiments. The atomic hydrogen photocathode cleaning facility, whose implementation has already been described in [Wei04], has been calibrated and its operational parameters have been optimised using spectral response diagnostics of the photocathode surfaces. The long-time operation of the photocathode setup allowed to study the effects of repeated atomic hydrogen exposure on the achievable quantum efficiency of the GaAs photocathodes.

Chapter 4 showcases the benefits offered by a cold photoelectron beam in merged-beam applications. We show that cold electron beams are a necessity for efficient cooling of slow molecular ions in the storage ring. Electron cooling experiments performed on a slow  $\text{CF}^+$  ion beam demonstrate the superior cooling force of the photoelectron beam compared to thermionic beam of the TSR's Electron Cooler. Furthermore, we show how the lower temperature of the Photoelectron Target enhances the energy resolution of the setup in low-energy electron-ion collision experiments.

Finally, chapter 5 introduces a novel application of the GaAs photocathodes as robust, ultraviolet-driven pulsed electron sources. Motivated by the behaviour of GaAs photocathodes in the PEA regime, as discussed in chapter 2 and studied experimentally at the TSR setup, a GaAs based pulsed electron source has been developed for implementation at the HITRAP Cooler Penning Trap facility at GSI. In contrast to NEA operation at the TSR Electron Target, the PEA photoelectron gun is designed to operate maintenance-free over periods of several months. In this work, a prototype of the pulsed electron gun has been built and taken into operation. We show that the design achieves the bunch intensity necessary for efficient electron filling of the Cooler Trap. Furthermore, we provide evidence for good stability of the PEA quantum efficiency as required for successful long-time operation of the electron source.

# Chapter 2

## GaAs Semiconductor Photocathodes

The upcoming chapter provides the basic principles of GaAs semiconductor photocathodes. In the TSR's Electron Target, the cathodes are used in a state referred to as *effective Negative Electron Affinity* (NEA). We thus dedicate a section to the description of the latter. A subsequent section gives an overview of the experimental techniques involved in the operation of GaAs-based NEA photocathodes in both reflection and transmission mode illumination, with special emphasis on the NEA activation and GaAs surface cleaning procedures. Photoelectron emission spectroscopy as implemented in our experimental setup is a powerful tool regarding optimisation of these surface preparation techniques as well as in studies of photocathode robustness against residual-gas-induced degradation processes. Finally, we discuss the behaviour of GaAs photocathodes in the regime of *positive* electron affinity which leads to a novel application of GaAs as a robust UV-driven electron emitter.

### 2.1 Electron Emitters

An electron emitting cathode constitutes the main element of any electron gun. In order to unbind electrons from the cathode material and allow them to populate positive eigenstates in the vacuum, they have to be given the ability to overcome a characteristic potential barrier referred to as the *workfunction*  $\Phi$  of the material. The workfunction is defined as the difference between the lowest unbound continuum level and the Fermi energy of the cathode material.

### 2.1.1 Field Emitters

Application of very strong ( $> 10^9$  V/m) electric fields at the surface of the cathode material reduces the workfunction potential step to a thin barrier, allowing electrons to escape to the continuum via the tunnelling effect. Field Emitting Arrays (FEA) work in this regime. The required high extraction fields are generated by structuring the cathode surface as a lattice of microscopically sharp spikes. However, the macroscopic current density extractable at low and medium cathode voltages is severely limited [Pff01]. Even for FEAs operated at room temperature, the nanostructured surface efficiently adsorbs residual gas, which reduces the electric extraction fields. Operation of FEAs at high electron currents therefore requires at least periodic heating of the cathode to high temperatures in order to remove residual gas pollution from its surface.

The standard techniques for production of *intense* DC electron beams thus do not rely on the tunnelling effect alone, but involve an energy supply to the cathode electrons which is at least equal to the workfunction, thus classically allowing the particle to pass the potential barrier separating it from the vacuum.

### 2.1.2 Thermionic Cathodes

The most widely used technique for the production of electron beams is thermionic emission. Energy is transferred to the free electrons of a metal cathode by heating the latter. As the temperature rises the electron energy distribution stretches to higher and higher values. At sufficiently high temperature, a significant part of the electrons' Fermi distribution lies above the workfunction threshold  $\Phi$ , allowing part of the electron population to escape from the solid. The current density  $j$  that can be extracted from a thermionic cathode is given by Richardson's Law

$$j = A_G T^2 \exp\left(-\frac{\Phi}{k_B T}\right), \quad (2.1)$$

where  $T$  is the cathode temperature,  $k_B$  Boltzmann's Constant, and  $A_G$  a characteristic parameter of the cathode material.

Thermionic cathodes can reliably deliver very high current densities. For modern cathodes, employing specialised compound metal oxides as emitter materials, workfunctions can be as low as  $\Phi \approx 1.5$  eV. Yet the emitters have to be heated to temperatures of 1200 K or above in order to emit significant electron current densities [Spr04]. This is a drawback for applications requiring low electron energy spreads. An electron temperature of 1200 K corresponds to a kinetic energy spread

of the emitted electron gas of approximately 100 meV. This thermodynamically limits the monochromaticity of the electron beam which can be produced by such a cathode.

### 2.1.3 Photocathodes

In a photocathode, electrons overcome the workfunction by absorbing photons of an energy  $\hbar\omega \geq \Phi$ . The advantage of photoemission is that no heating of the emitter material is necessary, which allows the generation of electron beams of low energy spread. While photoelectron emission is possible from simple metal surfaces at sufficiently high photon energies, semiconductor photocathodes based on GaAs or related materials have become the standard emitters used in electron guns designed to produce cold and intense DC electron beams [Sin06, Bar07, Or104, All95].

## 2.2 Negative Electron Affinity

In 1965, Scheer and van Laar discovered that coating of a *p*-doped GaAs surface with a monolayer of cesium and oxygen leads to a surface state referred to as *effective Negative Electron Affinity* (NEA) [Sch65]. This state allows the extraction of thermalised electrons from the *p*-GaAs crystal. The principle of NEA electron emission is illustrated in figure 2.1.

At room temperature, GaAs is characterised by a gap energy  $E_{\text{gap}}$  of 1.42 eV, defined as the difference in energy of the lowest conduction band state  $E_{\text{cb}}$  and the highest valence band state  $E_{\text{vb}}$ . Heavy *p*-doping of GaAs with zinc at densities of  $n_{\text{p}} \sim 5 \cdot 10^{18} \text{ cm}^{-3}$  lowers the Fermi energy to closely above the valence band maximum  $E_{\text{vb}}$  [Mil73].

By absorbing photons of energy  $\hbar\omega \geq E_{\text{gap}}$  electrons are promoted from the valence band to the conduction band. By emission of phonons and scattering with heavy holes, the excited electrons thermalise quickly to the bottom of the conduction band [Spi77]. The thermal relaxation time is of  $10^{-12}$  to  $10^{-13}$  s, while an electron's lifetime in the conduction band is typically of the order of nanoseconds. Although electrons can recombine with holes from the valence band, either radiatively under emission of photoluminescence photons, or non-radiatively by multi-step deexcitation through in-gap states created by crystal defects, the diffusion length of thermalised electrons is typically several  $\mu\text{m}$ . For a thin crystal it is thus likely that electrons excited and thermalised within the *p*-GaAs bulk reach the crystal surface. The energies of these electrons populate a Boltzmann distribution defined by the

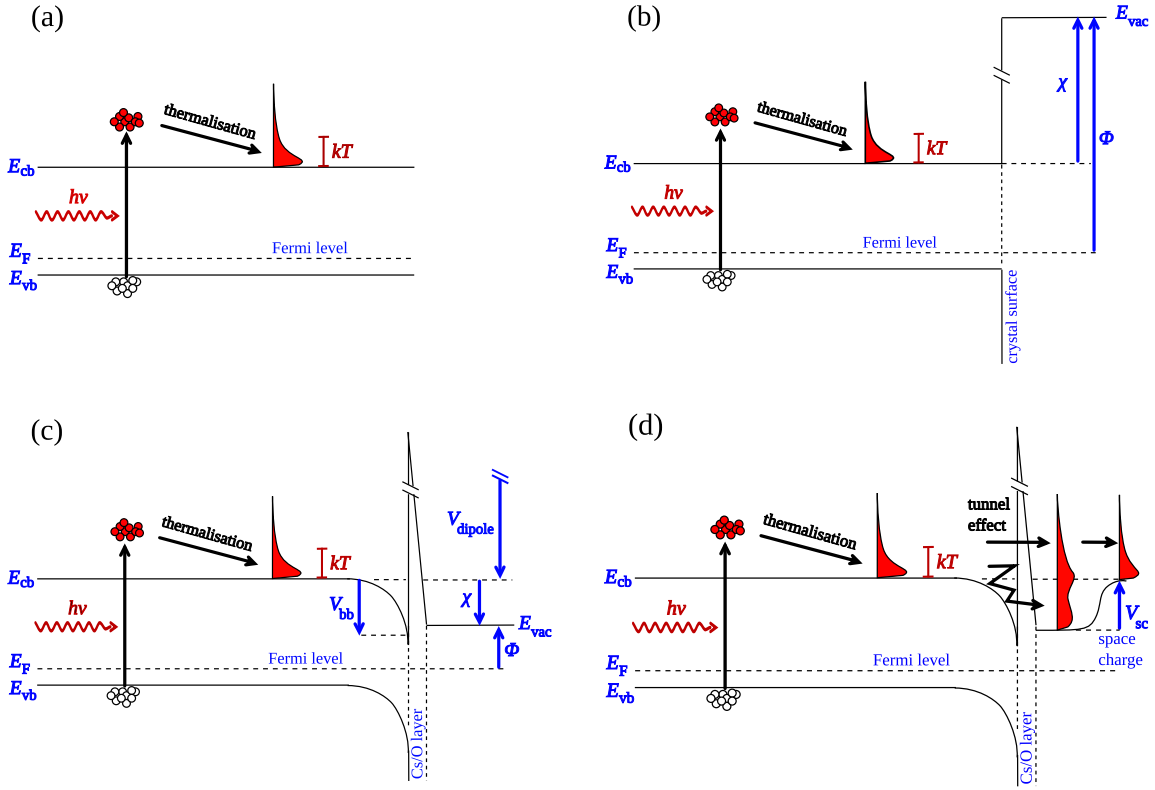


**Figure 2.1:** Electron emission from a NEA  $p$ -GaAs photocathode. (a) Photoexcitation to the conduction band and subsequent thermalisation. (b) The electron affinity  $\chi$  separates the vacuum level  $E_{vac}$  from the conduction band minimum  $E_{cb}$ . (c) A Cs/O monolayer on the  $p$ -GaAs surface effectively lowers  $E_{vac}$  below  $E_{cb}$ , forming a state of Negative Electron Affinity. (d) Electrons escape by tunnelling. Scattering initially broadens the energy distribution, but the space charge potential  $V_{sc}$  prohibits the emission of very slow electrons.

temperature of the GaAs lattice which can be as low as 77 K for a crystal cooled by liquid nitrogen.

The potential difference between the vacuum level and the bottom of the conduction band is referred to as *Electron Affinity*  $\chi$ . For a pure GaAs crystal,  $\chi$  amounts to about 4 eV. Deposition of an atomic layer of cesium and oxygen on the surface of  $p$ -doped GaAs effectively reduces the electron affinity down to negative values with respect to the valence band minimum in the crystal bulk [Sch65, Alp95]. The effect of the (Cs,O) layer is twofold. As the alkaline Cs atoms are electron donors, some of them contribute their valence electron to the GaAs crystal bulk. The positive charge associated with the ionic remnants leads to a downwards bending of both the conduction and the valence band by an amount of  $V_{bb} \approx (0.3 \dots 0.5)$  eV at the GaAs surface [Drou85, Alp95]. Thus, the band bending by itself is not sufficient to reduce the vacuum energy to the level of the conduction band minimum. However, ionisation of a relatively small fraction of the Cs atoms is sufficient to lower

their electronic states below the Fermi level in the GaAs bulk, prohibiting further electron donation. Hence, most of the Cs atoms do not lose their valence electron completely, but only polarise, with negative charge accumulating on the GaAs side of the (Cs,O) layer. In a simple dipole model, the (Cs,O) monolayer can thus be described as a planar capacitor of a thickness of one atomic diameter. The resulting very strong ( $\sim 10$  GV/m) electric field in the cesium layer reduces the vacuum level by an amount  $V_{\text{dipole}} \approx 4$  eV. Deposition of small amounts of oxygen or fluorine enhances the effect for reasons not fully understood [Fis72].

As the vacuum level now lies at an energy lower than the conduction band minimum in the *p*-GaAs *bulk*, we refer to this state as *effective* Negative Electron Affinity (NEA). The effective workfunction remains positive, but is lower than the band splitting  $E_{\text{gap}}$ . As shown in figure 2.1, part of the electrons thermalised to the conduction band minimum may now leave the crystal without further energy supply by tunnelling through the thin residual barrier present at the location of the (Cs,O) layer. The emission process is complicated by the fact that only a small part (a few percent) of the electrons succeed to tunnel through the barrier immediately [Ter95]. A significant fraction reflects at the GaAs-(Cs,O) boundary and stays trapped in the band bending region. Here the electrons lose energy by scattering at surface defect states and by phonon emission, before they either finally escape by tunnelling to the vacuum or recombine with holes [Orl00].

The electrons emitted from the GaAs photocathode thus do not retain their narrow thermal energy distribution from the bulk of the GaAs crystal, but populate an energy spectrum almost as wide as the value of the NEA [Drou85, Orl01]. However, in practical cathode operation, the emission of electrons of energies lower than about the potential of the GaAs bulk conduction band minimum is effectively suppressed by the space charge generated by the electron cloud accumulating in front of the emitting surface. It has been shown that the energy spread of the electron gas effectively extracted from a GaAs(Cs,O) photocathode operated in space-charge mode is about the same than the thermal energy spread in the crystal bulk. The latter is of  $k_{\text{B}}T \approx 30$  meV at room temperature and of  $k_{\text{B}}T \approx 10$  meV for a cathode cooled to liquid nitrogen temperature [Orl04].

## 2.3 Handling of NEA Photocathodes

The GaAs photocathodes put into operation throughout this work have been designed and are manufactured at the Russian Institute of Semiconductor Physics in Novosibirsk in the group of Terekhov *et al.*. Photographic pictures of a photocathode are shown in figure 2.2. The cathode consists of a circular GaAs layer of 3 mm radius

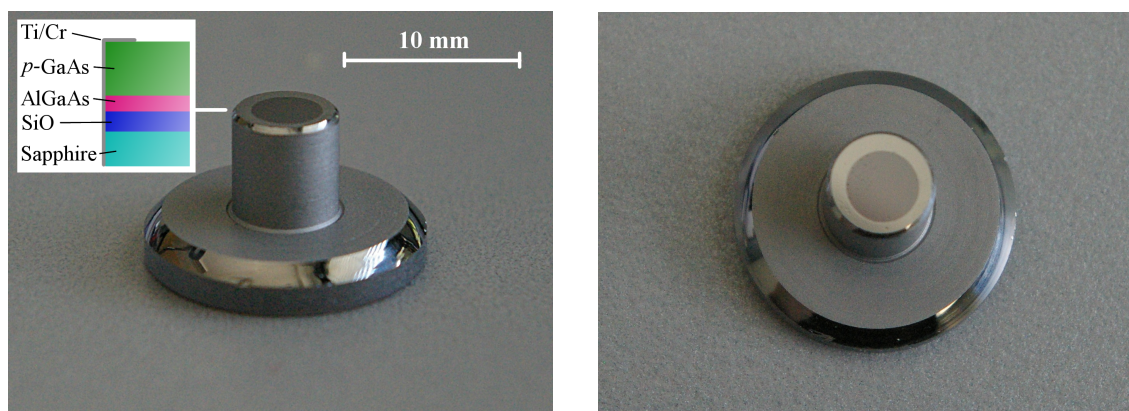


**Figure 2.2:** A NEA GaAs photocathode as used in the cold Electron Target of the TSR (left: side view, right: front view). The GaAs/AlGaAs heterostructure (circular dark area) is bonded to a transparent sapphire socket which allows to operate the cathode in transmission mode and ensures good thermal contact to the liquid nitrogen cooling system. Electrical contact to the cathode is ensured by a thin titanium or chromium coating (reflective surface) covering the sapphire socket and the edge of the GaAs crystal.

and  $(2 \dots 3) \mu\text{m}$  thickness, doped with Zn at a density of  $(5 \dots 7) \cdot 10^{18} \text{ cm}^{-3}$ . The  $p$ -GaAs crystals are grown in orientation (100), either by liquid phase epitaxy (LPE) or by metal-organic chemical vapour deposition (MOCVD). Designed to be operated in transmission mode, the cathodes are not fixed to a metallic base plate but diffusion-bonded to a transparent sapphire socket and electrically contacted through a 120-nm-thick titanium or chromium coating covering the sapphire and the edge of the GaAs crystal (c.f. figure 2.2). Between the sapphire and the  $p$ -GaAs, a 50-nm-thick layer of AlGaAs creates a potential step in the semiconductor band structure preventing electron drift towards the sapphire side of the crystal, thus enhancing the overall photoelectron yield of the cathode. In addition, an antireflective coating of SiO between the sapphire and the GaAs layer enhances the light absorption coefficient of the photocathode.

While the principles of NEA photoelectron emission are simple, cathode preparation, storage and manipulation is delicate. Good adhesion of the (Cs,O) monolayer requires the initial GaAs surface to be extremely clean. Techniques routinely used to prepare GaAs surfaces that are clean on the atomic level include chemical etching, thermal vacuum annealing, and atomic hydrogen cleaning. However, even after optimal surface preparation, the (Cs,O) monolayer stays very fragile and is easily destroyed by chemical agents binding to Cs and O. Very good vacuum conditions are thus of prime importance for storage and operation of photocathodes. In this section, we lay out the more general principles of handling, activation and surface cleaning of NEA photocathodes. A description of the corresponding experimental details follows in the upcoming chapter 3.

### 2.3.1 Cathode Activation

Under ideal circumstances, the (Cs,O) activation of the photocathode surface is performed on the atomically clean (100) GaAs surface. While the reduction of the *p*-GaAs workfunction down to the state of NEA is electrically explained by the alkalinity of Cs alone, it has been found since the early days of NEA cathodes that addition of an oxidising species (O<sub>2</sub> or F) significantly enhances the quantum efficiency that can be obtained from the activated cathode [Fis72]. Various studies [Fis72, Wei04, Kam91] indicate that the optimal surface covering ratio is about 0.1...0.2 monolayers of oxygen versus 1...2 monolayers of cesium. In order to experimentally match the optimal Cs/O ratio, we use a variant of the so-called “yo-yo”-technique during which the GaAs cathode is exposed to a constant cesium flux and an alternating O<sub>2</sub> flux.

The cesium flux is provided by dispensers based on Cs<sub>2</sub>CrO<sub>4</sub> (*SAES Getters*) sublimating pure cesium gas when heated by an electric DC-current, which is typically of (3.5...3.9) A. During the surface activation procedure, the quantum efficiency of the photocathode is monitored by application of a small ( $\approx 40$  V) negative potential to the photocathode and continuous measurement of the photoelectron current. Photons are supplied by a weak 635 nm laser beam of a DC power of approximately 10  $\mu$ W. Low-frequency (287 Hz) modulation of the laser beam allows to reliably measure the resulting low photoelectron current (typically a few tens of nA) using a lock-in amplifier. Knowledge of the laser power  $P_\gamma$  and of the photoemission current  $I$  allows to derive the quantum efficiency QE of the photocathode which we define as the number of emitted electrons  $n_e$  per number of irradiated photons  $n_\gamma$ :

$$\text{QE} = \frac{dn_e}{dn_\gamma} . \quad (2.2)$$

Using

$$I = \frac{dn_e}{dt} e \quad \text{and} \quad P_\gamma = \frac{dn_\gamma}{dt} \frac{hc}{\lambda} \quad (2.3)$$

yields

$$\text{QE} = \frac{I}{P_\gamma} \frac{hc}{e\lambda} , \quad (2.4)$$

where  $e$  is the elementary charge,  $\lambda$  the laser wavelength,  $c$  the velocity of light, and  $h$  Planck's constant. It is noteworthy that the measurement of the quantum efficiency is performed in *reflection mode*, i.e. the laser light is shone directly onto the (Cs,O)-activated GaAs surface, in contrast to the so-called *transmission mode*, where the light is irradiated from the back side of the GaAs crystal.

Figure 5.5 shows the quantum efficiency of a GaAs photocathode as well as the pressure in the vacuum chamber recorded along a typical (Cs,O) activation.

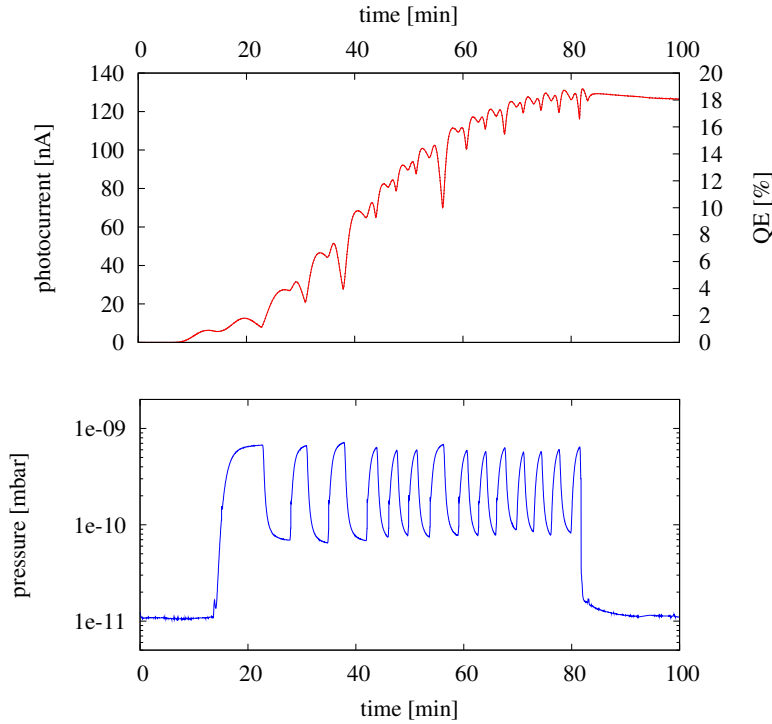


**Figure 2.3:** A typical (Cs,O) activation curve of a GaAs photocathode. The upper part of the figure shows the photocurrent as a function of activation time. The emission current can be recalculated using (2.4) to give the quantum efficiency of the cathode. According to the QE signal, the experimenter switches the O<sub>2</sub> dispensers on or off. The lower figure shows the pressure in the preparation chamber as a function of time. With the O<sub>2</sub> dispensers switched on, the residual gas pressure is dominated by oxygen, the “peaks” in the pressure signal thus indicate periods of oxygen exposure.

The cathode is first exposed to cesium gas only. The rise of the total residual gas pressure in the vacuum chamber caused by operation of the Cs dispenser is very low and thus not visible in the figure. After approximately 8 minutes of Cs exposure, the photoelectron current starts to rise noticeably. In this example, it reaches a maximum after approximately 14 minutes. This first local maximum of the QE is commonly referred to as the “first Cs peak” and corresponds to a surface covering of roughly 0.5 monolayers. Further Cs exposure leads to a *decrease* in QE; this state is referred to as *overcesiation*. Thus, after the first local maximum in the QE curve, O<sub>2</sub> dispensers are switched on. Moreover, in order to accelerate further (Cs,O) deposition, the cesium flux is increased by about 50% and kept constant at this new value for the rest of the process. Operation of the O<sub>2</sub> dispensers causes the pressure in the chamber to rise by almost two orders of magnitude, the residual gas is dominated by molecular oxygen. The presence of oxygen at the GaAs surface assists the deposition of Cs [Fis72], the QE starts to rise again and reaches another local maximum at approximately 20 minutes (Cs,O) exposure time. After this first “oxygen peak” the QE decreases again, we say that the GaAs surface is *undercesiated*. Thus, the O<sub>2</sub> dispensers are disabled again while keeping the cesium flux constant. As soon as the oxygen pressure drops, the photocurrent starts to rise.

The on and off switching of the oxygen exposure while observing the evolution of the cathode quantum efficiency leads to the characteristic “yo-yo” activation curve visible in figure 5.5. Initially, each (Cs,O) cycle leads to a higher quantum efficiency

than the previous one. However, after typically 10...15 oxygen exposures, the photocurrent reaches a saturation level. Further (Cs,O) exposure has been found to lead to a slow decrease of the cathode QE. While we cannot measure directly the thickness of the resulting (Cs,O) layer on the GaAs crystal, former studies indicate that the maximum QE is reached at a (Cs,O) thickness of 1 to 2 monolayers [Wei04].

In our setup the point of maximum QE is typically reached after 70...90 minutes of (Cs,O) activation. After that, the Cs and O<sub>2</sub> dispensers are switched off and the residual gas pressure in the cathode preparation chamber quickly drops to the 10<sup>-12</sup> mbar range. Peak quantum efficiencies usually lie between 10% and 25%, depending on the initial cleanness and quality of the GaAs surface. The record quantum efficiency obtained so far from a NEA GaAs photocathode in our setup was of 35%.

### 2.3.2 Cathode Lifetime

The thin (Cs,O) layer which reduces the effective workfunction of the GaAs to the state of Negative Electron Affinity is inherently delicate. The alkaline nature of Cs renders the layer very sensitive to oxidising chemical agents. Storage and operation of NEA photocathodes thus require very good vacuum conditions. Agents known to be harmful to the (Cs,O) layer are H<sub>2</sub>O and CO<sub>2</sub> [Dur96], which are among the most prominent residual gas components after H<sub>2</sub> and CH<sub>4</sub> in our photocathode vacuum setup [Pas96].

Destruction of the Cs layer by chemical reactions with species of higher electronegativity results in a gradual decrease of both the band-bending potential and the atomic dipole field on the GaAs surface, and thereby in a rise of the effective cathode workfunction. Ultimately, the effective electron affinity rises back to positive values and the cathode loses its ability to emit thermalised conduction band electrons. As the integral emission probability of thermalised electrons through the (Cs,O) dipole layer depends on the magnitude of the NEA, the quantum efficiency of the photocathode drops noticeably already long before the state of zero electron affinity is reached [Ter96]. Following a common definition, we say that the *cathode lifetime* is the time interval during which the quantum efficiency of a photocathode decreases by a factor e<sup>-1</sup> [Bar07].

While reactions with the residual gas define the so-called *dark lifetime* of a NEA photocathode, which can be as long as hundreds of hours [Pas96], high current electron emission significantly reduces the lifetime [Wei04]. Leak currents between the photocathode and the electron gun electrodes cause desorption from the electrode surfaces and lead to higher residual gas pressure in vicinity of the cathode compared

to low-current operation.

Another lifetime reducing effect related to the current density extracted from the photocathode is electron impact ionisation of residual gas constituents. Ions produced in the electron beam carry positive charge and are therefore *attracted* by the cathode potential. The resulting ion bombardment of the cathode surface is known to be the main lifetime limiting effect in high-energy photoelectron guns [Bar07, Sin03]. In chapter 3 of this work, it is shown that ion backstream is a lifetime-limiting process also at lower gun potentials of a few hundred or thousand volts.

Finally, in the case of liquid-nitrogen-cooled photocathodes, the density of harmful residual gas agents can, in addition, be enhanced by cryoadsorption at the cold cathode surface. Too deep cooling of the photocathode thus significantly reduces the lifetime compared to room temperature operation. Chapter 2 provides details about the lifetime-limiting effects encountered during high-current operation of our NEA GaAs(Cs,O) photocathodes in the cold electron target of the TSR.

### 2.3.3 Surface Cleaning

After degradation of the (Cs,O) layer beyond the point of positive electron affinity, products originating from reaction of the (Cs,O) layer with residual gas agents, residual Cs atoms as well as Ga and As oxides remain on the GaAs surface. This surface pollution inhibit efficient re-deposition of (Cs,O) upon activation. The degraded cathode surface has thus to be cleaned prior to reactivation. At this point, we only give a general overview of the cleaning techniques put into effect with more details and recent developments being laid out in the following chapter 3.

#### Thermal Cleaning

In the simplest case, surface cleaning is performed by heating the GaAs crystal. Placing the photocathode in front of a sufficiently powerful halogen lamp, can heat it to temperatures of more than 900 K in vacuum [Wei04]. It has been shown that heating of the GaAs surface to  $\sim 900$  K removes all traces of cesium and oxygen from preceding activations. However, at such high temperatures, As sublimates from the crystal, causing As vacancies near the active surface [Pie80]. These crystal defects are efficient electron-hole recombination centres, their accumulation would thus lead to a steady and irreversible degradation of the quantum efficiency of the cathode. We therefore heat our cathodes only to a temperature of  $\approx 740$  K, i.e. well below the As sublimation point [Orl09a]. After typically 40 to 50 minutes the heater is

switched off and the cathode is allowed to cool down for at least one hour before it is reactivated by (Cs,O) exposure.

Heat-cleaning and subsequent re-activation can be repeated typically 3 times. For subsequent activation cycles, the maximum quantum efficiency decreases significantly. The reason for this behaviour is found in the presence of oxides on the GaAs surface, as the oxygen on the GaAs surface forms non-volatile  $\text{Ga}_2\text{O}_3$  and  $\text{As}_2\text{O}_3$  which desorb only incompletely at bakeout temperatures of 740 K [Orl09a]. These surface oxides accumulate during the activation cycles and increasingly inhibit the building of new (Cs,O) layers. After typically 3 activation cycles, a more elaborate cleaning of the GaAs surface is necessary in order to recover the initial quantum efficiency of the cathode.

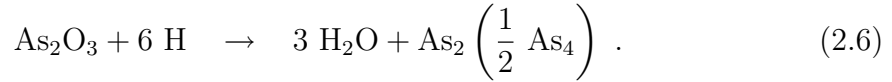
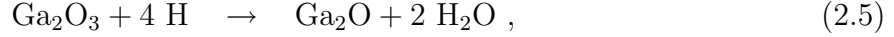
### Chemical Etching

Etching of the degraded and oxidised GaAs surface by hydrochloric acid has been shown to remove all polluting oxides and to lead to an atomically flat GaAs (100) surface [Ter02]. In our case, GaAs cathode surfaces are etched in a solution of HCl in 2-propanol of molarity 3 for 120 seconds at room temperature. The etching process leaves a thin layer of gallium chlorides ( $\text{GaCl}$ ,  $\text{GaCl}_2$ ,  $\text{GaCl}_3$ ) and arsenic on the GaAs surface. The latter As layer has proven to be beneficent, as it passivates the underlying GaAs surface against renewed oxidation.  $\text{GaCl}$  and  $\text{GaCl}_3$  are known to desorb in vacuum at  $330^\circ\text{C}$  and  $80^\circ\text{C}$ , respectively. Neutral As has been shown to completely desorb at a temperature of  $400^\circ\text{C}$  [Wei04]. Thus, the product layer originating from the etching process is easily removed by subsequent vacuum annealing of the cathode. The main drawback of the HCl cleaning procedure is the requirement of removing the respective photocathode from the vacuum setup. Contamination of the cathode surface by contact to air is prevented by a pure nitrogen protective atmosphere surrounding the cathode during the etching procedure and during the transfer back to the vacuum setup. The subsequent pumping of the cathode loading chamber takes approximately 24 hours to reach a pressure of approximately  $1 \cdot 10^{-8}$  mbar at which the GaAs sample can be transferred to a UHV chamber where vacuum annealing can be performed. The complete GaAs surface cleaning procedure by etching in HCl thus takes more than one day before the cathode is ready for (Cs,O) reactivation.

### Atomic Hydrogen Cleaning

An alternative way of recovering an atomically clean GaAs surface from an already activated and degraded photocathode is exposure to atomic hydrogen radicals. For-

mer studies have shown that exposure of degraded GaAs cathodes to neutral hydrogen atoms in vacuum removes all gallium and arsenic oxides found on the cathode surface even at moderate temperatures of approximately 400 °C [Lan89]. Mechanisms proposed by Ide and Yamada explain the cleaning effect by reaction of the non-volatile surface oxides Ga<sub>2</sub>O<sub>3</sub> and As<sub>2</sub>O<sub>3</sub> with H radicals [Ide94, Yam94]:



All the resulting species, H<sub>2</sub>O, Ga<sub>2</sub>O, As<sub>2</sub>, and As<sub>4</sub>, are volatile in vacuum at temperatures of 400 °C or below. Atomic hydrogen cleaning thus allows to prepare a GaAs surface clean on the same atomic level as achieved by chemical etching without the requirement of removing the photocathode from the vacuum setup, which constitutes a significant practical advantage. Cathode heating to 450 °C and hydrogen exposure typically take only 20 minutes, followed by vacuum annealing of the cathode for approximately 50 minutes. Hence, atomic hydrogen treatment yields a fully cleaned photocathode ready for (Cs,O) reactivation after only 2 hours.

While former studies have found that repeated atomic hydrogen exposures lead to slow, but irreversible degradation of the maximum achievable cathode quantum efficiency [Mar03], we do not observe this effect [Orl09a]. We explain this by the fact that former studies used radiofrequency plasmas as sources of atomic hydrogen [Lan89]. Such sources produce hydrogen atoms as well as protons of relatively high kinetic energies (up to approximately 20 eV) which can create defects on the *p*-GaAs crystal surface. These are known to be efficient electron-hole recombination centres that degrade the cathode quantum efficiency irreversibly [Mar03]. Our atomic hydrogen setup is based on thermal cracking of hydrogen molecules in a hot capillary, creating hydrogen radicals of thermal kinetic energies of only (0.1 . . . 0.2) eV which are of no danger to the cathode surface. Details of the atomic hydrogen setup, the cleaning procedure, as well as an analysis of the long-term impact of repeated hydrogen cleaning on the photocathode quality will be given in chapter 3.

## 2.4 Spectral Response

The functional dependence between the cathode quantum efficiency and the wavelength of the irradiated light used for electron excitation is called *spectral response* of the photocathode. Spectral response measurements are widely used as a tool to investigate the band structure, the electron diffusion properties or the temperature of NEA GaAs photocathodes [Sch65, Pie80].

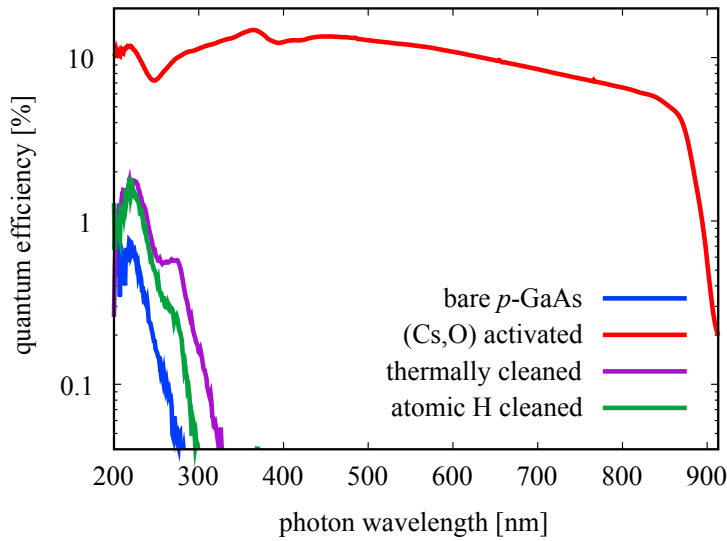


**Figure 2.4:** Spectral response of a photocathode for different states of the GaAs surface. *Blue:* Bare GaAs surface prepared by chemical etching in HCl and vacuum annealing. *Red:* Fully (Cs,O) activated photocathode. *Purple:* Thermally cleaned surface after several activation cycles. *Green:* Surface cleaned from oxides by atomic hydrogen exposure.

During this work, a spectral response measurement setup has been implemented at the photocathode setup of the TSR Electron Target. The measurement principle relies on detection of the photoelectron current of a cathode while it is being irradiated by a tunable monochromatic light source. The very low emission current is measured using a similar lock-in technique as described above in the case of fixed-wavelength quantum efficiency measurements. These more technical details of the setup are described in chapter 3.

As shown above, thermalised conduction band electrons can only be emitted by a GaAs cathode that has been prepared into the state of Negative Electron Affinity. For spectral response measurements, the excitation light is irradiated from the (Cs,O) side of the GaAs crystal. This so-called *reflection mode* photon irradiation causes electrons to be excited very close to the surface barrier created by the Cs layer. They can thus reach the GaAs surface before being given sufficient time to relax into a thermal energy distribution at the bottom of the conduction band. For spectral response diagnostics, this emission of non-thermalised electrons is beneficial, as it allows to measure quantum efficiencies also for photocathodes that are *not* in the state of NEA.

Figure 2.4 visualises spectral responses of a photocathode measured for different GaAs surface conditions. The blue curve shows the spectral dependence of the cathode quantum efficiency for a bare GaAs surface, obtained by etching in HCl and subsequent vacuum annealing as described earlier. As can be seen, the quantum efficiency is practically zero for any photon wavelength longer than approximately 230 nm. This reflects the fact that photoelectrons have to overcome the high work-function of the unactivated *p*-GaAs crystal ( $\Phi \approx 5.4$  eV). In contrast, the red curve represents the spectral response of the same GaAs cathode after full (Cs,O) acti-

vation. Here, an almost constant quantum efficiency of approximately 10% can be observed over a broad spectrum, ranging from the ultraviolet (200 nm) to the near-infrared region. Photons of any wavelength longer than 880 nm have energies lower than the band gap of GaAs ( $E_g = 1.42$  eV), making photoexcitation impossible. Correspondingly, the photocathode's response vanishes quickly at wavelengths beyond 880 nm. The purple and green curves in figure 2.4 depict the spectral responses of the cathode after thermal and atomic hydrogen treatment, respectively, as described above. One can observe that both surface cleaning procedures reduce the quantum efficiency of the cathode drastically compared to the (Cs,O)-activated state, however not down to the level of the bare surface prepared by chemical etching. In case of the thermally cleaned surface, the residual quantum efficiency stems from surface contamination by non volatile Ga and As oxides as discussed above. Atomic hydrogen treatment is able to remove this oxide pollution and thus lowers the quantum efficiency further than thermal cleaning. The higher response curve compared to the bare GaAs surface is due to the presence of residual Cs atoms which exposure to hydrogen radicals cannot remove.

A detailed discussion of spectral response measurements as a diagnostic tool for surface cleaning techniques is given in chapter 3.

## 2.5 GaAs Photocathodes in PEA Regime

As figure 2.4 suggests, in-vacuum cleaning of a previously activated cathode to the state of practically zero quantum efficiency is difficult. The standard thermal cleaning procedure employed to remove degraded (Cs,O) from the GaAs surface always leaves the photocathodes still retaining a low residual quantum efficiency in the ultraviolet spectral range. The thermally cleaned photocathode is in the state of *Positive Electron Affinity* (PEA), so that only non-thermalised photoelectrons can be emitted. That is, the residual quantum efficiency manifests itself only upon reflection mode irradiation.

Figure 2.5 explains this phenomenon energetically. For a bare GaAs photocathode (a), the workfunction  $\Phi$  of the material is of approximately 5.4 eV. Electron emission is thus not possible for photon energies  $\hbar\omega < 5.4$  eV or wavelengths  $\lambda > 230$  nm. Activation with (Cs,O) lowers the vacuum level near the GaAs surface drastically to the state of effectively negative electron affinity, such that any conduction band electron may tunnel to the vacuum as described above (b). Transmission-mode electron emission from the cathode is now possible for any photon energy higher than the band splitting  $E_{\text{gap}} = 1.42$  eV. This changes, once the (Cs,O) layer has degraded to the point where the electron affinity ( $\chi$ ) rises back to positive val-

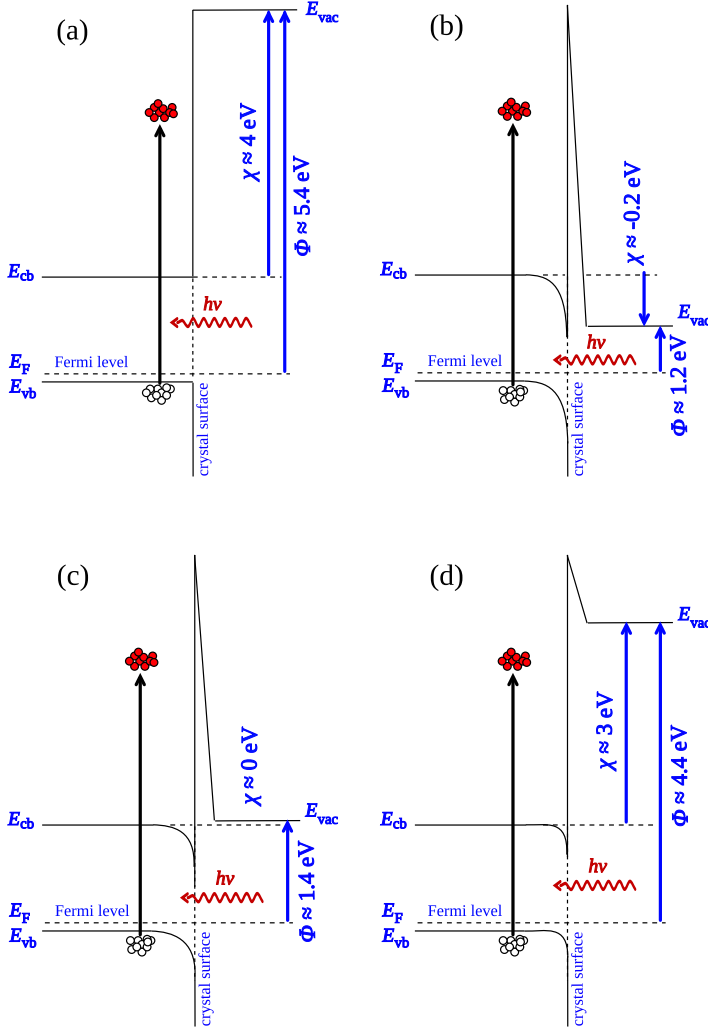


**Figure 2.5:** PEA electron emission. (a) For a bare GaAs surface, photoelectrons have to overcome the full workfunction of approximately 5.4 eV in order to escape to the vacuum. (b) (Cs,O) activation reduces the vacuum level to the state of NEA. (c) Subsequent degradation of the (Cs,O) layer leads to a rise of the vacuum level energy. (d) Due to residual surface contamination, the vacuum level does not rise back to the initial value, but converges to a level  $\sim 1$  eV lower compared to that of the bare GaAs surface.

ues (c). Now, electron emission requires excitation photons to provide a minimum energy

$$\hbar\omega_{\min} = E_{\text{gap}} + \chi. \quad (2.7)$$

One might expect the initial state (a) to be eventually restored by complete destruction of the (Cs,O) layer. However, even the in-vacuum thermal cleaning procedure is not able to completely remove all Cs and surface oxides from the GaAs crystal. During degradation of the (Cs,O) layer, the vacuum energy level thereby converges to a value lower by approximately 1 eV compared to the bare *p*-GaAs surface (d).

Using the electron emission spectroscopy setup, this effect can be measured and is illustrated in figure 2.6. The quantum efficiencies of a GaAs photocathode are shown as a function of excitation photon energy. Again, the blue curve represents the bare GaAs surface obtained by etching in HCl. The photoelectron yield drops steeply at photon energies below approximately 5.4 eV, in good agreement with our

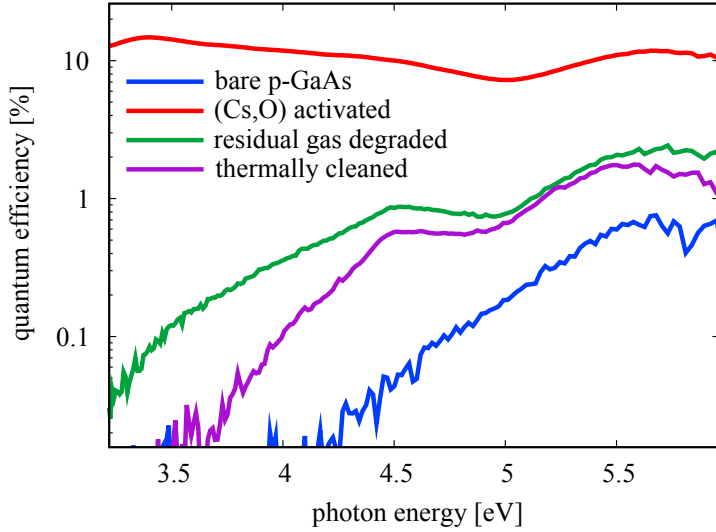


**Figure 2.6:** Quantum efficiency as a function of irradiated photon energy for a GaAs photocathode in PEA regime. *Blue:* Bare *p*-GaAs surface. *Red:* Fully (Cs,O)-activated cathode. *Green:* PEA spectral response after 60 h of accelerated (Cs,O) layer degradation. *Purple:* Spectral response after thermal surface cleaning.

above considerations. The red curve, showing the quantum efficiency of the fully (Cs,O)-activated cathode, is practically constant over the entire spectral range of the figure. The green line represents the photocathode efficiency after subjecting the (Cs,O) layer to an artificially accelerated degradation process. The latter was achieved by storing the sample in a vacuum chamber of significantly worse residual gas pressure ( $\sim 10^{-8}$  mbar) compared to the photocathode activation chamber which is normally used for storage of activated cathodes ( $5 \cdot 10^{-12}$  mbar). While the decrease in quantum efficiency was initially very fast, it converged after a few hours to the values shown in the plot. One recognises a high residual quantum efficiency compared to the bare GaAs surface, especially in the energy range above 4.5 eV. This indicates that, even in this severely degraded state of the (Cs,O) layer, the vacuum level in vicinity of the GaAs surface lies approximately 1 eV lower compared to a crystal with no surface layer at all. As shown again by the purple curve in figure 2.6, even thermal cleaning of the cathode cannot remove this residual quantum efficiency completely.

The residual quantum efficiency can be exploited by irradiating the photocathode in reflection mode using ultraviolet light. We refer to this application as PEA (*Positive Electron Affinity*) electron emission from GaAs. Photons in the interesting energy range between 4.5 eV and 5.0 eV can be easily provided at high flux densities using e.g. standard 262 nm laser sources ( $\hbar\omega = 4.7$  eV). While the achievable quantum efficiencies of (0.1...1) % are low compared to those of fully (Cs,O)-activated NEA photocathodes, they are at least one order of magnitude higher than that of plain metal surfaces [Dow09] and much more *stable* that of NEA cathodes.

Operation of GaAs photocathodes in PEA regime is thus a viable option for applications which need only relatively low average electron current densities, for

which thermalisation of the electron gas in the cathode is not of importance, but which require maintenance-free operation of a single photocathode over long times. Design and initial tests of an electron gun employing a PEA GaAs photocathode are presented in chapter 5.



# Chapter 3

## The Photoelectron Target of the TSR

Merged electron-ion beam devices are widely used tools in atomic, molecular and nuclear physics at storage rings. In 1966, Budker proposed a way to enhance the brilliance of proton colliders by mixing the ion beam with a comoving, cold electron “buffer gas” [Pot90]. First realised in 1974, *electron cooling* has, since the late 1980s, become a standard phase space cooling technique for heavy ion beams stored in ring accelerators that operate at low or medium ion velocities [Wol91, Lie87, Dan94]. Extension of this technique to highly relativistic [Mag06, Fed06] as well as to very low-energetic ion beams [Shor, Orl07] is ongoing.

In addition, electron-ion beam merging devices are powerful tools to investigate electron-ion collision dynamics over a wide range of collision energies [Wol00]. Velocity dematching between ion and electron beams especially allows to generate very low collision energies, down to the scale of a few meV, which are inaccessible to laboratory-frame experiments. With reference to the non-zero collision velocity of ions and electrons, we call electron beams used in this way *electron targets*.

### 3.1 The Electron Target

In 2003, the Test Storage Ring (TSR) of the Max-Planck-Institute of Nuclear Physics (MPIK) has been equipped with a second electron-ion merging section in addition to its *Electron Cooler* already included in the original design. In contrast to the latter, the new merging section has been specifically optimised to be operated as an *Electron Target* for high-precision atomic and molecular electron-ion recombination

experiments [Spr04]. While usage of a conventional thermionic cathode is possible [Spr04, Les07], the Electron Target can be equipped with an electron gun based on NEA GaAs photocathodes in order to achieve state-of-the-art electron beam energy monochromaticity [Orl04]. The present work is focussed on that latter mode of operation.

The designs of both, Electron Cooler and Target, are based on the same general working principle. The electron beams are produced outside the beamline of the storage ring. Guided by magnetic fields of typical inductions of a few tens of mT, the electron beams are merged with the stored ion beam by toroidal coils leading into the TSR's beamline. As the electron beams are of much lower *rigidity* than the ion beam, the electron trajectories are bent into the direction parallel to the ion trajectory, while the latter is only weakly disturbed and can be easily corrected using dipole magnets outside of the beam merging sections. After travelling a given distance alongside the stored ions, the electrons are demerged from the ions by another toroidal coil and dumped onto a Faraday cup.

The layouts of the TSR and the Electron Target are depicted in figure 3.1, and a photographic view of the Electron Target section is shown in figure 3.2. The design of the Electron Target is modular, mainly consisting of four components: the electron gun setup, the electron beam acceleration section, the 1.5-m-long electron-ion interaction section, and the collector section where the electron beam is dumped onto the Faraday cup after its demerging from the ion beam. In contrast to the Electron Cooler, both, the acceleration and collector sections of the Target, lie in the plane defined by the TSR in order to allow easy access to the electron gun. This is required for photocathode operation of the latter as will be discussed below.

Electron current intensities produced by the electron target when operating with the photocathode normally amount to (0.1...1) mA. The 1.2-m-long acceleration section of the Target features a total of 77 independent ring electrodes which are used to shape the electron accelerating potential. Slow, adiabatic acceleration minimises beam heating through longitudinal-longitudinal plasma relaxation, as will be discussed in chapter 4.

A longitudinal magnetic guiding field with a typical induction of (0.02...0.04) T avoids divergence and heating by plasma relaxation of the electron beam as it travels along the Target, as will be discussed in chapter 4. The disturbance of the ion trajectory caused by the electron guiding field is corrected by two pairs of bending dipole magnets, placed before the merging and after the demerging toroid coils, respectively. While the electron emitting area of the photocathode has a diameter of only 3 mm, magnetic expansion of the electron beam increases its width to typically (12...20) mm. Expansion is not only necessary in order to obtain a good overlap with the stored ion beam, but also decreases the transverse momentum spread of the

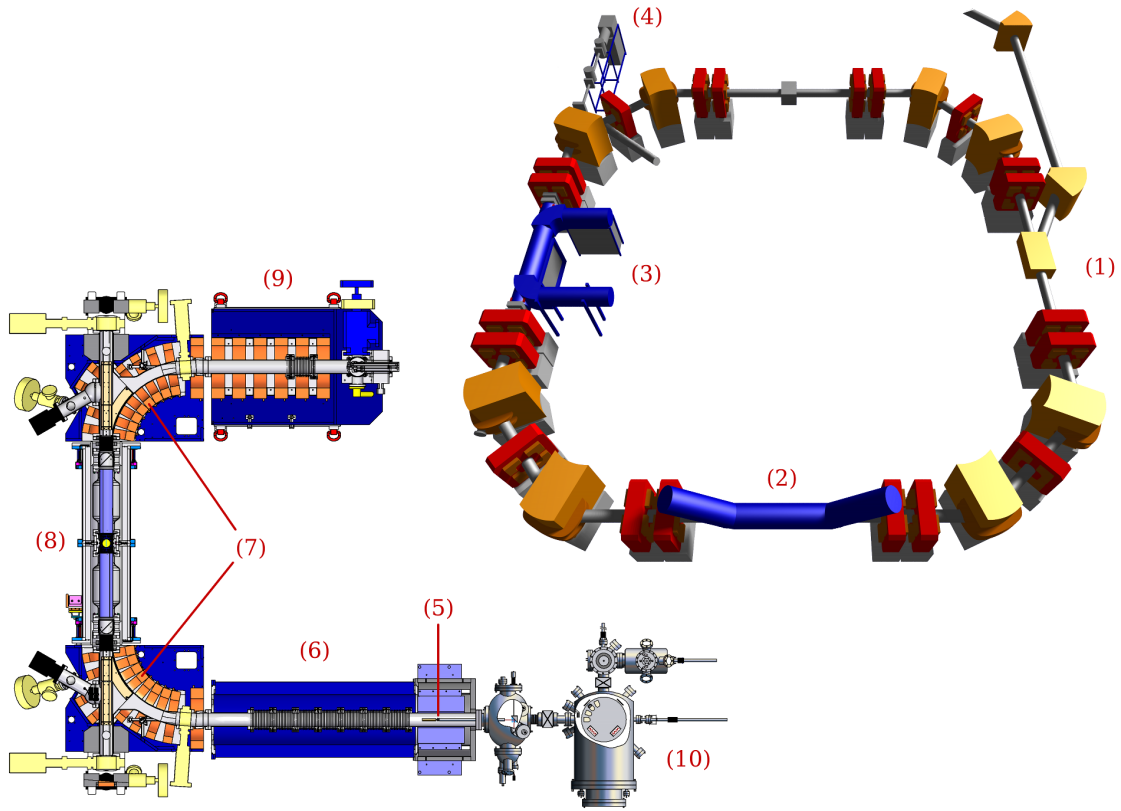


**Figure 3.1:** Schematic drawing the heavy ion-storage ring TSR at the MPIK and horizontal cut of the Electron Target. Ion beams are injected into the storage ring in the section marked (1). The blue structures at the bottom and left sides are the Electron Cooler (2) and the Electron Target (3), respectively. Following the Electron Target, a set of counting and imaging detectors (4) awaits electron-ion reaction products. The detailed cut drawing of the Electron Target shows the photoelectron gun (5), the acceleration section (6), the toroidal coils for merging and demerging electron and ion beams (7), the 1.5-m-long interaction section (8), the collector section (9), and the photocathode vacuum setup (10).

electron beam (c.f. chapter 4). The electron gun is thus surrounded by superconducting coils creating an intense longitudinal magnetic field of a typical induction of (0.8...1.6) T at the location of the photocathode. Given a guiding field induction of normally 0.04 T in the acceleration section, this corresponds to a typical field ratio  $\alpha$  of 20 to 40 in the beam expansion zone.

The collector section features a high-voltage (up to 3 kV) water-cooled Faraday cup. A negatively-biased blocking electrode at the entrance of the latter prevents secondary electrons, liberated from the cup material upon impact of the primary beam, to drift back into the Target section. An aperture of 50  $\mu\text{m}$  diameter in the Faraday cup electrode backed by a retarding field analyser allows to measure the current density distribution as well as the longitudinal velocity spread of the electron

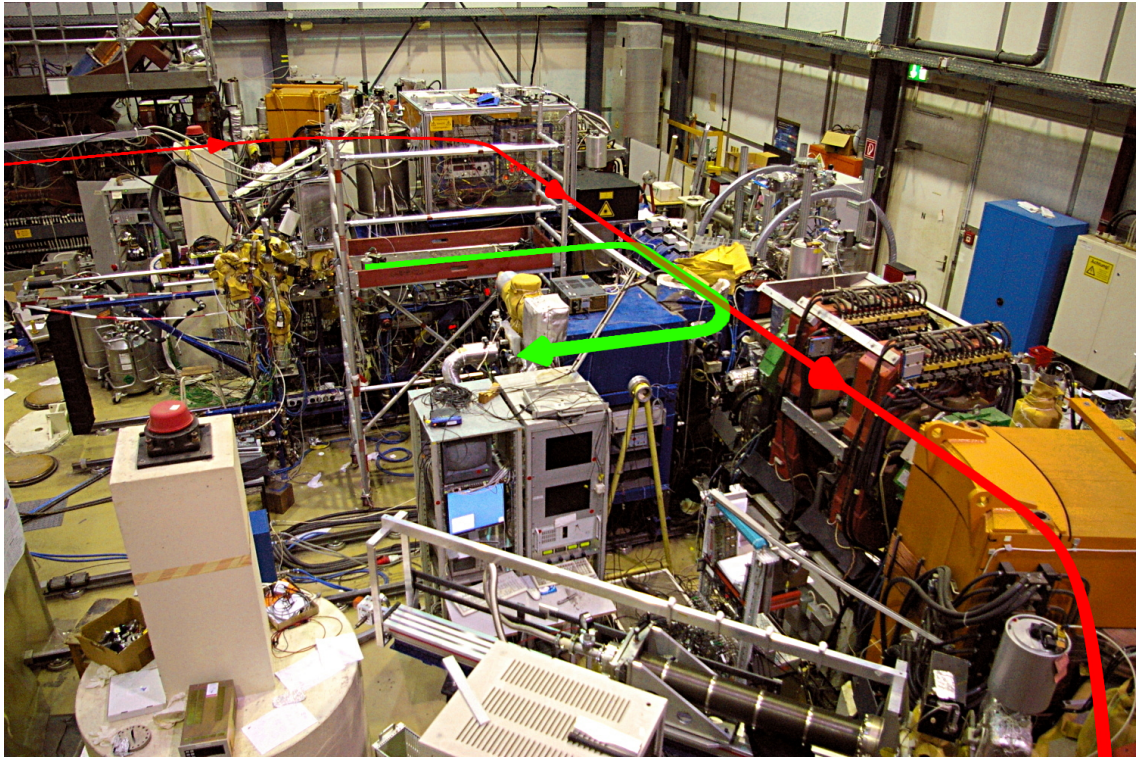


**Figure 3.2:** View of the section of the TSR containing the Electron Target. The overlaid red line indicates the trajectory of the stored ion beam, the Electron Target beam is highlighted in green. The arrows indicate the flight direction of electrons and ions.

beam [Spr04, Les07].

In all sections, the beam pipes of the Electron Target are surrounded by magnetic dipole coils which produce weak magnetic correction fields in both vertical and horizontal directions transverse to the main guiding field. This allows to independently incline the electron flight direction both vertically and laterally in all Target sections and thereby create overlap between the electron beam and the TSR's stored ion beam.

## 3.2 Photocathode Setup

In photocathode operation, the Target's electron beam is produced by a NEA GaAs photocathode, cooled by liquid nitrogen to achieve lowest electron temperatures. The cathode is mounted in a Pierce-type electron gun and can be illuminated by laser beams either from the back side of the GaAs crystal (*transmission mode* operation)

or from the (Cs,O)-activated side of the same (*reflection mode*). While the electron gun itself is compact and of relatively simple design, a complex vacuum setup is necessary for loading, cleaning, and (Cs,O) activation of the GaAs cathodes. In total, the so-called *photocathode setup* consists of three independent UHV vacuum chambers as shown in figure 3.3: The *electron gun chamber*, the *cathode preparation chamber*, and the combined *cathode loading and atomic hydrogen chambers*. Each chamber is a self-contained vacuum system with individual pumping units. The gun chamber is necessarily open towards the Electron Target’s acceleration section and is thus connected to the TSR vacuum. The remaining chambers are isolated from each other by all-metal gate valves which are only temporarily opened during photocathode transfer.

Photocathodes can be moved across the vacuum setup using a system of three magnetically-coupled manipulators (c.f. figure 3.3). Herefore, the sapphire sockets supporting the GaAs crystals are fixed into cylindrical titanium holders. A bayonet coupling mechanism allows to fix these holders to the tip of a manipulator and to move the photocathode from one vacuum chamber to another. In the preparation and loading chambers, metal counterparts to the cathode holders act as docking ports which allow storage of photocathodes inside the vacuum setup. In the electron gun, a more complicated cathode fixation mechanism is used, designed to ensure good thermal conductance between the GaAs supporting sapphire socket and the liquid nitrogen cooling system [Wei04].

### 3.2.1 Photoelectron Gun Chamber

The electron gun chamber provides all infrastructure required for operation of the NEA GaAs photocathodes in the Electron Target. Connected to the TSR vacuum, the base pressure in the gun chamber is of  $(1 \dots 2) \cdot 10^{-11}$  mbar. The electron gun is shown in figure 3.4. Photons required for electron excitation within the GaAs can be delivered either in transmission or in reflection mode. For transmission-mode illumination an 800 nm laser diode (*Coherent F6-808-3-2400C*, maximum output power: 2.4 W) is used, fed into the gun chamber through a lateral viewport and reflected onto the rear cathode surface using a movable prism. Reflection mode illumination employs a diode-pumped solid state laser (*Coherent Verdi V6*, 6 W) with a wavelength of 532 nm. It is reflected onto the photocathode through periscope optics in the merging toroid section of the Electron Target.

The electron gun is of Pierce geometry [Wei04]. Electrons are extracted from the photocathode by a ring electrode placed in front of the cathode, at a distance of 2.4 mm. A Pierce shield placed between the extraction electrode and the cathode, at a distance of only 0.2 mm from the GaAs surface, is used to homogenise the extrac-

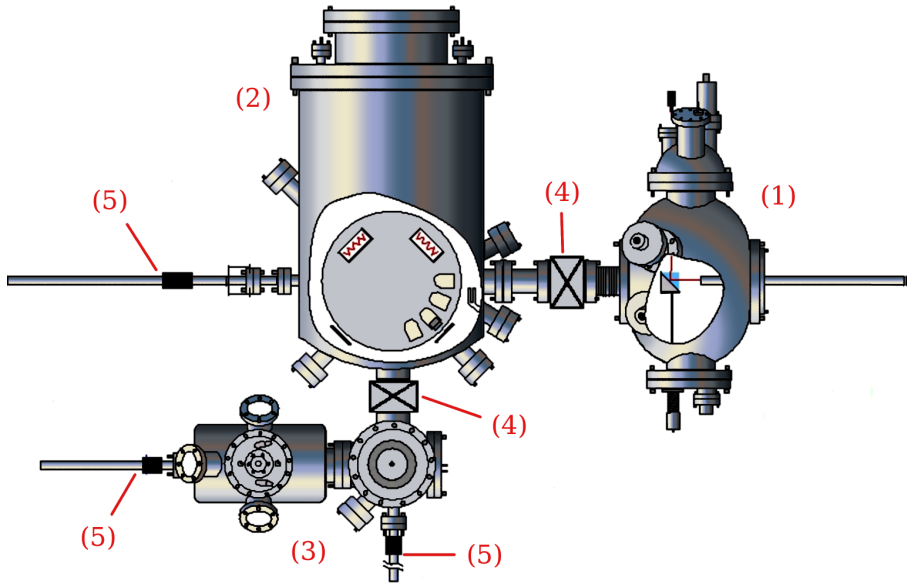


**Figure 3.3:** Schematic drawing of the photocathode vacuum setup used for photocathode operation of the Electron Target section (top view). The setup consists of three distinct vacuum chambers separated by UHV valves (V): The photoelectron gun chamber (1), the cathode preparation chamber (2), and the combined cathode loading and atomic hydrogen cleaning chambers (3). Photocathodes can be moved across the vacuum setup using a system of magnetically driven manipulators (M).

tion field over the cathode surface and leads to a uniform electron density throughout the profile of the electron beam. The intense guiding field of (0.8... 1.6) T produced by the superconducting coils that surround the electron gun prohibits electron propagation transverse to the gun axis. Thus, the initial cross section of the electron beam is defined by the aperture of the Pierce electrode which has a diameter of 3 mm. Typical extraction voltages lie in the range of (50... 200) V. Following the extraction electrode, electrons enter a field-free region created by a 25-cm-long drift tube. Here, magnetic expansion takes place as the magnetic induction drops to a value of (0.02... 0.04) T generated by the guiding solenoids of the Electron Target. An intermediate acceleration ring electrode provides the option to shape the electric field gradient in the region between the extraction electrode and the drift tube. Experience has shown that such intermediate field shaping is not necessary in most situations.

In general, electron guns can operate in two distinct *extraction regimes*. In the case of a strong electric extraction field and/or weak photoelectron excitation rate, every electron emitted from the (Cs,O)-activated GaAs surface is extracted. In this so-called *current limited mode* of operation, the electron current emitted by the gun is determined by the intensity of the excitation laser and the quantum efficiency

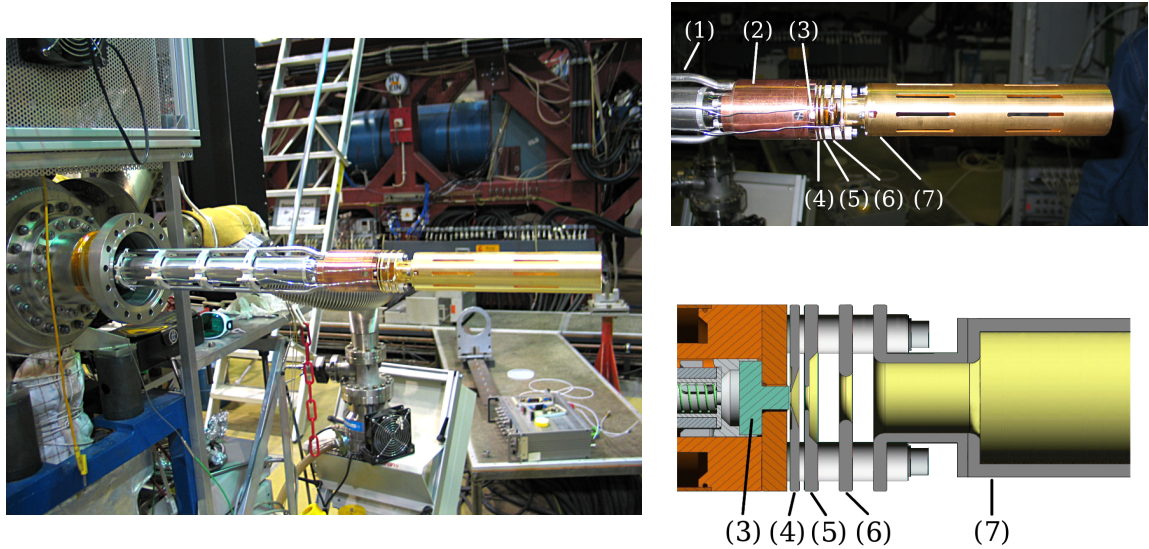


**Figure 3.4:** The photoelectron gun. The left picture shows the gun chamber before being flanged to the Electron Target’s acceleration section. The right pictures show a closeup and a schematic longitudinal cut drawing (modified from [Wei04]) of the electron gun, including the liquid nitrogen supply line (1), the copper HV-coldhead (2), and the sapphire socket of the photocathode (3). Also visible is the gun electrode array: Pierce shield (4), extraction electrode (5), intermediate acceleration electrode (6), and drift tube electrode (7).

of the photocathode alone and does not depend on variations of the extraction potential. For high laser intensities and/or weak extraction fields, the space charge of the electron cloud emitted from the photocathode partially screens the cathode surface from the extraction potential. For a certain extraction voltage, electrons accumulate in front of the emitting surface, up to the point where extraction from and emission into the electron cloud cancel each other. This so-called *space charge mode* of operation is quite beneficent for many applications. The space charge effect stabilises the extraction current at a value defined only by the extraction voltage, independent of short-time fluctuations of the laser intensity or changes of the cathode quantum efficiency due to temperature fluctuations or degradation of the (Cs,O) activation layer. In space charge mode, the extraction current  $I$  of an electron gun relates to the extraction voltage  $U$  by

$$I = P U^{3/2} . \quad (3.1)$$

The parameter  $P$  depends on the distance between the cathode surface and the extraction electrode and can be calculated from the geometry of the gun electrodes using the Child-Langmuir formula [Kir67].  $P$  is called the *perveance* of the electron gun, expressed in units of  $\text{Perv} = \text{A} \cdot \text{V}^{-3/2}$  [Pie40]. For our photoelectron gun, the perveance amounts to approximately  $1 \mu\text{Perv}$ , i.e. a voltage of e.g. 100 V allows to extract an electron current of approximately 1 mA.

The photocathode is embedded in a copper coldhead cooled by liquid nitrogen. The sapphire socket of the photocathode is pressed against the copper wall by a spring with a force of 200 N, which ensures good thermal contact between the cathode and the cooling system. The temperature of the GaAs crystal can thus be assumed to be higher by only a few K compared to that of the coldhead. In operation, a temperature difference between coldhead and cathode of approximately 25 K has been measured, due to heating by the excitation laser beam of approximately 1 W in power [Wei04].

The nitrogen line is electrically isolated from the chamber walls and also serves as feedthrough for the base cathode high-voltage. The electron gun has been designed to operate at base voltages of up to  $-20$  kV with respect to the grounded Electron Target section [Spr04]. Floating low and high voltage supplies are used to lift the Pierce shield, the extraction electrode and the drift tube to the desired voltages with respect to the base cathode potential. The electrode structure is attached to the copper coldhead, with sapphire spacers defining the electrode positions. The use of sapphire ensures electrical isolation between the electrodes while still providing good thermal contact to the coldhead. In a former design of the electron gun, the drift tube electrode was fixed to the chamber wall of the Target acceleration section rather than to the electron gun [Spr04, Wei04]. In order to improve the vacuum conditions at the location of the photocathode, the electron gun design has been changed in such a way that the drift tube is now also thermally anchored to the photocathode coldhead. A direct measurement of the temperature distribution in the electrode array has shown that, if the copper coldhead is cooled down to the temperature of liquid nitrogen (77 K), the acceleration and drift tube electrodes have approximate equilibrium temperatures of 110 K and 130 K, respectively. Owing to its large surface, the cold drift tube is expected to improve the vacuum conditions in vicinity of the photocathode by cryoadsorption of harmful residual gas agents. However, it should be noted that, in practical gun operation, the copper coldhead is not cooled all the way down to the temperature of liquid nitrogen, as will be motivated in an upcoming section. The true temperature of the electrode array in real-life operation is not precisely known, neither is thus the cryopumping speed of the drifttube.

Due to the finite lifetime of the (Cs,O) activation layer, photocathodes used in the electron gun have to be reactivated after a certain time of operation. However, the cost of operation of the MPIK's accelerator facilities and the thereby limited beamtime available for experiments at the TSR require a quasi-continuous operation of the Electron Target. As already mentioned in chapter 2, the cleaning and reactivation processes take 3 to 4 hours. For that reason alone, cleaning and reactivation of the photocathode in the electron gun is not an option. Moreover, in-situ heat-cleaning of the cathode would severely degrade the vacuum conditions in the

TSR and imply time-intensive shutdown and subsequent reactivation of the liquid nitrogen cooling system. Thus, degraded photocathodes have to be mechanically replaced by freshly activated ones. As (Cs,O)-activated GaAs cathodes can only be stored in ultra high vacuum, the switching has to be performed without breaking the UHV conditions.

### 3.2.2 Cathode Preparation Chamber

The *cathode preparation chamber* is the principal facility for storage, cleaning and (re-) activation of GaAs photocathodes. As visible in figure 3.5, four docking positions mounted on a rotatable carousel can be used to park photocathodes if they are not used in the electron gun. A combination of an ion-getter pump (*Varian StarCell*, pumping speed 230 l/s) and non-evaporative getter (NEG) strips (*SAES Getters*) activated by radiative ovens establishes very good vacuum conditions. The base residual gas pressure in the preparation chamber amounts to  $5 \cdot 10^{-12}$  mbar, allowing to store (Cs,O)-activated GaAs cathodes for several days without significant loss of quantum efficiency.

A UHV gate valve separates the preparation chamber from the gun chamber. After opening the valve, shutdown of the Target HV, and removal of the optical prism used to reflect the excitation laser light onto the rear GaAs surface, a high-force magnetically coupled manipulator (*Huntington*, 800 N) aligned to the axis of the electron gun is used to unmount the degraded photocathode from the latter using a bayonet coupling mechanism (c.f. figure 3.3). The degraded cathode is then parked in one of the preparation chamber docks, and a freshly activated cathode is mounted into the electron gun in its stead. A skilled operator is able to perform the cathode switching routine in less than 5 minutes. During the process, the pressure in the gun chamber rises to typically  $10^{-10}$  mbar, dropping back to approximately  $2 \cdot 10^{-11}$  mbar within 20 to 30 minutes. Interruption of the cooling system is not required, that is, after typically half an hour the electron current can be switched back on.

The preparation chamber also provides the infrastructure required for thermal cleaning and (re-)activation of photocathodes (c.f. figure 3.5). Using the rotatable carousel on which the cathode docks are mounted, photocathodes, degraded by usage in the electron gun, can be placed in front of one out of two radiative ovens. The latter are industry-standard halogen lamps (*Osram*, 250 W). In order to account for the absence of convective cooling of their glass bulbs in the vacuum chamber, the lamps are operated at no more than half of their nominal power, i.e. at less than 100 W. Measurements of photoluminescence and transmission spectra from the GaAs have shown that this heating power establishes the optimal bakeout temperature

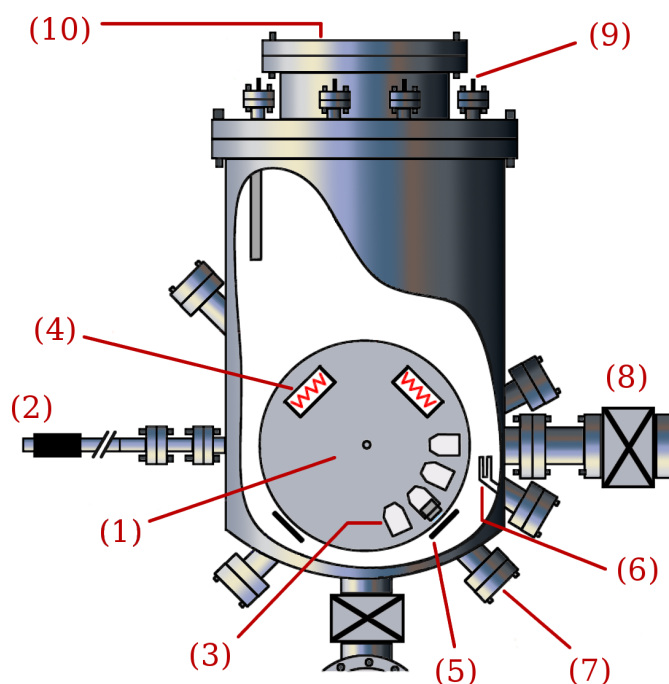


**Figure 3.5:** The preparation chamber. The schematic cut shows the carousel (1), the high performance manipulator (2) used to park photocathodes in the four docking ports (3). By rotation of the carousel, the cathodes can be placed in front of powerful halogen lamps (4) for thermal cleaning, or next to the cesium (5) and oxygen (6) dispensers for (Cs,O) activation. A UV-grade viewport (7) is used for electron emission spectroscopy of photocathode surfaces. A UHV valve (8) separates the preparation chamber from the electron gun while an array of NEG strips activated by electric ovens (9) and an ion-getter pump (not visible) ensure extremely good vacuum conditions. Two large viewports (10, one not visible) allow observation of all cathode manipulations.

of approximately  $(450 \dots 470)^\circ\text{C}$  already stated in chapter 2. The heat-cleaning process typically lasts for 50 minutes, during which the residual gas pressure in the preparation chamber rises to about  $(1 \dots 2) \cdot 10^{-10}$  mbar, dropping back to the  $10^{-12}$ -mbar-range within one hour after the bakeout is finished.

Clean photocathodes can be placed in front of cesium and oxygen dispensers (c.f. figure 3.5) to undergo the (Cs,O) surface activation procedure described in chapter 2. The activation process is monitored online by measuring the emission current flowing through the cathode by using a lock-in technique. The carousel supporting the cathode docks is electrically isolated from the chamber walls and contacted by a vacuum feedthrough electrode. The latter can be used to apply a negative potential (typically  $40 \text{ V} \dots 50 \text{ V}$ ) to the photocathode and to measure the photoelectron current using a picoamperemeter. The light necessary for photoexcitation is delivered by a weak ( $\sim 10 \mu\text{W}$ ) 635 nm laser beam coupled onto the GaAs surface in reflection mode. The laser beam is modulated using a low reference frequency (normally 287 Hz). As the photocathode response time is very fast compared to the laser modulation period, the photoemission current is modulated with the same reference frequency and phase. Using a lock-in amplifier (*Stanford Research SR850 DSP*) set to this reference frequency, even very low emission currents become measurable. The lock-in technique reduces the noise level of the current measurement to approximately 0.5 pA, so that emission current intensities down to

a few pA can be measured practically background-free. As shown in figure 5.5, this sensitivity is high enough to follow the (Cs,O) activation process of a photocathode all the way from an initial quantum efficiency of essentially zero ( $\text{QE}_{\min} \sim 10^{-6}$ ) up to the final quantum yield of typically (10...25) %.

### Spectral Response Measurement Setup

The same lock-in technique is also used for spectral response measurements within the preparation chamber. The corresponding experimental setup is depicted in figure 3.6. Here, instead of the activation laser beam, light from a tunable monochromatic source is shone onto the photocathode surface and allows to measure the emission current as a function of the light wavelength, thus, the cathode quantum efficiency as a function of photon energy (c.f. chapter 2). The tunable light source consists of a combined deuterium/halogen lamp (*Mikropack DH-2000*) equipped with a grid monochromator (*Acton Research SpectraPro-300i*). The light is fed into and coupled out of the monochromator using optical fibres. The beam leaving the fibre is uncollimated, so lens optics are used to image the exit of the fibre onto the cathode surface. An aluminium mirror of finely adjustable pitch and yaw allows to accurately centre the monochromatic light spot on the GaAs surface. The fibres, the lens system, the mirror as well as the viewport of the preparation chamber (*Caburn-MDC VP-100S*) are UV-capable, such that electron emission spectra can be measured down to light wavelengths of 200 nm.

The aperture of the optical fibre has a diameter of 0.6 mm. The lens optics have been designed to have a magnification factor of 7, thus, the light spot projected onto the photocathode has a diameter of 4.2 mm. This is approximately equal to the diameter of the free GaAs surface, i.e. the measurement averages over the complete active photocathode area. As in equation (2.2), the quantum efficiency of the photocathode QE is defined as the number of emitted electrons per irradiated number of photons

$$\text{QE}(\lambda) = \frac{dn_e}{dn_\gamma} = \frac{dn_e}{dt} \frac{dt}{dn_\gamma} = \frac{I_e(\lambda)}{F_\gamma(\lambda)}, \quad (3.2)$$

where we expect the photoelectron current  $I_e$ , the photon flux reaching the cathode  $F_\gamma$ , as well as its quantum efficiency QE to be dependent on the wavelength  $\lambda$  of the irradiated light. Neither the emission spectrum of the deuterium/halogen lamp, nor the transmission functions of the monochromator, mirror, fibres, and lenses are known reliably. Therefore, the photon flux  $F_\gamma(\lambda)$  has been determined experimentally using a calibrated UV-grade photodiode (*Hamamatsu S1336-BQ*) of known quantum efficiency  $\text{QE}_{\text{PD}}(\lambda)$ . The photodiode was placed into the lightpath *outside* the vacuum chamber, following the aluminium mirror. In order to obtain the true photon flux directed at the cathode surface *inside* of the vacuum chamber,

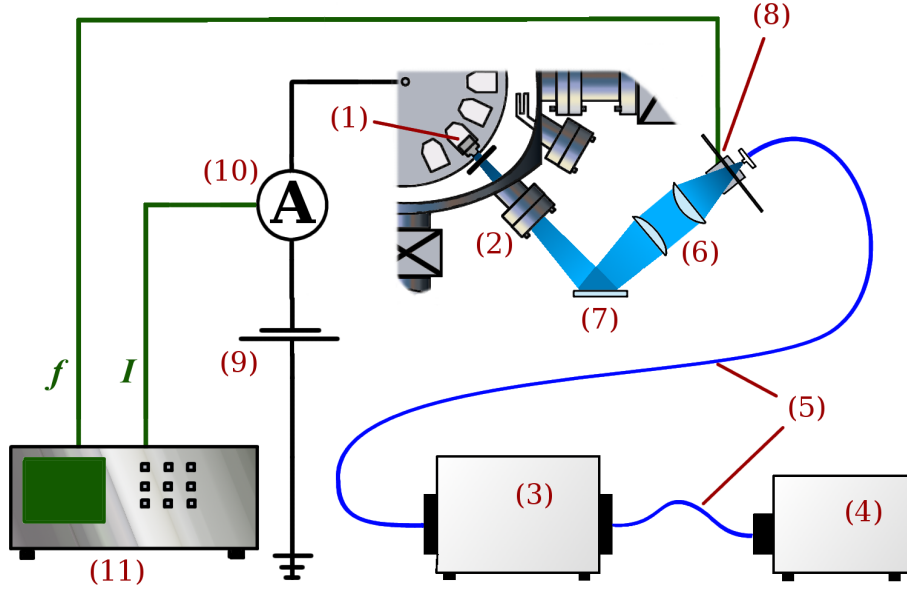


**Figure 3.6:** Scheme of the spectral response measurement setup. The photocathode (1) is placed next to the UV-grade viewport (2) of the preparation chamber. Monochromatic light produced by a grid monochromator (3) fed by a deuterium/halogen lamp (4) is transported close to the setup using UV-capable optical fibres (5), and focussed onto the cathode surface using lens optics (6) and a mirror (7). An optical chopper wheel (8) modulates the light beam with frequency  $f$ . The photocathode is lifted onto negative potential using a small voltage supply (9), and the photoelectron current  $I$  is measured using a fast picoammeter (10). A lock-in amplifier (11) locks to the chopper frequency and separates the photocurrent signal from the background noise.

the value determined from the current intensity  $I_{\text{PD}}$  of the photodiode has to be corrected for the transmission function of the viewport  $T_{\text{w}}(\lambda)$ :

$$F_{\gamma}(\lambda) = \frac{I_{\text{PD}}(\lambda)}{\text{QE}_{\text{PD}}(\lambda)} \cdot T_{\text{w}}(\lambda) . \quad (3.3)$$

Equations (3.2) and (3.3) relate the photocathode quantum efficiency QE to the electron emission current  $I_e$ , measured as a function of the light wavelength  $\lambda$ . The current  $I_{\text{PD}}(\lambda)$  induced in the photodiode by our monochromatic light source setup as well as the transmittance of the UV-viewport  $T_{\text{w}}$  have been accurately measured. The spectral response  $\text{QE}_{\text{PD}}(\lambda)$  of the photodiode is given with high precision by the manufacturer.

### 3.2.3 Cathode Loading and Atomic Hydrogen Chambers

The last major component of the photocathode setup is the combined cathode loading and atomic hydrogen (LAH) chamber. Separated from the preparation chamber

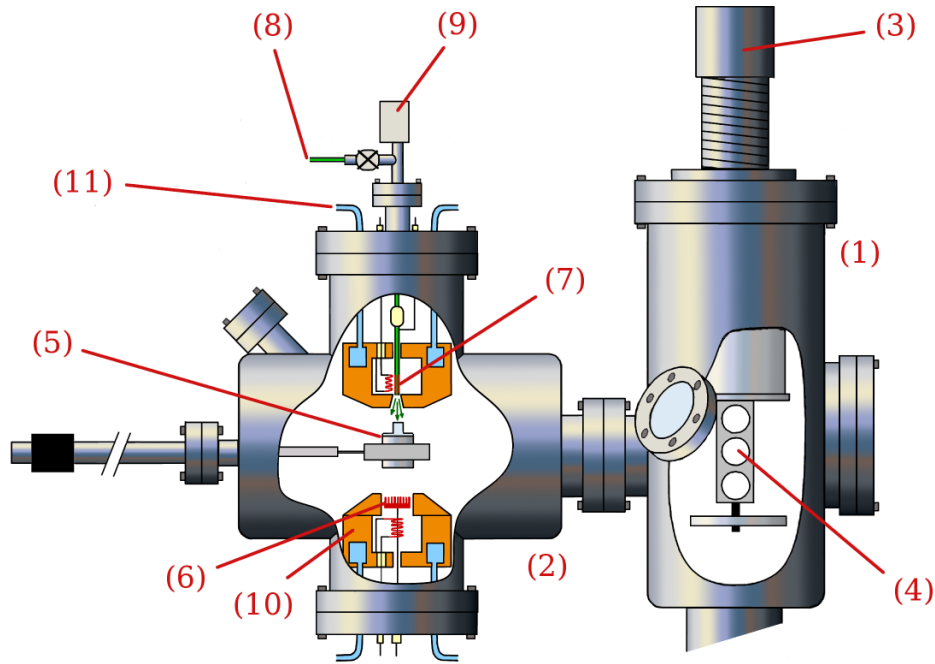


**Figure 3.7:** Side view of the combined loading (1) and atomic hydrogen (2) chambers. The loading chamber houses a transfer module (3) equipped with three photocathode docks (4) that can be retracted into a sealed vessel. Using a system of two magnetic manipulators (one not visible in the picture), a photocathode (5) can be placed between a radiative oven (6) and an atomic hydrogen source based on a hot tungsten capillary (7). The feeding pressure of molecular hydrogen is controlled by a leakage valve (8) and monitored by a Pirani gauge (9). In order to avoid heating of the chamber walls, both the cathode oven (6) and the hot capillary (7) are surrounded by water-cooled copper shields (10 and 11).

by a gate valve (c.f. figure 3.3), the loading and atomic hydrogen chambers form a common vacuum system, pumped by a turbomolecular pump (*Balzers TPU 180H*, 140l/s) to a base pressure of approximately  $5 \cdot 10^{-9}$  mbar.

The *loading chamber* is equipped with a removable transport vessel used to transfer photocathodes to and from the vacuum setup without any contact to laboratory atmosphere. A schematic view of the chamber including the loading module attached to it is shown in figure 3.7. The loading module is equipped with three photocathode docks that can be retracted into a sealed volume. New photocathodes to be loaded into the vacuum setup undergo the HCl wet-chemical etching procedure, described in chapter 2, in a glove box filled with a pure nitrogen protective atmosphere. The cathode loading module can be attached to the glove box and clean photocathodes inserted into its docking positions without exposure to laboratory atmosphere. The sealed vessel is then flanged to the loading chamber, opened and evacuated using the LAH chamber's turbopump. After loading, photocath-

odes usually undergo bakeout in front of the radiative oven of the atomic hydrogen chamber. Restoration of the LAH vacuum conditions after cathode loading takes typically 24 hours. Subsequently, the gate valve towards the preparation chamber can be temporarily opened for cathode transfer without significantly disturbing the UHV pressure in the rest of the photocathode setup.

The *atomic hydrogen chamber* is dedicated to in-vacuum cleaning of oxide-polluted GaAs surfaces by atomic hydrogen exposure, as described in the earlier chapter 2. Following the basic design proposed by Bischel *et al.* [Bis93], the atomic hydrogen cleaning facility has been implemented by Weigel [Wei04]. During this work, the long-term behaviour of photocathodes cleaned by atomic hydrogen exposure could be studied, and the operational parameters of the atomic hydrogen source have been optimised. These findings are presented in a dedicated upcoming section.

### 3.3 Photocathode Currents and Lifetimes

The performance of the Photoelectron Target has seen significant improvements during the time of this work. Enhancements that have been achieved include longer lifetimes of photocathodes in operation, higher electron current intensities, and better real-life reliability of the photoelectron gun. In the period between September 2006 and February 2009, all experiments at the TSR involving the Electron Target have been carried out using electron beams delivered by the photoelectron gun. While the Electron Target's thermionic cathode gun is still the option of choice for experiments requiring highest electron densities, the photocathode electron gun can replace it in most situations. Especially for experiments on low-velocity ion beams, the main advantage of the thermionic cathode over its photoelectric counterpart – its high maximum emission current – vanishes, as the extraction currents of both devices become limited by gun perveance at low electron beam energy.

#### 3.3.1 Lifetime-limiting Effects

All practical enhancements achieved in operation of the photoelectron target stem eventually from an improved durability of the GaAs photocathode's (Cs,O) activation layers. A more durable activation layer either allows to extract higher electron current densities at a given cathode lifetime, or permits to operate the electron gun for a longer time at given current intensity. Enhanced cathode reliability and longevity allow TSR experimenters and Target operators to schedule photocathode

replacements in a flexible manner, and thereby lead to a better overall availability of the Photoelectron Target beam to TSR experiments. The following sections lay out the three main sources of photocathode degradation in the Electron Target setup and describe how these degradation processes are monitored and minimised in order to obtain optimum cathode lifetimes.

### **Electron-Impact-Induced Desorption**

It has been mentioned earlier that excellent vacuum conditions are a strict necessity for successful operation of NEA GaAs photocathodes. Residual gas constituents like  $\text{H}_2\text{O}$  or  $\text{CO}$  destroy the cathode's (Cs,O) layer chemically. Their partial pressures thus have to be reduced to a minimum by careful bakeout of the entire electron gun and Target setup. That having been said, the vacuum conditions in the Electron Target are as excellent as can be expected from a large-volume, room-temperature vacuum chamber. The residual gas pressure at the very location of the photocathode is not measurable, as the intense magnetic field produced by the superconducting coils that surround the electron gun prohibits operation of ionisation gauges in this region of the setup. For similar reasons, no electrical pumping units can be installed in close vicinity of the photocathode. While NEG strips cover the walls of the beam pipe, their pumping speed is limited, as the vicinity of the superconductor material prohibits high-temperature activation during chamber bakeouts. However, the base pressure in neighbouring accessible parts of the Electron Target is known. It is as low as  $1 \cdot 10^{-11}$  mbar in the electron gun chamber, and of a few  $10^{-11}$  mbar in the beam-merging toroid section. While the electron gun is separated by distances of approximately one and two meters, respectively, from both measuring points, the large inner diameter of the electron beam tube (10 cm) permits the assumption that the local pressure at the electron gun is not worse than a few  $10^{-11}$  mbar.

While the vacuum conditions in the TSR are good enough to allow for very long so-called *dark photocathode lifetimes*, operation of the electron gun can itself lead to a pronounced degradation of these vacuum conditions. Upon electron impact, residual gas desorbs from all surfaces that are exposed to the electron beam. The energy deposition rate in affected surfaces is defined by the electric power of the impinging electron beam. Thus, the effect of electron-induced vacuum degradation scales with both, electron energy and current density. Direct electron bombardment of the Target chamber walls must be avoided at any cost. Exposure of a surface to the full beam current subjects it to a highly localised heating power in the order of 1 W and, within a few seconds, leads to a pressure increase by several orders of magnitude. Following accidental beam misalignments, pressures up to  $10^{-6}$  mbar have been recorded in the Electron Target section. Such high residual gas densities compromise the operation of the TSR itself and destroy instantaneously the (Cs,O)

layer of even a freshly activated GaAs photocathode.

Ideally, electrons should be emitted from the photocathode, be extracted and accelerated by the electron gun electrodes, travel along the electron target, and be completely collected by the Faraday cup. Desorption from the latter does not affect the vacuum in the TSR and at the photocathode as the collector section implements differential pumping of the beam-dumping region. More specifically, the electron current extracted at the location of the Pierce shield should ideally be equal in magnitude to the current collected on the Faraday cup. Any non-zero difference indicates the presence of *leak currents* between the cathode and the gun electrodes and/or the grounded vacuum chamber walls. As the magnetic guiding field largely prohibits electron propagation transverse to the beam axis, the major part of the leak currents consists of secondary electrons emitted from the Faraday cup upon impact of the primary beam. While the cup has been designed to be a very efficient electron absorber [Spr04], secondary electrons produced in the cup electrode have a finite probability of escaping from the collector potential. Guided by the magnetic field, these electrons drift back towards the electron gun and impinge in close vicinity of the photocathode, leading to local vacuum degradation. Despite the presence of the guiding field, toroidal drift in the merging and demerging sections deflects the leak electrons laterally, so that they typically hit the electron gun's extraction and acceleration electrodes. By installation of floating picoammeters between the extraction and drifttube electrodes and their respective voltage supplies, the leak current can be measured directly. Observation has shown that the magnitude of this current correlates with the residual gas pressure in the electron gun chamber.

Using the leak current measurement as a proxy signal for electron impact induced vacuum degradation allows to minimise the latter with the help of the Electron Target's beam steerers. Once the electron beam has been aligned to the stored ion beam, the electron beam geometry in the Target's acceleration and interaction sections must not be changed anymore. Under many circumstances, neither can the correction coils of the demerging toroid section be used, as they can disturb the closed orbit of the ion beam in the TSR. Thus, the only available degrees of freedom for leak current minimisation are the beam steerers of the Target's collector section as well as the high-voltages of the collector electrodes themselves. Application of high positive collector voltages of up to 3kV with respect to the electron gun potential reduces the overall leak current intensity as the deeper "trapping potential" decreases the escape probability of secondary electrons. A negatively biased blocking ring electrode at the entrance of the collector further decreases the current leaking from the collector. The blocking electrode potential is set to a negative voltage close to that of the photocathode. Due to the stochastic nature of the ionisation processes involved, the secondary electrons produced at the collector surface have lower kinetic energies than the primary electrons. The primary beam can thus enter

the collector volume, while most of the secondary electrons reflect at the blocking electrode potential, unable to escape. Nevertheless, a small but non-zero fraction of the secondary electrons still drifts back into the Electron Target. The correction magnets of the collector section can be used to deviate the point of impact of this leak beam as far away as possible from the photocathode. The fact that the collector steerers also influence the impact position of the primary beam on the Faraday cup, and thereby the collecting efficiency of the latter does not matter in practical operation: In a real-life experiment, the Target operator first aligns electron and ion beam axes in the interaction section and subsequently adjusts the collector steerer coils and cup voltages in an iterative way, aiming for minimal leak current measured at the extraction and drifttube electrodes of the electron gun. Experiments have shown that the solution of minimum leak current intensity corresponds to optimal vacuum conditions at the electron gun and slowest cathode degradation rate.

### Cryoadsorption at the Cathode Surface

Another prominent (Cs,O) layer degradation mechanism relates to the liquid nitrogen cooling of the photocathode. At estimated temperatures of 100 to 150 K, the photocathode is, apart from the copper coldhead, the coldest surface in the Electron Target. Cryoadsorption enhances the residual gas density at the photocathode surface and accelerates the destruction of the (Cs,O) layer. In closed vacuum setups of small volume, GaAs photocathodes have been used down to a temperature of 4 K without noticeable degradation of the quantum efficiency [Orl00]. In our case, the vacuum system of the photoelectron gun being open towards the TSR and the accelerator facilities, the total residual gas volume is virtually unlimited, such that the cryopumping speed of the cathode becomes a lifetime-limiting factor in our setup. As described earlier, the drifttube electrode, which used to be kept at room temperature in the previous revision of the electron gun design, has been connected to the cooling chain of the other gun electrodes in an effort to enlarge the cryopumping surface area and minimise the amount of residual gas adsorbed by the cathode surface.

Nevertheless, the cooling power applied to the photocathode remains a critical parameter regarding the optimisation of the lifetime of the (Cs,O) layer. Cooling the photocathode improves the temperature of the emitted electron gas by a factor of 2 to 3 compared to room temperature operation. However, too low temperatures – presumably close to that of liquid nitrogen – lead almost instantaneously to a much-accelerated degradation rate of the cathode quantum efficiency. It has been observed that part of this low-temperature induced degradation is *reversible*, i.e. part of the lost quantum efficiency is restored upon throttling the cooling power and rewarming the cathode surface. This behaviour can be understood by postulating

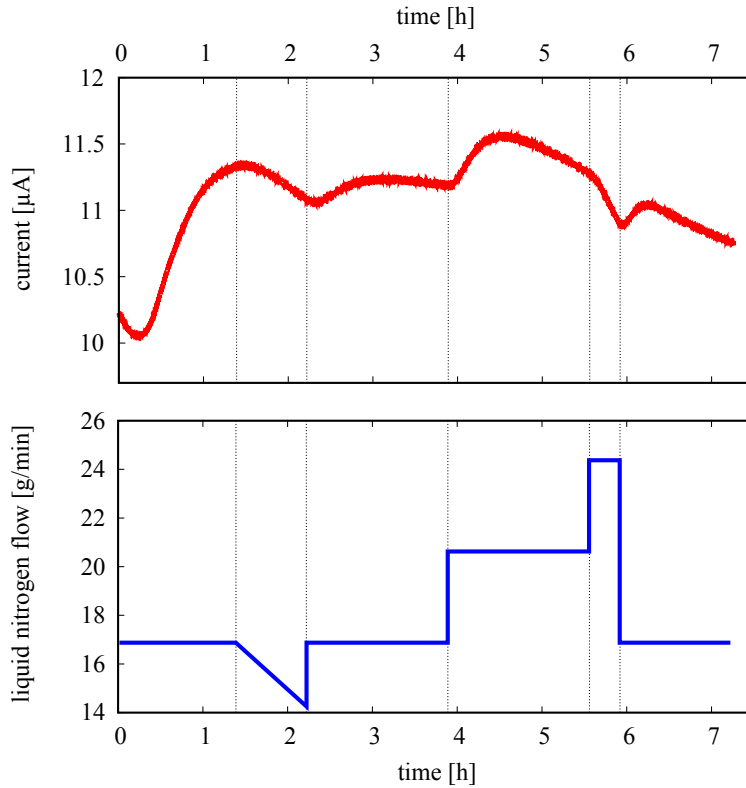


**Figure 3.8:** Emission current of a NEA GaAs photocathode for different liquid nitrogen cooling powers. In normal cathode operation, a liquid nitrogen flow through the coldhead of approximately 17 g/min is used. It is clearly visible that higher nitrogen flows result in steeper degradation of the emission current. The short-term fluctuations of the current following changes in the cooling power result from the temperature dependence of the GaAs bandgap and do not relate to the shape of the (Cs,O) activation layer.

two distinct degradation processes on the molecular level: One part of the cryoadsorbed residual gas constituents (e.g.  $\text{H}_2\text{O}$  and  $\text{CO}_2$ ) *actively* destroys the (Cs,O) monolayer by chemical reaction with the cesium and oxygen on the GaAs surface [Dur96]. This active degradation process irreversibly lowers the magnitude of the NEA, the corresponding loss in cathode quantum efficiency can be restored only by cleaning and subsequent reactivation of the GaAs sample. Other components of the residual gas like CO and  $\text{CH}_4$  adsorb to the cathode surface, but seem chemically inert with respect to the (Cs,O) layer. The presence of these polluting agents decreases the quantum efficiency *passively*, by decreasing the tunnelling probability through the GaAs surface barrier in affected cathode areas. The (Cs,O) structure stays intact and, upon rewarming the cathode, the passive adsorbate sublimates and liberates the blocked cathode area, thus restoring the lost quantum efficiency.

The behaviour of a NEA photocathode subject to changing cooling power is shown in figure 3.8. In this test measurement, the power of the cathode excitation laser has been deliberately decreased to a very low value, such that the cathode operates in *current limited mode*. In this mode, the measured extraction current is strictly proportional to the cathode quantum efficiency, so that the time evolution of the latter can be observed directly. In thermal equilibrium, the time-dependence of the emission current is well described by an exponential decay. The lifetime  $\tau$

of the photocathode is defined as the time after which its quantum efficiency has decreased by a factor of  $1/e$ . The QE degradation rate  $1/\tau$  is a function of the cathode temperature, and thus of the liquid nitrogen flow through the electron gun coldhead. An interpretation of figure 3.8 is complicated by the fact that the cathode temperature influences not only the (Cs,O) degradation rate but also the value of the band gap energy  $E_g$  in the bulk of the GaAs crystal. The dependence of the band splitting on the crystal temperature is described by

$$E_g(T) = E_g(0) - \frac{a T^2}{b + T} . \quad (3.4)$$

The magnitude of the band gap  $E_g$  thus rises as the temperature  $T$  decreases.  $a$  and  $b$  are parameters to be determined empirically [Var67]. A larger band gap leads to stronger band bending close to the (Cs,O) activated surface and thus results in a higher effective Negative Electron Affinity. The initial rise of the emission current visible in figure 3.8 corresponds to the enhancement of the cathode's NEA as it cools from initially 300 K to the nominal operation temperature. The cooling power applied in normal Electron Target operation corresponds to a flow of liquid nitrogen of approximately 17 g/min. Experience has indicated that this represents an optimal tradeoff between low electron temperature and acceptable photocathode lifetime. As visible in figure 3.8, a higher nitrogen flow of 21 g/min leads – after a further initial temperature-induced rise of the NEA – to a significantly faster QE degradation rate once thermal equilibrium is established. Further rise of the nitrogen flow to more than 24 g/min leads almost instantaneously to a steep decline of the emission current. As described above, part of the lost cathode efficiency is restored upon throttling of the nitrogen flow (at  $t = 6$  h).

The sensitive dependence of the photocathode quantum efficiency on the temperature requires reliable control of the liquid nitrogen cooling system. The coolant flow used to be defined in a rather indirect way, by adjusting the supply pressure applied to the liquid nitrogen dewar. Slow drifts of this supply pressure during long-time photocathode operation could eventually lead to warming or undercooling of the GaAs sample. The latter not only shortens the lifetime of the photocathode, but also results in experimentally defavorable fluctuations of the current intensity of the Electron Target. In order to achieve more reliable monitoring and control of the cooling power, an integrated mass flow controller (*Bürkert MFC 8262*) has been installed at the warm end of the nitrogen supply line. The MFC consists of a thermal-capacity gas flow meter coupled to a servo-driven throttle valve and actively stabilises the nitrogen mass flow at a given setpoint. Since installation of this active nitrogen flow regulator, temperature-induced cathode instability is not an issue anymore.

### Electron Impact Residual Gas Ionisation

The last major degradation mechanism is electron impact induced ionisation of residual gas in the Electron Target vacuum chamber. While the vacuum pressure in the beam-merging section is excellent for such a large scale setup (few  $10^{-11}$  mbar all over the length of the TSR), the dominant residual gas constituents have significant electron impact ionisation cross sections at the typical energies of operation of the Electron Target. The dominant residual gas species  $H_2$ ,  $CH_4$ ,  $H_2O$ ,  $CO_2$  and  $CO$  all have impact-ionisation cross-sections of  $10^{-16}$   $cm^2$  or more in the projectile energy range between 45 eV and 500 eV [NIS09a]. Given the usual residual gas pressure of a few  $10^{-11}$  mbar, the typical electron density of  $10^6$   $cm^{-3}$  and the total length of the Electron Target of approximately 4 m, this corresponds to an estimated ion production rate of  $(10^6 \dots 10^7) s^{-1}$ .

Typically, the kinetic energy of the impacting electron is large compared to the ionisation threshold of the residual gas molecule. As a consequence, the momentum transfer to the ionic core is minimal and the initial kinetic energy of the ions produced in the electron beam is small. Trapped by the Target's magnetic guiding field and the space charge potential of the electron beam, and given an thermal velocity, the ions may however drift either into the direction of the collector section or into that of the photoelectron gun. In the latter case, the positively charged ions are strongly accelerated by the electron beam optics. The magnetic field geometry designed to expand the electron beam focusses the positive ions onto a small spot at the centre of the photocathode. Depending on the electron gun potential, ions thus hit the photocathode surface with kinetic energies of hundreds or even thousands of electronvolts. This high energetic ion bombardment does not only destroy the (Cs,O) layer of the cathode, but can also damage the GaAs bulk itself by creating crystal defects. The latter favour electron-hole recombination by cascades through in-gap states, thereby lowering the quantum efficiency of the photocathode irreversibly. In operation of photocathode-based high-energy electron guns, ion-bombardment has been observed to be the main cathode degradation effect [Sin03, Bar07]. While the production rate of ions in the beam depends only weakly on the electron energy, the damage inflicted to the (Cs,O) layer by a given ion flux scales with its kinetic energy and, thus, with the electron gun potential. Hence, we expect the cathode degradation rate to be approximately proportional to the electron beam power.

As shown in figure 3.9, an efficient way to prevent drift of residual gas ions towards the electron gun is the introduction of a positive blocking potential step between the electron gun and the Electron Target volume. As the initial kinetic energies of the ions are small, even a very weak positive potential step of magnitude (1...5) V is sufficient to prevent ions from drifting towards the photocathode to a large extent. For small operation energies of the Electron Target, the electron

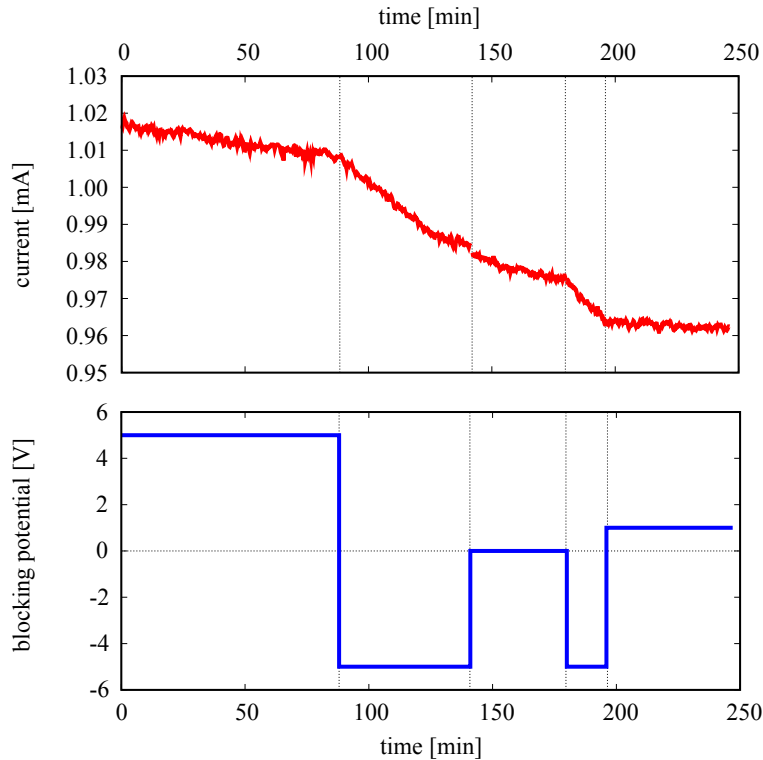


**Figure 3.9:** Emission current of a GaAs photocathode operated in the Electron Target. The test measurement illustrates the effect of photocathode quantum efficiency degradation by residual gas ion bombardment. Introduction of weak positive potentials in front of the electron target significantly reduces the degradation rate by preventing positive ions from drifting towards the electron gun. Application of an (ion-collecting) negative blocking potential even enhances the degradation rate compared to the reference configuration with no blocking electrode.

gun's drift tube electrode can be employed to generate the weak blocking potential. At higher gun voltages, the short distance separating the drift tube from the photocathode prohibits this simple solution. Too fast acceleration is detrimental to the electron beam temperature, as it favours beam heating through longitudinal-longitudinal plasma relaxation (c.f. chapter 4). Thus, in the case of high electron beam energies – starting from a few hundred electronvolts – a set of the Electron Target's acceleration ring electrodes is used to create the positive ion blocking potential. As its kinetic energy is high compared to the ion blocking potential, the Electron Target beam is virtually left unperturbed by the latter.

Figure 3.10 depicts the effects of ion bombardment both on a photocathode protected by an ion-blocking electrode, and a cathode operated without such a protective ion screen. The figures show the current density distribution across the electron beam, measured with the analyser Faraday cup in the collector section. After 5 hours of high current (1 mA) operation at electron energies of approximately 255 eV, the beam profile of the unprotected photocathode is of hollow shape, with a current density practically equal to zero in the very centre of the beam. This characteristic profile arises from the presence of a large non-emitting surface in the centre of the photocathode created by destruction of the (Cs,O) layer by focussed ion bombardment. In contrast, even after 7 hours of operation, the beam profile of the photocathode protected by an ion blocking electrode is as uniform as in freshly

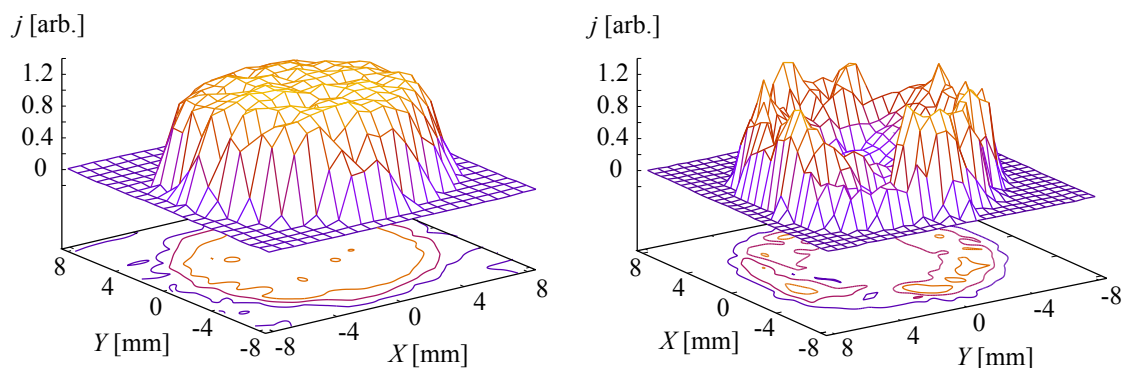


**Figure 3.10:** Electron beam profiles. The plots show the current density distribution  $j$  over the cross-section of the Electron Target beam, measured with a small-aperture analyser Faraday cup. The beam profiles have been recorded after operating the photoelectron gun for 7 and 5 hours, respectively, at a high electron current of 1 mA and an electron energy of 255 eV. The right measurement has been performed with a positive blocking potential protecting the photocathode from ion bombardment. In the case depicted on the left, no blocking potential was present.

activated state, indicating that ion bombardment has been largely suppressed.

### 3.3.2 Electron Target Beam Performance

In a former measurement campaign in 2005, the extraction current of the photocathode had to be limited to approximately 0.2 mA. Higher electron densities would lead to unacceptably short cathode lifetimes. By carefully monitoring and controlling the (Cs,O) layer degradation effects mentioned above, the performance and reliability of the Photoelectron Target could be greatly enhanced. In the period from September 2006 to February 2009, a total of 25 experimental runs have been performed at the TSR, exclusively using the photoelectron gun. Depending on the electron energy, the maximum usable current that can be extracted from the photocathode has been increased to at least 1 mA.

Figure 3.11 shows two examples illustrating the stability of the photoelectron beam at medium and high electron current. The plot on the left is a record of the photoelectron current during an electron-ion recombination experiment on  $\text{HF}^+$  performed at the TSR in September 2007. The average electron beam energy was of 131 eV. As the measurement shows, the electron current was stable at a value of approximately 0.5 mA for almost 40 hours. Obviously, the cathodes (Cs,O) layer did degrade during this time, but as long as the quantum efficiency of the cathode was higher than approximately 1%, the electron gun operated in space charge limited extraction mode. As mentioned earlier, the electron cloud accumulating between

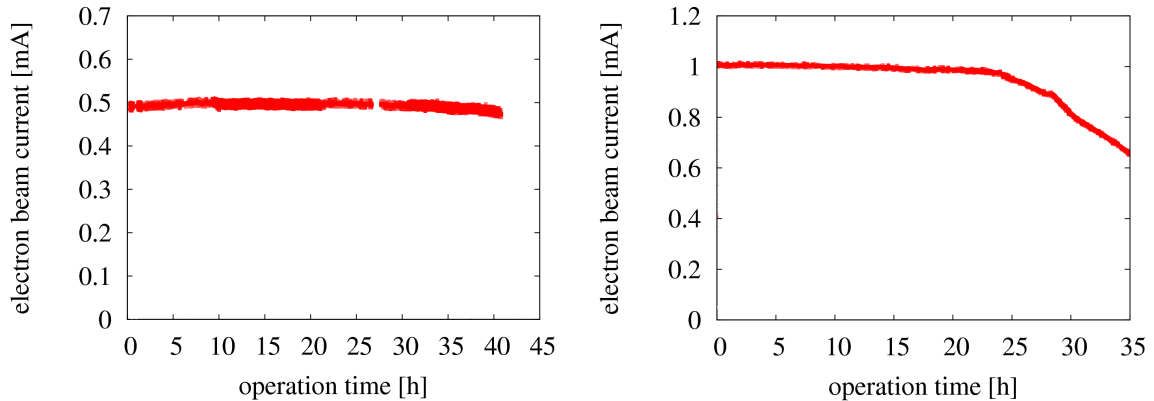


**Figure 3.11:** Two examples of electron beam currents delivered by GaAs photocathodes as a function of the operation time. The left plot depicts a medium electron beam intensity of 0.5 mA, stable over more than 40 hours of operation. In the right example, the electron current has deliberately been measured beyond the point of current-limited extraction for demonstration purposes. Normally this photocathode would have been replaced after approximately 24 h of operation.

the cathode surface and the Pierce electrode acts as an electron buffer which hides underlying changes of the cathode quantum efficiency. Disregarding slow relative drifts in the electron current of a few percent, the electron extraction rate is thus defined by the extraction potential alone.

The plot on the right in figure 3.11 depicts a demonstration run of the photoelectron gun performed in July 2007. At an electron energy of 260 eV, a current of approximately 1 mA could be extracted from the cathode for 23 hours. At that point, the (Cs,O) layer on the GaAs surface – and thereby the cathode’s quantum efficiency – had degraded to a point where the extraction regime of the electron gun changed from space charge limited to current limited mode. As a consequence, the extraction current, no longer stabilised by the buffer effect of the electron cloud, declines proportional to the degrading cathode quantum efficiency. In real-life operation, the photocathode would, at this point, be replaced by a newly activated one from the preparation chamber. For demonstration purposes, the current has, in this case, been measured ten hours beyond the usable operation time of the photocathode.

Figures 3.12 and 3.13 visualise a compilation of Electron Target performances in TSR experiments between June 2007 and July 2008. For the sake of clarity, the dataset has been restricted to the two GaAs photocathodes that were most heavily used during this period. As the scatter plot on the right in figure 3.12 shows, medium electron current intensities  $I$  of (0.3...0.5) mA are currently the most frequently used in TSR experiments. While higher currents of (1...2.5) mA are possible, they are rarely necessary. This is due to the fact, that the major part of the 2007/2008

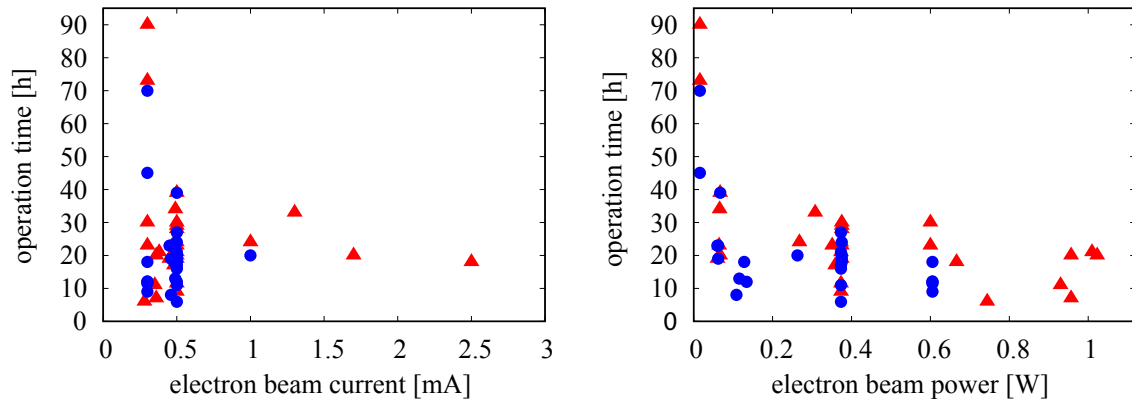


**Figure 3.12:** Cathode operation time versus electron beam current (left) and electron beam power (right). The scatter plots show data from two NEA GaAs photocathode samples used in TSR experiments between June 2007 and July 2008. The two cathodes (red triangles and blue circles, respectively) underwent a total of more than 60 usage cycles during this period.

measurement campaign focussed on electron recombination with molecular ions. Given their low charge-to-mass ratio, molecular ion beams are of high rigidity and can be stored in the TSR at only moderate velocities. The corresponding kinetic energies of the velocity-matched electron beams usually range from 100 eV to 1 keV. At these electron gun potentials and commonly used beam expansion factors  $\alpha$  of 20...30, electron currents of (0.3...0.5) mA correspond to electron particle densities in the electron-ion interaction volume of  $5 \cdot 10^5 \text{ cm}^{-3}$  to  $4 \cdot 10^6 \text{ cm}^{-3}$ , as derived e.g. in [Spr04]. Due to their production mechanism in the MPIK accelerator facilities, the molecular ion beams themselves are of weak intensities. For complex molecules, stored ion currents in the TSR are typically below  $1 \mu\text{A}$ . Often the beam currents even have to be reduced artificially in order to prevent saturation of the neutral-product detector systems. Under these circumstances, electron densities of around  $10^6 \text{ cm}^{-3}$  have proven sufficient for fast electron cooling as well as efficient data taking rate in recombination measurements.

In experiments involving ion beams of very low velocity, the electron current that can be extracted from the photocathode becomes limited by the electron gun perveance. This effect is illustrated in figure 3.13. The slowest beams produced by the two cathodes used in the depicted dataset were emitted by an electron gun potential of only 54 eV and were used to cool a  $\text{CF}^+$  ion beam of kinetic energy 90 keV/u (c.f. chapter 4). At an electron gun perveance of  $1 \mu\text{Perv}$ , the maximum extractable current is of approximately 0.4 mA, independent of the photocathode quantum efficiency and robustness. Thus, at these low electron energies, the photoelectron gun loses its main drawback compared to its counterpart employing a thermionic cathode. While the latter can undeniably deliver much higher electron densities at high electron gun voltage, its maximum beam current is subject to the

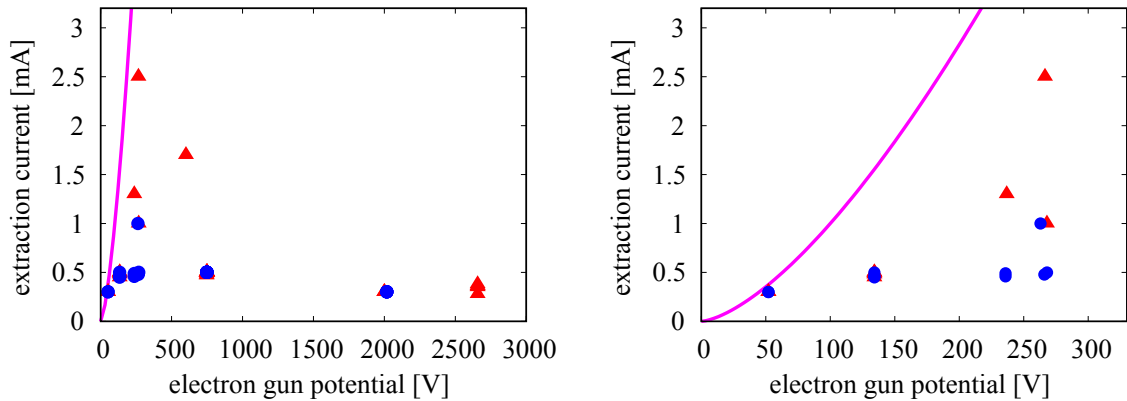


**Figure 3.13:** Extraction current versus electron gun potential for two different NEA GaAs photocathodes used in TSR beamtimes between June 2007 and July 2008. The right figure is a closeup of the energy range below 300 eV. The solid magenta line is the perveance limit for the extraction current assuming a gun perveance of  $1 \mu\text{Perv}$ .

same perveance limit at low extraction potentials.

As shown in the preceding section, degradation of photocathode quantum efficiency by residual gas cryoadsorption has been minimised by installation of the liquid nitrogen flow controller. We thus expect electron-induced desorption and residual gas ionisation to be the dominant remaining degradation mechanisms defining the photocathode lifetime in operation. As indicated in the preceding section, both, the desorption flux and the damage rate inflicted by ion bombardment, not only depend on the current intensity, but also on the energy of the electron beam. Assuming the (Cs,O) degradation rate to be purely proportional to the electric power  $P$  of the electron beam, one expects the photocathode lifetime  $\tau$  to behave approximately like

$$\tau \sim \frac{1}{P}. \quad (3.5)$$

This simple hypothesis is supported by the right plot in figure 3.12 which depicts the operation time of photocathodes as a function of the electron beam power  $P = IU$ .  $U$  is taken to be the electron gun potential corresponding to velocity-matching between electron and ion beams. It should be noted that this is a rather crude approximation of the true average electric power of the electron beam as, in reality, the Electron Target is not only used for electron cooling, but also for recombination measurements at non-zero electron-ion collision energy. Nevertheless, the data is in qualitative agreement with the hyperbolic dependence of the cathode operation time on the electron beam power as expected according to (3.5).

Considering its high perveance-limited electron density, its far lower electron temperature and its long durability at low electron energies, we can conclude that

the GaAs photocathode – while perfectly usable also at high gun potentials of 1 to 3 keV – is currently the electron source of choice for TSR experiments involving slow ion beams.

## 3.4 Long-Time Photocathode Behaviour

Within the scope of the present work, the TSR’s Electron Target has been operated exclusively with the GaAs photoelectron source for two and a half years, in a total of 25 experimental runs. Some of the GaAs samples have been continuously kept in vacuum for more than one year, undergoing more than 100 (Cs,O) activations with subsequent thermal cleaning, and approximately 20 atomic hydrogen treatments. This long period of operation permits to study the long-time behaviour of photocathodes across multiple activation and surface cleaning cycles. More specifically, the cathode data allowed to observe the effect of multiple in-vacuum atomic hydrogen cleanings on the achievable photocathode quantum efficiency.

### 3.4.1 Atomic Hydrogen Cleaning

Photocathodes degraded by usage in the Electron Target gun can undergo thermal cleaning and subsequent reactivation only a few (typically three) times. As stated in chapter 2, we limit the cathode bakeout temperature to (450...470) °C in order to prevent damage of the GaAs surface by preferential As sublimation. In consequence, non-volatile Ga and As oxides accumulate on the photocathode surface and prevent efficient reactivation by renewed (Cs,O) deposition onto the GaAs surface.

The atomic hydrogen chamber of the photocathode setup allows to remove the oxide pollution from the GaAs surface without heating the crystal to dangerously high temperatures and without the need to remove the photocathode from the vacuum setup.

Using a dedicated magnetically-driven manipulator equipped with a cathode holder, a degraded photocathode can be placed between a radiative oven and a source of low-energetic hydrogen radicals (c.f. figure 3.7). The principle of the atomic hydrogen source is based on thermal cracking of dihydrogen molecules in a hot tungsten capillary [Bis93]. Pure molecular hydrogen is fed into a buffer volume through a hot palladium filter. The tungsten capillary, of 6 cm length and of an inner diameter of 0.6 mm, connects the hydrogen buffer volume to the UHV part of the LAH chamber. The hydrogen pressure at the inlet of the tungsten capillary is measured using a Pirani gauge. It can be adjusted by a leakage valve separating the

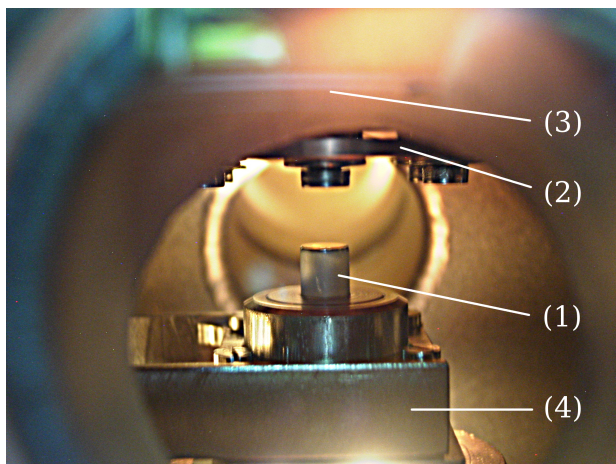


**Figure 3.14:** A photocathode (1) positioned for atomic hydrogen cleaning, seen through the lateral viewport of the atomic hydrogen chamber. On the upper edge of the picture, part of the copper body shielding the hot capillary source can be seen (2), the atomic hydrogen source itself (3) is not visible. The rectangular structure (4) surrounding the cathode is a docking port fixed to the tip of a manipulator in which the cathode is fixed via a bayonet mechanism.

buffer volume from the outlet of the palladium filter. An approximately 2-cm-long section of the capillary is heated by electron bombardment from an adjacent emitter filament. The heating power, easily controllable by the thermionic emission current and the extraction high voltage, is set to 21 W. Pyrometer measurements have shown that this results in a capillary temperature of  $(1610 \pm 25)^\circ\text{C}$ . This temperature is low enough to avoid tungsten sublimation from the capillary, which could pollute the GaAs surface, but also sufficiently high to dissociate (3...10)% of hydrogen molecules passing the capillary, according to studies performed by Tschersich *et al.* [Tsch00, Tsch08]. The photocathode is placed at a distance of approximately 1.5 cm from the capillary outlet. In order to facilitate desorption of the volatile oxide species formed upon reaction with the hydrogen radicals (c.f. equations (2.5) and (2.6)), the photocathode itself can be heated to approximately  $450^\circ\text{C}$  using the radiative oven opposite the hydrogen source. Water-cooled copper shields surround both, the radiative oven and the hot capillary, in order to avoid vacuum-deteriorating heating of the LAH chamber walls.

Figure 3.14 shows a photograph of a GaAs photocathode ready to undergo atomic hydrogen treatment. Usually, the electron bombardment heating of both, the tungsten capillary and the radiative cathode oven, as well as the palladium filter are cleaned by preheating before a photocathode is transferred to the atomic hydrogen chamber. Subsequently, the photocathode is heated to its target temperature of approximately  $450^\circ\text{C}$  for 10 minutes. After that, the heating of the tungsten capillary is switched on and the cathode is exposed to atomic hydrogen for another 10 minutes. The hydrogen dose to which the GaAs surface is subjected during the treatment typically amounts to a few hundred Langmuir units ( $1 \text{ L} = 2.04 \cdot 10^{15} \text{ cm}^{-1}$ ). During the hydrogen cleaning procedure, the pressure in the LAH chamber rises to  $(10^{-7} \dots 10^{-5}) \text{ mbar}$ , depending on the operational parameters of the hydrogen source. Once the hydrogen supply is disabled, the pressure quickly drops back to its nominal value. Usually, Cathode transfer back to the preparation chamber is

possible as early as 10 minutes after hydrogen treatment.

Atomic hydrogen treatment is a widespread surface cleaning technique for semiconductor electron sources [Lan89]. However, research performed by Maruyama *et al.* on GaAs photocathodes designed for delivering polarised electron beams at SLAC have found that repeated atomic hydrogen treatments lead to a steady and irreversible decrease of the achievable quantum efficiency of the cathodes [Mar03]. Similar studies at the polarised electron accelerator CEBAF at Jefferson Laboratory confirmed these findings and, in addition, showed that also the degree of polarisation in the photoelectron beam degraded with increasing number of atomic hydrogen cleaning cycles [Bay05]. While this long-time degradation effect is not fully understood, it is known that both studies employed radiofrequency plasma discharge sources as molecular hydrogen crackers. Such devices are known to deliver neutral hydrogen atoms and protons of relatively high kinetic energies of up to 20 eV [Mat83]. Upon impact on the GaAs surface, these energetic particles may create crystal defects in the bulk and at the surface of the GaAs, lowering the photoelectron escape probability.

We estimate that our atomic hydrogen source, based on low-energetic, *thermal* cracking of  $H_2$ , ensures a more gentle cleaning of the GaAs surface. In the following we show that no photocathode damage arising directly from the hydrogen cleaning procedure is evident for our setup. Still, unnecessary overexposure to hydrogen radicals of the photocathode surfaces should be avoided as long as the origins of possible degradation effects are not fully understood.

### 3.4.2 Calibration of the Atomic Hydrogen Source

In operation of our atomic hydrogen cleaning setup, the only tunable parameters are the molecular hydrogen feeding pressure  $p_i$ , the temperature of the cracker capillary, and the time during which the photocathode is exposed to the H beam. In order to gain insight into the amount of hydrogen radicals reaching the GaAs surface at given operating conditions, the source has been calibrated with the help of studies performed by Tschersich *et al.* on a similar thermal hydrogen cracker. As derived in [Tsch00], the on-axis atomic hydrogen flux density  $\varphi_0$  at a distance  $l$  from the exit of the hot capillary is given by

$$\varphi_0 = \frac{p_i C_c}{k T_R} \cdot \frac{2\sqrt{2} \beta}{1 - \beta + \sqrt{2} \beta} \cdot \frac{1}{l^2 \Omega}. \quad (3.6)$$

The first term in equation (3.6) represents the molecular gas flow rate through the capillary of conductance  $C_c$ . Since  $C_c$  has to be equal to the volumetric gas flow

$\dot{V}$  passing the vacuum gauge at the entrance of the capillary, the Ideal Gas Law indeed requires the molecular particle flow  $\dot{N}_{\text{H}_2}$  into the capillary to be given by

$$\dot{N}_{\text{H}_2} = \frac{p_i C_c}{k T_R} . \quad (3.7)$$

It should be noted that  $T_R$  is *not* the temperature of the hot capillary, but that of the gas volume in which the feeding pressure  $p_i$  is measured. As the heating power of the vacuum gauge is negligible, we consider  $T_R$  to be equal to 300 K.

The parameter  $\beta$  in (3.6) is the degree of molecular dissociation, defined by the equilibrium particle densities  $n_{\text{H}}$  and  $n_{\text{H}_2}$  of atoms and molecules, respectively:

$$\beta := \frac{n_{\text{H}}}{n_{\text{H}} + 2n_{\text{H}_2}} . \quad (3.8)$$

$\beta$  depends both on the temperature and on the total equilibrium pressure inside the capillary. In contrast to the first, the latter cannot be measured. Tschersich thus used the tabulated dependence of  $\beta$  on the temperature to fit the capillary pressure to the measured atomic hydrogen flow rate  $\dot{N}_{\text{H}}$ . Naively, one would expect the latter to be related to the molecular input flow rate  $\dot{N}_{\text{H}_2}$  by  $\dot{N}_{\text{H}} = 2\beta\dot{N}_{\text{H}_2}$ . However, a more accurate treatment, taking into account the different thermal propagation velocities of atoms and molecules through the hot capillary, yields [Tsch00]

$$\dot{N}_{\text{H}} = 2\dot{N}_{\text{H}_2} \frac{\sqrt{2} \beta}{1 - \beta + \sqrt{2} \beta} . \quad (3.9)$$

Hence the second term in equation (3.6) describes the yield of hydrogen atoms at the exit of the capillary per number of hydrogen molecules fed into the system.

Finally, the last term in equation (3.6) normalises the integral atomic hydrogen flux to the cross-section area of the atomic beam at a distance  $l$  from the capillary outlet. Following the definition from [Tsch00],  $\Omega$  is given by

$$\Omega = \int_{2\pi} f(\vartheta) d\omega . \quad (3.10)$$

Where  $\omega$  is the solid angle with respect to the capillary axis and  $f(\vartheta)$  is the angular distribution of atomic hydrogen emerging from the capillary outlet, depending only on the polar angle  $\vartheta$  with respect to the mean emission direction. An analytic form of  $f(\vartheta)$  is given in [Tsch00].  $\Omega$  is the integral of the angular distribution over the full hemisphere into which hydrogen atoms are emitted.  $\Omega$  can thus be interpreted as the solid angular width of the atomic hydrogen beam.

The conductance  $C_c$  of our capillary has been measured at its normal operating temperature of 1880 K. This was done by observing both the molecular feeding

pressure  $p_i$  and the resulting equilibrium pressure  $p_c$  in the atomic hydrogen chamber. Using an effective pumping speed  $S$  of 1151/s, resulting from a reported molecular hydrogen pumping speed of 1401/s of the turbomolecular pump (*Balzers TPU 180H*) and a calculated vacuum pipe conductance of 6701/s, the capillary conductance can be derived as

$$C_c = S \frac{\Delta p_c}{\Delta p_i}, \quad (3.11)$$

where  $\Delta p_c$  and  $\Delta p_i$  denote the pressure differences in the feeding buffer and in the hydrogen cleaning chamber compared to the vacuum conditions with the hydrogen source switched off. The measured values of  $C_c$  are shown in figure 3.15.

Values for the molecular dissociation degree  $\beta$  and the width of the angular distribution  $\Omega$  of the H beam can be extracted from [Tsch00]. However, they rely on the assumption that the angular distribution depends only on the molecular gas feeding pressure but not on the capillary temperature. In [Tsch00] the angular distribution  $f(\vartheta)$  has been measured at high capillary temperatures of 2600 K, where the dissociation degree is almost unity. This distribution was then taken to be valid also at lower temperatures. In addition, the dependence of the degree of dissociation on the capillary temperature has been measured only on-axis with the capillary. The total degree of dissociation  $\beta$  was calculated assuming that the angular distributions of atoms and molecules leaving the capillary were equal. In a recent publication Tschersich *et al.* showed that both of these assumptions were unjustified: Atoms emerge primarily from the hot part of the capillary which lies relatively close to the exit of the latter. On the other hand, molecules originate from any point of the capillary.

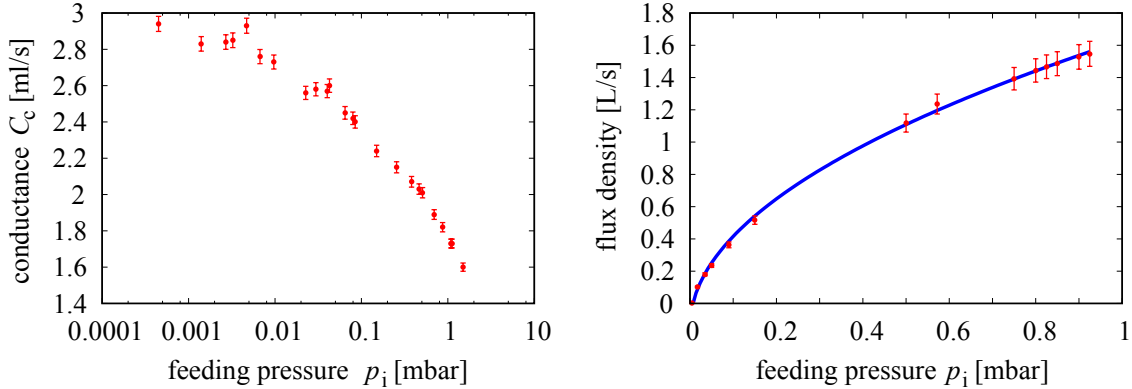


**Figure 3.15:** *Left:* Volumetric conductance of the hydrogen cracker capillary, measured at an operating temperature of 1880 K for different molecular hydrogen feeding pressures  $p_i$ . *Right:* Atomic hydrogen flux density at the location of the photocathode at a capillary temperature of 1880 K as a function of the capillary feeding pressure  $p_i$ , calculated using calibration data from [Tsch00] and [Tsch08] for the degree of molecular dissociation and for the angular distribution of the atomic hydrogen beam emitted from the capillary. The solid blue line is intended as a guide to the eye only.

$p_i$ (mbar)	$C_c$ (ml/s)	$\beta$	$\Omega$ (sr)	$\kappa$	$\bar{\varphi}$ (L/s)
$4.7 \cdot 10^{-3}$	2.8	0.092	0.16	0.85	$3.2 \cdot 10^{-2}$
$5.0 \cdot 10^{-2}$	2.5	0.052	0.21	1.10	$2.3 \cdot 10^{-1}$
$1.5 \cdot 10^{-1}$	2.3	0.043	0.26	1.02	$5.2 \cdot 10^{-1}$
$5.0 \cdot 10^{-1}$	2.0	0.034	0.36	0.88	1.1
$9.0 \cdot 10^{-1}$	1.8	0.030	0.44	0.80	1.5

**Table 3.1:** Parameters of the atomic hydrogen source for a few typical feeding pressures at a capillary temperature of 1880 K.

As a consequence, the angular distribution of atoms is – at a given temperature – broader than that of the molecules [Tsch08]. As can be seen from equation (3.6), whose dependence on  $\beta$  is mostly linear, the combination of a measured flux density  $\varphi_0$  and an *underestimated* beam divergence  $\Omega$  automatically leads to a correspondingly large underestimation of  $\beta$ . The two effects thus nearly cancel each other out. Hence, the true atomic hydrogen flux density  $\varphi_{0,c}$  at distance  $l$  from the capillary is equal to  $\varphi_0$  as given by (3.6) within order 1:

$$\varphi_{0,c} = \kappa \cdot \varphi_0 \quad \text{with} \quad \kappa \approx 1. \quad (3.12)$$

The precise values of the correction factor  $\kappa$  can be derived from the data published in [Tsch08] and, at our capillary temperature of 1880 K, range from 0.8 to 1.1 for molecular feeding pressures  $p_i$  between 0.005 mbar and 0.93 mbar.

In order to estimate the true flux of atomic hydrogen reaching the photocathode surface as accurately as possible, we average the flux density as derived from (3.12) over the solid angle  $\Omega_c$ , spanned by a macroscopic area  $\pi r_c^2$  on the photocathode surface placed at distance  $l$  from the capillary aperture, by defining

$$\bar{\varphi} = \varphi_{0,c} \cdot \frac{\int_{\Omega_c} f(\vartheta) d\omega}{\pi(r_c/l)^2}. \quad (3.13)$$

In the following we average over a solid angle  $\Omega_c \approx 0.031$  sr, spanned by a cathode area of radius  $r_c = 1.5$  mm at a distance  $l$  of 15 mm. Combining (3.6), (3.12), and (3.13), we can finally write

$$\bar{\varphi} = \kappa \cdot \frac{p_i C_c}{kT_R} \cdot \frac{2\sqrt{2} \beta}{1 - \beta + \sqrt{2} \beta} \cdot \frac{1}{l^2 \Omega} \cdot \frac{\int_{\Omega_c} f(\vartheta) d\omega}{\pi(r_c/l)^2} \quad (3.14)$$

for the H radical flux density experienced by photocathodes exposed to our atomic hydrogen source. The plot on the right of figure 3.15 shows equation (3.14), evaluated for various molecular hydrogen feeding pressures  $p_i$ , given the geometry of

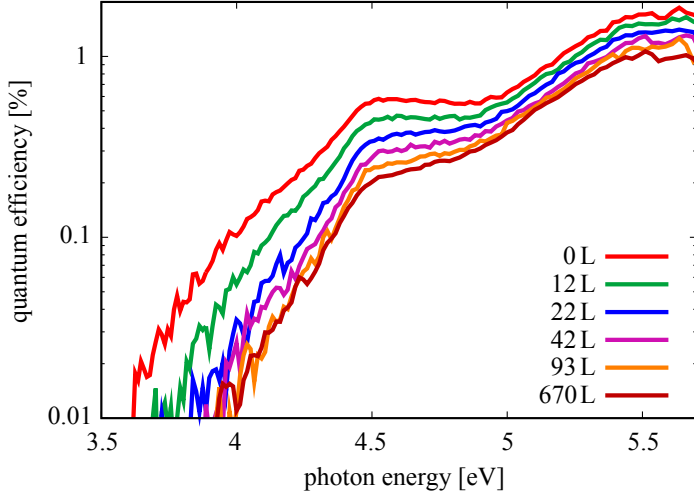


**Figure 3.16:** Spectral response of a GaAs photocathode in the UV range, measured following increasing dose exposures to atomic hydrogen. Up to H exposures of around 100 L, fast decrease in the photocathode quantum efficiency indicates ongoing surface cleaning. At higher doses a saturation effect becomes apparent.

our setup as well as the degree of dissociation  $\beta$ , the angular dispersion  $\Omega$ , and the correction factor  $\kappa$  derived from [Tsch00] and [Tsch08] for the usual operating temperature of our cracker capillary of 1880 K. The errorbars reflect an estimate of the overall accuracy of the calibration of  $\pm 5\%$ . Table 3.1 showcases the parameters entering equation (3.14) as well as the resulting atomic flux densities for a few characteristic molecular hydrogen feeding pressures. This data has also been published in [Orl09a].

### 3.4.3 Spectroscopic Diagnostics of the Cleaning Procedure

Considering the above calibration of molecular hydrogen feeding pressure versus atomic hydrogen flux density, we can find the optimum exposure dose for surface cleaning of GaAs photocathodes. Figure 3.16 shows the spectral response of a photocathode, degraded after multiple (Cs,O) activations, following atomic hydrogen treatments of rising intensity. The response curve marked “0 L” corresponds to the initial state of the cathode, after multiple (Cs,O) activations, usages in the electron gun, and subsequent thermal cleanings in the preparation chamber.

Due to pollution of the GaAs surface by surface oxides, the cathode features significant quantum efficiency in the range of ultraviolet excitation photons of energies ranging from 3.5 eV to 5 eV. Exposure to atomic hydrogen doses of 12 L ( $p_i = 0.017$  mbar for 2 min), 22 L ( $p_i = 0.035$  mbar for 2 min), and 42 L ( $p_i = 0.05$  mbar for 3 min) lead to a fast decrease of the ultraviolet quantum efficiency of the photocathode. At each exposure the electron emission threshold shifts to higher photon energies, which indicates a still ongoing cleaning process.

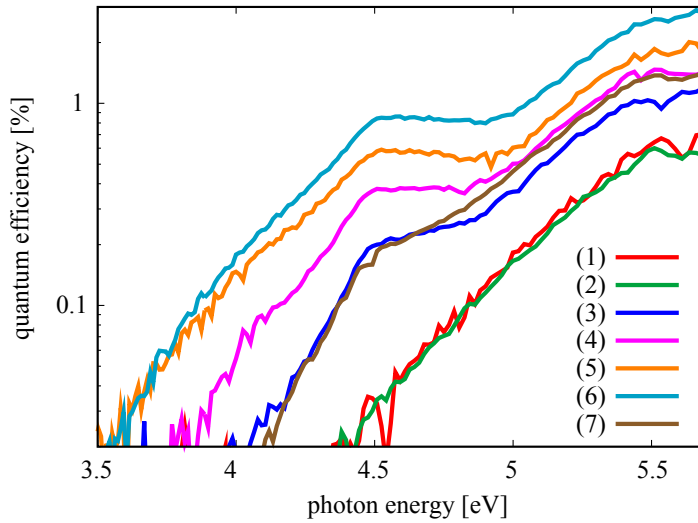


**Figure 3.17:** Spectral response of a GaAs photocathode after chemical surface cleaning in HCl (1), after subsequent H treatment (2), after cesium exposure and subsequent thermal cleaning (3), after three full (Cs,O) activations and subsequent thermal cleanings (4 - 6), and after a final atomic hydrogen treatment without preceding etching in HCl (7).

Starting from a total hydrogen exposure of 93 L ( $p_i = 0.15$  mbar for 3 min), a saturation effect becomes apparent. Further rise of the atomic hydrogen exposure dose to a high value of 670 L ( $p_i = 0.5$  mbar for 10 min), no longer shifts the photoemission threshold to significantly higher energies. We thus conclude that an atomic hydrogen exposure dose of approximately (100...150) L removes practically all non-volatile Ga and As oxides from the photocathode surface.

Figure 3.17 demonstrates the cleaning efficiency of the atomic hydrogen treatment in real-life photocathode operation. The curve (1) in the figure is the UV spectral response of an atomically clean GaAs surface, freshly loaded into the vacuum setup after having been etched in HCl. As one can see, virtually no electron emission takes place at photon energies below 5 eV. Subsequently, the cathode underwent a standard atomic hydrogen treatment of exposure dose 140 L ( $p_i = 0.05$  mbar during 10 min). The resulting spectral response curve (2) is identical to (1), indicating that exposure to the thermal atomic hydrogen beam neither physically nor chemically alters the structure of the GaAs surface on a detectable level.

The cathode was then activated by application of approximately 0.5 monolayers of Cs only – no oxygen was added to the surface – and subsequently thermally cleaned at approximately 450 °C in the preparation chamber. The resulting quantum efficiency spectrum (3) is characterised by a shift of the electron emission threshold to lower photon energies of about 4 eV. It is known that heating of the cathode surface to temperatures below 600 °C cannot remove all Cs atoms from the GaAs surface [Kam91, Kam01]. The spectral response curves (4), (5), and (6) result from standard (Cs,O) activations of the photocathode to maximum quantum efficiency, with subsequent usages in the Target’s electron gun and thermal cleanings in the preparation chamber. Each duty cycle leads to an additional increase of the residual

quantum efficiency of the cathode due to accumulation of cesium and non-volatile surface oxides as described in chapter 2. After three duty cycles, atomic hydrogen cleaning of exposure dose 140 L was performed once more. The resulting quantum efficiency spectrum (7) is very similar to (3), indicating that surface oxides on the cathode have been removed according to equations (2.5) and (2.6), while some residual Cs atoms remain on the cathode surface. The latter however do not inhibit building of new (Cs,O) layers, as photocathode activations following hydrogen treatments yield reproducibly high quantum efficiencies. Moreover, no evidence for accumulation of the residual Cs pollution upon multiple activation and hydrogen cleaning cycles has been observed.

### 3.4.4 Stability of the GaAs Crystals

Former studies of the long-time behaviour of GaAs photocathodes cleaned by atomic hydrogen have observed a steady decrease of the maximum achievable quantum efficiency of the cathodes as a function of the number of atomic hydrogen exposures [Mar03, Bay05]. The fact that the Electron Target has been operated with GaAs photocathodes for several years allowed us to observe the behaviour of individual cathode samples over large numbers of duty cycles and hydrogen treatments.

A photocathode can undergo its normal duty cycle, consisting of (Cs,O) activation, employment in the electron gun and subsequent thermal surface cleaning, typically three times. Further (Cs,O) activations yield much lower cathode quantum efficiencies, as ongoing accumulation of Ga and As oxides increasingly prevents efficient rebuilding of new (Cs,O) layers. Thus, typically at every fourth usage cycle, a GaAs sample undergoes atomic hydrogen treatment, which frees the GaAs surface from oxide pollution. Subsequent (Cs,O) activations yield significantly higher quantum efficiencies than preceding the atomic hydrogen cleaning procedure. For reasons not fully understood, the highest quantum efficiency is usually obtained from the second (Cs,O) activation after hydrogen treatment.

Figure 3.18 shows the behaviour of three photocathodes used in the Electron Target across many atomic hydrogen cleanings. The plot shows the maximum cathode quantum efficiency obtained after each hydrogen cleaning as a function of the integrated atomic hydrogen dose. Two of the cathodes employ GaAs crystals grown in the Metal-Organic Chemical Vapour Deposition (MOCVD) technique while the third has been grown by Liquid Phase Epitaxy (LPE). As can be seen from the plot, the MOCVD cathodes – although achieving very high initial quantum efficiencies (up to 35%) – are characterised by a slow, but steady decrease in electron yield as a function of the number of atomic hydrogen cleaning cycles. Neither higher atomic hydrogen exposures, nor etching in HCl can recover this quantum efficiency loss of

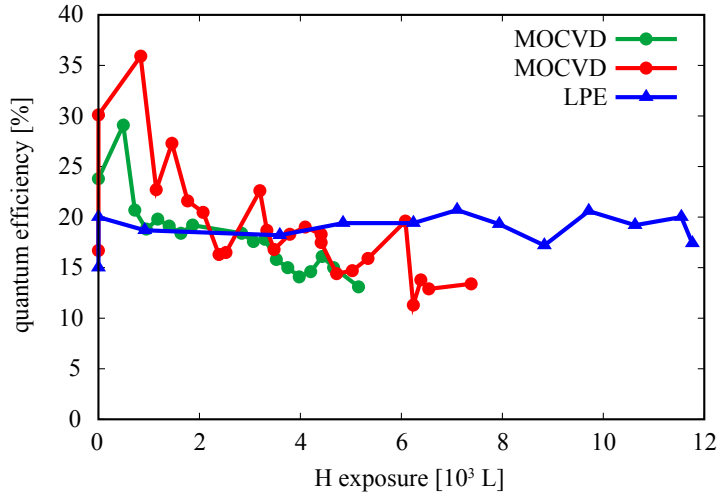


**Figure 3.18:** Long-time evolution of the achievable quantum efficiencies of three GaAs photocathodes as a function of integral atomic hydrogen exposure dose. Two cathode samples have been grown using metal-organic chemical vapour deposition (MOCVD), the other using the liquid phase epitaxy (LPE) technique. For the MOCVD cathodes, a slow but steady decrease of the maximum quantum efficiency is observed, in contrast to their LPE counterpart.

MOCVD cathodes. The LPE photocathode, even though exposed to significantly higher integral dose of atomic hydrogen, features a much more stable behaviour, with a practically constant achievable quantum efficiency of approximately 20%.

Several effects can lead to irreversible loss of cathode quantum efficiency. First, bombardment of the GaAs surface by the atomic hydrogen beam can itself produce crystal defects, thereby lowering the diffusion length of photoelectron through the GaAs. We assume that this effect is responsible for the cathode degradations observed in [Mar03] and [Bay05], as both studies employed plasma-discharge hydrogen crackers known to produce hydrogen atoms of high kinetic energies up to 20 eV [Mat83]. For our thermal hydrogen cracker operating at 1880 K, the kinetic energies of the produced atoms are of a few hundred meV only. Thus, we do not expect crystal damage inflicted by atom bombardment. This assumption is supported by the fact that photocathodes grown by LPE do not suffer from the mentioned degradation effect, even if exposed to much higher atomic hydrogen doses.

Another possible permanent cathode degradation channel relates to thermal cleaning of the GaAs crystals at very high temperatures. It has been shown that heating of photocathodes to 600 °C or higher allows to remove all surface oxides as well as residual cesium atoms from the crystal surface [Kam91, Kam01]. On the other hand, at such high temperatures, sublimation of As has been observed, leading to lattice vacancies at the photocathode surface which are efficient electron-hole recombination centres and thus lower the cathode quantum efficiency [Pie80]. In an effort to avoid As evaporation, we heat our photocathodes to significantly lower temperatures of around 450 °C upon thermal cleaning in the preparation chamber. As

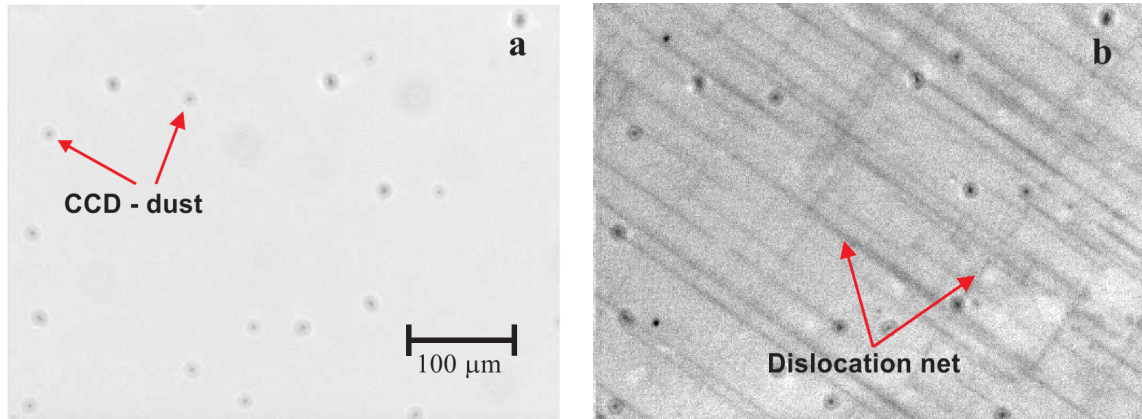


**Figure 3.19:** Microscopic photoluminescence photographs of the surfaces of a GaAs crystal freshly grown using the MOCVD technique (left) and of the MOCVD GaAs sample which has undergone a total of 24 atomic hydrogen exposures and 100 thermal cleanings in the photocathode setup of the Electron Target (right). The grid of dark, orthogonal lines visible in the right picture indicates the presence of a dislocation network in the GaAs lattice, likely introduced by subsection of the crystal to mechanical stress upon heating. The pictures are taken from [Orl09a].

the accumulating non-volatile Ga and As surface oxides can be completely removed by periodic atomic hydrogen cleaning, no net cathode degradation arises from this limited annealing temperature.

However, the GaAs/Al<sub>0.5</sub>Ga<sub>0.5</sub>As/glass heterostructure of the photocathodes is mechanically strained at the interfaces between the compound layers. Heating of the cathode – even at moderate temperatures of 450 °C – introduces additional strain due to the different thermal expansion coefficients of the cathode materials. Along multiple thermal heating processes, this repeated mechanical stress can result in development of dislocations in the GaAs lattice. Like other crystal defects, dislocations lower the quantum efficiency of the photocathode by enhancing the electron-hole recombination probability in the bulk of the crystal.

In order to check whether dislocation defects are indeed responsible for the observed irreversible degradation of quantum efficiency for MOCVD photocathodes, one of the GaAs samples used in the Electron Target was returned to the Institute of Semiconductor Physics in Novosibirsk, where its state has been examined by using a photoluminescence imaging technique [Orl09a]. The cathode was excited by green light and the spatial intensity distribution of emitted photoluminescence photons was recorded using an optical microscope equipped with a low-background CCD camera. As dislocation defects lead to in-gap states in the GaAs band structure, they decrease the photoluminescence emission probability in the same way than they reduce the photocathode quantum efficiency. Dislocation defects thus appear as dark areas in the photoluminescence distribution [Orl09a].

Figure 3.19 shows the results of the photoluminescence imaging. Picture (a) on the left side shows the surface of a freshly-grown MOCVD GaAs photocathode. The photoluminescence distribution is perfectly uniform over the entire field of view of the imaging system. In contrast, the MOCVD photocathode that has been intensely used in the Electron Target features well-pronounced, orthogonal dark lines in its spatial photoluminescence distribution (b). Such a network structure is known to originate from lattice dislocations [Gus98]. In our case these are present most probably at the interface between the  $\text{Al}_{0.5}\text{Ga}_{0.5}\text{As}$  and the GaAs layers [Orl09a].

It is still not clear why MOCVD GaAs photocathodes are more vulnerable to crystal dislocations than their LPE counterparts. MOCVD typically allows to grow crystals of better thickness homogeneity and more sharply-defined layer interfaces compared to LPE [Raz95]. It can however be suspected that the LPE-grown crystal structures are of inherently lower mechanical strain, increasing their robustness against additional stress upon thermal expansion of the cathode heterostructure [Orl09a]. While there seems to be room for optimisation of the robustness of MOCVD-grown GaAs photocathodes, it is safe to conclude that the atomic hydrogen cleaning process itself is not responsible for the slow, irreversible cathode degradation observed over very long operation times. It can thus be considered a viable replacement for the time-consuming photocathode cleaning technique by etching in HCl in almost all situations.



# Chapter 4

## Merged-Beam Physics with Cold Electrons

The technical details of the TSR's Electron Target as well as its performance and reliability in operation with the GaAs photoelectron gun have been described in the preceding chapter. In the following, we lay out the benefits arising from the use of photoelectrons in merged beam experiments. It will be shown that cold electron beams are a necessity for cooling very slow heavy ion beams and a valuable tool in studies of electron-ion recombination at high energy resolution. Both of these applications relate closely to the concept of electron beam temperature in the co-moving frame of the ion beam. Low temperature is the key parameter distinguishing the photoelectron beam from its thermionic counterpart, hence we dedicate a first section to the development of this concept.

### 4.1 Electron Beam Temperature

In a simplified view of the process of electron cooling, the interaction of ion and electron beams can be interpreted as a heat exchange between two gases of different temperatures. For merged beams of equal mean velocity, this picture is remarkably accurate. Being produced much colder than the ions, the electron gas adopts the role of a coolant absorbing heat from the hot ion gas. Even without further theoretical motivation it seems obvious that the cooling rate as well as the minimum equilibrium temperature of the ionic medium depend on the temperature of the electron coolant. For a non-zero difference in the mean velocities of ion and electron beams, the electron cooling process can be treated similarly to the energy loss of charged particles in matter, since the underlying physics of multiple Coulomb scattering is

practically identical. Also in this case, the “stopping force” experienced by the ion beam as it dives into the electron gas, relates closely to the velocity spread, i.e. to the temperature, of the electron medium.

Electron temperature is defined as the *statistical* spread of the electron velocities and the phenomena defining it are laid out in the upcoming subsections. Other effects inducing electron velocity spreads are space-charge screening and beam misalignment. Although the latter are not of inherently statistical nature, we discuss them at this point, as their effects are experimentally often indistinguishable from that of electron temperature.

### 4.1.1 Statistical Energy Distribution

From the discussion in chapter 2 we recall that, in the case of an ideal NEA emission process from the (Cs,O) activated GaAs, the velocity distribution of electrons leaving the cathode surface would be equal to that of the conduction band electrons inside the crystal bulk. Photoexcitation from the valence band takes place deep inside the crystal bulk. As conduction band electrons travel towards the surface, they relax to the point of thermal equilibrium with the GaAs lattice. The temperature of the latter is stabilised by the liquid nitrogen cooling system at an estimated value of (100...150) K. Electrons reaching the (Cs,O) activation layer may thus be assumed to populate a Boltzmann energy distribution of width  $k_B T_c \approx (9 \dots 13)$  meV.

In reality, the emission process is complicated by the inelastic scattering processes already mentioned in chapter 2. Only a very small fraction – approximately 1% – of the electrons reaching the (Cs,O) surface tunnels to the vacuum immediately [Ter95]. The larger part reflects at the potential barrier generated by the (Cs,O) dipole layer, losing energy by inelastic scattering at surface defects. Trapped in the band-bending region, the electrons relax by further phonon emission until they either eventually escape by tunnelling through the (Cs,O) dipole layer or recombine with valence holes by non-radiative cascades. The energy distributions of the electron gas emitted from the (Cs,O) GaAs surface is thus equal to the magnitude of the NEA, which is of (0.1...0.2) eV [Orl01]. Direct measurement has shown that the population density in the energetic region between the vacuum level  $E_{vac}$  and the conduction band minimum  $E_c$  is practically uniform. The population density at energies *above*  $E_c$  is dominated by conduction band electrons emitted by direct tunnelling and is thus given by the Boltzmann distribution of electrons inside the GaAs bulk.

It has been shown that, for photocathodes operated in space-charge limited emission mode, mostly electrons from the Boltzmann-like upper part of the energy distribution contribute to the extracted beam [Orl04]. Electrons from the broad,

low-energetic part of the population are unable to overcome the potential barrier generated by their own space-charge, and stay trapped close to the cathode surface. Hence, it turns out that it is safe to disregard the complications of the NEA emission process and simply assume that the kinetic energies of electrons extracted from the GaAs photocathode initially populate a Boltzmann distribution of a width of approximately 10 meV, as defined by the temperature of the liquid-nitrogen-cooled semiconductor lattice.

### 4.1.2 Temperatures of Magnetised Beams

While the electron cloud initially emitted from the cathode can be assumed to be in thermal equilibrium, its acceleration into the direction defined by the geometry of the electron gun breaks the isotropy of the electron velocity distribution as will be shown below. In addition, the magnetic guiding field of the Electron Target prevents energy transfer between the kinematic degrees of freedom transverse and parallel to the mean flight direction. Thus, for the accelerated electron beam, we define two independent temperatures,  $T_{\parallel}$  and  $T_{\perp}$ , related to the longitudinal ( $\vec{v}_{\parallel}$ ) and transverse ( $\vec{v}_{\perp}$ ) electron velocities with respect of the beam axis [Wol92]:

$$k_{\text{B}}T_{\parallel} = m \left\langle (v_{\parallel} - \langle v_{\parallel} \rangle)^2 \right\rangle = m \left( \langle v_{\parallel}^2 \rangle - \langle v_{\parallel} \rangle^2 \right) , \quad (4.1)$$

$$k_{\text{B}}T_{\perp} = \frac{m}{2} \left\langle (\vec{v}_{\perp} - \langle \vec{v}_{\perp} \rangle)^2 \right\rangle = \frac{m}{2} \left( \langle v_{\perp}^2 \rangle - |\langle \vec{v}_{\perp} \rangle|^2 \right) . \quad (4.2)$$

$m$  is the electron mass, and  $v_{\parallel}$  and  $\vec{v}_{\perp}$  are the longitudinal and transverse components of the velocity vector, respectively. The coordinate system in which the average velocities  $\langle v_{\parallel} \rangle$  and  $\langle \vec{v}_{\perp} \rangle$  vanish will be referred to as the *rest frame* of the electron beam. The additional factor of 2 in (4.2) reflects the fact that two degrees of freedom contribute to  $T_{\perp}$  which is defined as

$$T_{\perp} = \frac{1}{2} (T_x + T_y) , \quad (4.3)$$

where  $T_x$  and  $T_y$  are the temperatures of the two motional degrees of freedom in the plane perpendicular to the electron beam axis.

#### Longitudinal Temperature

Directly after emission from the cathode the velocity distribution of the electrons can be assumed to be isotropic, hence  $T_{\parallel}$  and  $T_{\perp}$  are equal. Acceleration of the electron cloud reduces  $T_{\parallel}$  as can be derived from energy conservation as follows: Consider an electron of initial velocity  $v_{\parallel}$  in the laboratory frame. Let the electron

be accelerated by a potential difference  $U$ . Its kinetic energy in the laboratory frame is then given by

$$E_{\text{lab}} = \frac{m}{2}v_{\parallel}^2 + eU, \quad (4.4)$$

where again  $m$  is the electron mass and  $e$  the elementary charge. Now consider a reference frame moving with velocity  $(2eU/m)^{1/2}$  with respect to the laboratory frame into the same direction as the electron. In this reference frame, the acceleration experienced by the electron due to the potential difference  $U$  vanishes; it is the rest frame of the accelerating beam. We denote by  $v'_{\parallel}$  the (constant) velocity of the electron in this co-accelerating frame. The corresponding kinetic energy is  $E' = \frac{1}{2}mv'_{\parallel}{}^2$ . With the coordinate transform defined above, we can calculate the kinetic energy in the laboratory frame from  $E'$ :

$$E_{\text{lab}} = \frac{1}{2}m \left( v'_{\parallel} + \sqrt{\frac{2eU}{m}} \right)^2. \quad (4.5)$$

Combination of (4.4) and (4.5) leads to

$$v_{\parallel}^2 = v'_{\parallel}{}^2 + 2 v'_{\parallel} \sqrt{\frac{2eU}{m}}. \quad (4.6)$$

If the velocity  $v'_{\parallel}$  of the electron in the beam rest frame is small compared to that of the beam itself, we can neglect higher orders in  $v'_{\parallel}$  on the right hand side, and write

$$v'_{\parallel} \approx \frac{v_{\parallel}^2}{2\sqrt{\frac{2eU}{m}}}. \quad (4.7)$$

Extending this idea to a thermal ensemble of electrons of initial temperature  $k_{\text{B}}T_c$  which is accelerated by a potential difference  $U$ , one derives [Jan90]

$$k_{\text{B}}T_{\parallel} = \frac{(k_{\text{B}}T_c)^2}{2eU} \quad (4.8)$$

for the longitudinal temperature  $T_{\parallel}$  in the comoving reference frame of the accelerated beam.

As  $eU \gg k_{\text{B}}T_c$  for electrons produced at the TSR Electron Target, acceleration significantly reduces the longitudinal velocity spread of electrons in the rest frame of the beam. Equation (4.8) reflects a purely kinematic transformation effect, which is a good approximation of reality as long as the beam electrons can be treated as an ideal gas, i.e. as an ensemble of free, non-interacting particles. For dense and/or cold electron gases, Coulomb interaction between the particles has to be taken into account, which leads to additional contributions to  $T_{\parallel}$  as will be shown in section 4.1.3.

### Transverse Temperature

Kinematic compression of the velocity spread reduces only the electron temperature of the degree of freedom in the longitudinal direction of the beam. The velocity spread along the two degrees of freedom transverse to the mean propagation axis is not affected as transverse coordinates do not change upon transformation from the laboratory to the beam rest frame. However, the transverse temperature of the electron beam can be decreased by a technique known as adiabatic magnetic expansion [Dan94].

In the magnetic guiding field of the Target Section, electrons move on helical trajectories around the magnetic field lines. The angular velocity of their motion in the plane transverse to the direction of the magnetic induction  $\vec{B}$  is given by the *cyclotron frequency*

$$\omega_c = \frac{eB}{m} , \quad (4.9)$$

as one derives from the non-relativistic Lorentz force experienced by the electron. The radius of the helix trajectory is the *Larmor radius*

$$r_c = \frac{mv_{\perp}}{eB} , \quad (4.10)$$

whereas the longitudinal geometry of the trajectory is defined by the *cyclotron length*

$$\lambda_c = 2\pi \frac{v_{\parallel}}{\omega_c} = 2\pi \frac{mv_{\parallel}}{eB} . \quad (4.11)$$

$\lambda_c$  is the longitudinal distance covered by the electron during one cyclotron period.

In a magnetic field of spatially decreasing intensity, a longitudinal component of the Lorentz force arises which accelerates the electron. We say that the decrease of the magnetic induction  $B$  is *adiabatic* if the induction gradient along the longitudinal direction  $z$  is weak compared to complete disappearance of the field over one cyclotron length [Pas96b], i.e. if

$$\left| \frac{dB}{dz} \right| \ll \frac{B}{\lambda_c} . \quad (4.12)$$

In case the condition of adiabatic decrease of the magnetic induction is fulfilled, it can be shown that the electron ensemble is characterised by two adiabatic invariants [Spi62, O'Ne85]:

$$R^2 B = \text{const.} \quad \text{and} \quad \frac{k_B T_{\perp}}{B} = \text{const.} , \quad (4.13)$$

where  $R$  is the radius of the electron beam, not to be confused with the cyclotron radius  $r_c$ . The first invariant quantity in (4.13) states that the radius of the electron beam increases for decreasing magnetic induction, hence the name *adiabatic magnetic expansion*. The final electron beam radius is given by

$$R_f = \sqrt{\frac{B_c}{B_f}} R_c . \quad (4.14)$$

The index c denotes the beam radius and magnetic induction at the location of the cathode, while f stands for the final state after expansion. The second invariant in (4.13) indicates that, during expansion, energy is transferred from the transverse kinetic degrees of freedom to the longitudinal one. Hence, the final transverse temperature of the electron beam after expansion is given by

$$T_{\perp,f} = \frac{B_f}{B_c} T_{\perp,c} =: \frac{T_c}{\alpha} , \quad (4.15)$$

where we have defined the field ratio  $\alpha$  and have made use of the fact that  $T_{\perp,c} = T_c$ . Adiabatic magnetic expansion provides a way to reduce the transverse temperature of the electron beam to values below the cathode temperature  $T_c$ . However, experimentally accessible values of  $\alpha$  are limited. While the Electron Target has been designed to allow field ratios as high as 90 [Spr04], typical values of  $\alpha$  range from 20 to 40.

Energy conservation requires the heat removed from the transverse degrees of freedom to be absorbed by the longitudinal one. While lowering the transverse temperature, magnetic expansion thus enhances the longitudinal one. As can be seen from (4.15), the total amount of heat transferred is equal to  $(1 - \alpha^{-1})k_B T_c$ . Upon acceleration, this additional heat is suppressed by the same longitudinal coordinate transform already discussed above. In analogy to (4.8), we thus write

$$\begin{aligned} k_B T_{\parallel} &= \frac{(k_B T_c)^2}{2eU} + (1 - \alpha^{-1})^2 \frac{(k_B T_c)^2}{2eU} \\ &= \left(1 + (1 - \alpha^{-1})^2\right) \frac{(k_B T_c)^2}{2eU} . \end{aligned} \quad (4.16)$$

Note that, for any realistic values of  $\alpha$  in the range of 20 to 40, the additional factor compared to (4.8) is practically equal to 2. Hence (4.8) can be modified into

$$k_B T_{\parallel} \approx \frac{(k_B T_c)^2}{eU} , \quad (4.17)$$

which is valid in the case of strong adiabatic magnetic expansion of the electron beam.

### 4.1.3 Plasma Relaxation Effects

Up to now, we have treated the electron beam as an ideal gas of non-interacting particles. This is strictly true only in the case of vanishing Coulomb interaction between the electrons, i.e. if the interparticle distances in the electron beam are infinitely large. In reality, potential energy is stored in the electric field between neighbouring electrons which has not been accounted for in the preceding purely kinematic discussions. In addition, Coulomb interactions between neighbouring electrons allow heat transfer between the transverse and longitudinal degrees of freedom which is not possible for isolated particles. A thorough treatment of these effects requires the theoretical instrumentation of plasma physics. Here, we only describe briefly the phenomena involved and refer to other publications for a more detailed discussion [Dik88, Spr04, Les07].

#### Potential Energy Relaxation

Consider two electrons separated by a distance  $r$ . Their potential energy is given by

$$V_{e,e} = \frac{e^2}{4\pi\epsilon_0} \frac{1}{r} . \quad (4.18)$$

For an ensemble of many electrons, the total potential energy stored in the plasma cloud is given by the sum of the potential energies of the individual particles in their common electric field. Although the presence of many electrons obviously leads to deviations from the simple two-particle Coulomb potential at large distances, it is reasonable to assume that the potential energy of a single electron relates to the mean next-neighbour distance  $\langle r \rangle$ :

$$V_{e,\text{plasma}} \sim \frac{e^2}{4\pi\epsilon_0} \frac{1}{\langle r \rangle} . \quad (4.19)$$

Acceleration of an electron cloud initially at rest elongates it along the mean flight direction, as can be easily derived from current conservation, while transverse interparticle distances are kept constant. Acceleration thus breaks the isotropy of the angular distribution of  $r$ . As a consequence, the individual particles are no longer in their energetically most favourable positions relative to their neighbours. In a strongly magnetised beam, the transverse coordinates of the electrons are frozen, the excess potential energy thus relaxes into kinetic energy of the longitudinal degree of freedom only. Hence, the effect is also named *longitudinal-longitudinal relaxation* (LLR).

A calculation of the maximum kinetic energy release in a totally anisotropic plasma yields [Dik88]

$$V_{\text{e,plasma}} = 1.9 \frac{e^2}{4\pi\epsilon_0} n_e^{1/3}, \quad (4.20)$$

where  $n_e$  is the electron density. Note that, since  $n_e^{1/3} = \langle r \rangle^{-1}$ , equation (4.20) is agrees indeed with our guess of the potential energy given by (4.19). The factor 1.9 is the upper limit of LLR heating for a “suddenly” accelerated electron beam. The acceleration section of the TSR’s Electron Target has been designed to allow for “slow”, so-called adiabatic acceleration of the electron beam (c.f. chapter 3). In this case the electrons are given time to continuously adapt their longitudinal equilibrium positions to the changing density distribution of the accelerating beam, which leads to an overall lower kinetic energy release through LLR [Dik88].

We add the heat transfer caused by LLR to equation (4.17), allowing for a smooth acceleration of the electron beam, by writing

$$k_B T_{\parallel} \approx \frac{(k_B T_c)^2}{eU} + C \frac{e^2}{4\pi\epsilon_0} n_e^{1/3}, \quad (4.21)$$

where  $C$  is a parameter describing the adiabaticity of the acceleration process. It is expected to range from  $C = 1.9$  for a “sudden” beam acceleration down to  $C \approx 0.4$  for a perfectly adiabatic process [Dik88].

## Kinetic Energy Relaxation

For the Photoelectron Target, the transverse beam temperature is always much higher than the longitudinal one. Magnetic expansion typically leads to  $k_B T_{\perp} \sim 1$  meV, while acceleration by gun potentials of a few hundred Volts easily reduces  $k_B T_{\parallel}$  down to values of a few tens of  $\mu\text{eV}$  [Orl07].

The unbalanced distribution of heat among the longitudinal and transverse kinetic degrees of freedom tends to homogenise through a process called *transverse-longitudinal relaxation* (TLR). While the presence of a strong magnetic guiding field prohibits such a heat exchange to a large extent, the effect vanishes completely only for infinite magnetic induction.

As electrons move along their helical trajectories, they generate a time-dependent electric field, oscillating with the cyclotron frequency  $\omega_c$ . The energy contained in the transversely oscillating field can be partially transferred to a neighbouring electron if the *distance of closest approach* of the two electrons on their helix trajectories is small enough. Again, as the transverse degree of freedom of both electrons is frozen

by the magnetic field, the energy is practically completely absorbed into excitation of the longitudinal degree of freedom.

A more detailed overview of kinetic energy relaxation is given e.g. in [Spr04]. Theoretical and empirical descriptions of TLR have been elaborated e.g. in [Dik88], [O'Ne85], and [Kra92]. A detailed experimental analysis of the process has been conducted by Lestinsky on high-density electron beams generated using the Target's thermionic cathode electron gun [Les07]. At a guiding field induction of 0.02 T, it has been found that the effect of TLR is completely negligible compared to LLR as long as the mean cyclotron radius  $\langle r_c \rangle$  of the electrons is shorter than the mean interparticle distance  $n_e^{-1/3}$  by a factor of approximately 5 [Les07].

Given the lower transverse temperature and limited current density compared to the thermionic cathode, this condition is always fulfilled for Electron Target beams produced by the photoelectron gun. In the following, we thus neglect kinetic energy relaxation, and adopt equation (4.21) as the complete description of the longitudinal temperature of our photoelectron beams.

#### 4.1.4 Space-Charge Induced Velocity Distribution

The electron velocity distribution is not homogeneous across the beam. The collective electric charge of the electron beam partially screens the acceleration voltage  $U$ . As a consequence, the electron velocity in the centre of the beam is lower than at its surface. Let us assume the electric charge density distribution  $\rho(r)$  to be homogeneous within a sharply-defined radius  $R$  of the electron beam:

$$\rho(r) = \begin{cases} n_e e & (r \leq R) \\ 0 & (r > R) \end{cases} . \quad (4.22)$$

For a carefully adjusted pierce shield, this simple model reflects the true shape of the beam very well, as can be verified e.g. from figure 3.10. From (4.22) one derives the electric potential

$$\phi(r) = \frac{n_e R^2 e}{4\epsilon_0} \cdot \begin{cases} 2 \ln\left(\frac{R_0}{R}\right) + 1 - \left(\frac{r}{R}\right)^2 & (r \leq R) \\ 2 \ln\left(\frac{R_0}{r}\right) & (r > R) \end{cases} , \quad (4.23)$$

where  $R_0$  is the radius of the Electron Target's beam tube. Note that we defined  $\phi(R_0) = 0$ . The space charge induced potential difference  $\Delta\phi_{sc}$  between the surface of the electron beam and its centre is

$$\Delta\phi_{sc} = \phi(0) - \phi(R) = \frac{n_e R^2 e}{4\epsilon_0} . \quad (4.24)$$

For a typical photoelectron density  $n_e$  of  $10^6 \text{ cm}^{-3}$ , the potential difference between the beam centre and its surface is  $\Delta\phi_{\text{sc}} \approx 0.3 \text{ V}$ .

Due to the space charge potential  $\phi(r)$ , the electrons experience an electrostatic force directed radially outwards from the beam axis. While expansion of the electron beam is prohibited by the magnetic guiding field, the Lorentz force induced by the latter leads to a collective rotation of the electrons around the beam axis of angular velocity [Spr04, Bel06]

$$\Omega_{\text{B}} = \frac{\omega_{\text{c}}}{2} \left( 1 - \sqrt{1 - \left( \frac{B_{\text{B}}}{B} \right)^2} \right), \quad (4.25)$$

where  $B$  is the induction of the guiding field.  $B_{\text{B}}$  is the *Brillouin field* defined by

$$B_{\text{B}} = \left( \frac{2 n_e m}{\varepsilon_0} \right)^{1/2}. \quad (4.26)$$

Similar to a rigid body, the entire electron cloud rotates with a common angular velocity  $\Omega_{\text{B}}$  around its axis. This behaviour is referred to as *Brillouin flow* and is characteristic of a magnetically contained, one-component plasma of homogeneous density [Bel06].  $B_{\text{B}}$  is the minimal magnetic induction necessary in order to prevent transverse divergence of the electron beam due to its space-charge potential. For the Electron Target,  $B$  is always much greater than  $B_{\text{B}}$ , so that  $\Omega_{\text{B}}$  is very small compared to the cyclotron frequency  $\omega_{\text{c}}$ . For a typical electron density  $n_e = 10^6 \text{ cm}^{-3}$  and a guiding field induction  $B = 0.04 \text{ T}$ , one finds  $\Omega_{\text{B}} \approx 2.3 \cdot 10^5 \text{ rad/s}$ . At a beam radius of 8 mm, this corresponds to a transverse kinetic energy of approximately 0.4 meV for electrons at the beam surface. For electrons closer to the rotational axis, this space-charge induced transverse kinetic energy is correspondingly lower and vanishes at the centre of the beam.

### 4.1.5 Misalignment Effects

The effects mentioned above define the velocity distribution of the electrons in the restframe of the ion beam in case the mean velocity vectors of ions and electrons coincide. Even if the magnitudes of both velocities are identical, a slight non-collinearity of both beam trajectories changes their relative velocity distribution. Let  $\vec{v}_{\text{i}}$  be the velocity of an ion in the laboratory frame, and  $\vec{v}_{\text{e}}$  that of an electron. Let us assume that the magnitudes of these velocities coincide:

$$|\vec{v}_{\text{i}}| = |\vec{v}_{\text{e}}| =: v \quad (4.27)$$

Misalignment of both trajectories by an angle  $\theta$  leads to a relative velocity whose longitudinal and transverse components are given by

$$\Delta v_{\parallel} = (1 - \cos \theta) \cdot v , \quad (4.28)$$

$$\Delta v_{\perp} = \sin \theta \cdot v . \quad (4.29)$$

$\Delta v_{\parallel}$  and  $\Delta v_{\perp}$  are the longitudinal and transverse velocity differences with respect to the ion beam axis. These velocity components correspond to longitudinal and transverse collision energies of

$$E_{\parallel} = \frac{1}{2} m v^2 (1 - \cos \theta)^2 \quad (4.30)$$

$$E_{\perp} = \frac{1}{2} m v^2 \sin^2 \theta . \quad (4.31)$$

Due to the large mass difference between ion and electron, it is safe to take the reduced mass to be equal to the electron mass  $m$ . For an ideally adjusted Electron Target,  $\theta$  vanishes, and both, (4.30) and (4.31), evaluate to zero. In practice, this ideal situation can be achieved only within a certain accuracy. Instabilities of either the Target beam steerers or the ion beam position in the TSR can lead to time-dependent drifts of  $\theta$  around its optimal value of zero. In addition, localised small inhomogeneities of the magnetic guiding field in the Electron Target may cause local fluctuations of  $\theta$  along the length of the interaction section. We absorb these effects into a common statistical uncertainty on  $\theta$  by writing

$$\theta = 0 \pm \delta\theta . \quad (4.32)$$

Expanding (4.30) and (4.31) up to the fourth order in  $\theta$ , one sees that the uncertainty  $\delta\theta$  of the latter propagates to the collision energies as

$$\begin{aligned} \delta E_{\parallel} &\approx \frac{3}{24} m v^2 (\delta\theta)^4 \\ &= \frac{1}{4} eU (\delta\theta)^4 , \end{aligned} \quad (4.33)$$

$$\begin{aligned} \delta E_{\perp} &\approx \frac{1}{2} m v^2 \left( (\delta\theta)^2 - \frac{1}{3} (\delta\theta)^4 \right) \\ &= eU \left( (\delta\theta)^2 - \frac{1}{3} (\delta\theta)^4 \right) . \end{aligned} \quad (4.34)$$

As usual,  $eU$  is the total kinetic energy of the electrons in the laboratory frame. According to (4.33) and (4.34), a *statistical* uncertainty on the angle  $\theta$  between electron and ion beam results in a spread of the electron energies in the rest frame of the ion beam. This leads to *apparently* higher electron temperatures compared to (4.21) and (4.15).

Due to the high power of  $\delta\theta$  in (4.33), the effect of misalignment is negligible for the longitudinal electron energy spread. For the transverse degree of freedom, however, the effect might be significant. Using (4.34) one e.g. calculates that, for a electron beam energy of 1 keV, a statistical fluctuation of  $\theta$  in the range  $0 \pm 5 \cdot 10^{-4}$  leads to a value of  $\delta E_{\perp} = 0.25$  meV, i.e. to a contribution to the transverse collision energy spread in the same order of magnitude as that caused by the electron temperature.

## 4.2 Low-Temperature Electron Cooling

The basic principle of electron cooling consists of mixing a hot and dilute plasma of ions with a denser and colder plasma of electrons. The Second Law of thermodynamics requires the temperature difference of both gases to relax by heat transfer from the hot to the cold medium until a common equilibrium temperature is reached. In the case of merged-beam electron cooling at ion storage rings, the electron medium is continuously renewed, so that no net heating of the electrons can occur. Thus, it is possible to cool the ion beam down to the restframe temperature of the electron beam.

On the particle level, the cooling proceeds by multiple Coulomb interactions between ions and neighbouring electrons. As the ion beam is initially produced much hotter than the electron beam, every single ion is characterised by a non-zero velocity with respect to the rest frame of the electron ensemble. As the ion moves through the electron plasma, it undergoes multiple Rutherford scattering with electrons. The recoils experienced by the ion sum up statistically to a “friction force” that opposes its motion. The process is very similar to Bragg stopping of ion beams in matter by multiple ionisation, the main difference being that the cooler electrons are free particles not bound to any parent nucleus.

### 4.2.1 The Binary Collision Model

Following the discussion from [Pot90], let us consider the scattering of a single ion of positive charge  $Ze$  on a single electron (c.f. figure 4.1). We adopt a reference frame where the electron is initially at rest. The ion is characterised by a velocity of magnitude  $v_i$  with respect to this reference frame. The total momentum  $\Delta p_{\text{scatt}}$  transferred in the scattering process is given by the attractive electrostatic force

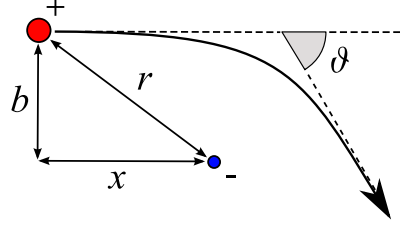


**Figure 4.1:** Scattering of a positively charged ion at an electron.

between the ion and the electron, integrated over all times:

$$\Delta p_{\text{scatt}} = \int_{-\infty}^{+\infty} \frac{1}{4\pi\epsilon_0} \frac{Ze^2}{r^2} dt = \int_{-\infty}^{+\infty} \frac{1}{4\pi\epsilon_0} \frac{Ze^2}{x^2 + b^2} dt . \quad (4.35)$$

As indicated in figure 4.1, the distance  $r$  separating electron and ion can be decomposed into a component  $x$  parallel to the initial trajectory of the ion and a component  $b$  transverse to that trajectory.  $b$  is the *impact parameter*, related to the Rutherford scattering angle  $\vartheta$  by

$$b = \frac{Ze^2}{4\pi\epsilon_0 M v_i^2} \cot \frac{\vartheta}{2} , \quad (4.36)$$

where  $M$  is the ion mass. As (4.35) integrates over all times, the electric field along the longitudinal direction does not lead to a net momentum transfer. It is thus sufficient to consider only the transverse component of the electric force:

$$\begin{aligned} \Delta p_{\text{scatt}} &= \int_{-\infty}^{+\infty} \frac{1}{4\pi\epsilon_0} \frac{Ze^2}{x^2 + b^2} \sin \vartheta dt \\ &= \int_{-\infty}^{+\infty} \frac{1}{4\pi\epsilon_0} \frac{Ze^2 b}{v_i (x^2 + b^2)^{3/2}} dx = \frac{2Ze^2}{4\pi\epsilon_0 v_i b} , \end{aligned} \quad (4.37)$$

where we have substituted  $dt = dx/v_i$ . If the scattering electron has an initial velocity  $\vec{v}_e$  in the chosen reference frame, (4.37) changes into the more general form

$$\Delta p_{\text{scatt}} = \frac{2Ze^2}{4\pi\epsilon_0 u b} , \quad (4.38)$$

where  $u$  is the magnitude of the relative velocity of electron and ion, i.e.

$$u = |\vec{u}| = |\vec{v}_e - \vec{v}_i| . \quad (4.39)$$

The momentum transfer  $\Delta p_{\text{scatt}}$  corresponds to an energy transfer to the electron of

$$\Delta E_{\text{scatt}}(b) = \frac{(\Delta p_{\text{scatt}})^2}{2m} = \frac{2Z^2 e^4}{(4\pi\epsilon_0)^2 m b^2 u^2} . \quad (4.40)$$

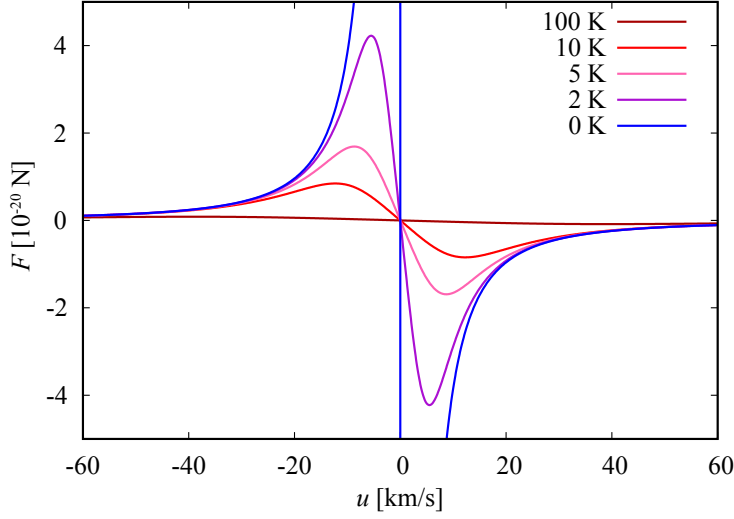


**Figure 4.2:** Friction force  $F$  acting on an ion of charge  $Z = 1$  travelling with velocity  $u$  through an electron gas of density  $n_e = 10^6 \text{ cm}^{-3}$  for different electron temperatures  $T_e$ . The plots are obtained by convolution of (4.42) with a Maxwellian electron velocity distribution of mean  $\sqrt{k_B T_e/m}$ . The electron temperature strongly influences the magnitude of the friction force at low ion velocity.

For an ion travelling through an electron cloud of density  $n_e$ , the differential energy loss  $dE$  per travelling distance  $dx$  is found by integration over all possible impact parameters:

$$\frac{dE}{dx} = -2\pi \int_0^{+\infty} n_e b \Delta E_{\text{scatt}}(b) db = -\frac{4\pi Z^2 e^4 n_e}{(4\pi\epsilon_0)^2 m u^2} \int_0^{+\infty} \frac{db}{b}. \quad (4.41)$$

The momentum transfers from all individual scattering processes thus add up to an overall “stopping force” experienced by the ion as it passes the electron cloud. The integral diverges logarithmically for  $b \rightarrow +\infty$  and  $b \rightarrow 0$ . However, not all impact parameters are physically meaningful, hence we can rewrite (4.41) as [Pot90]

$$\frac{dE}{dx} = -\frac{4\pi Z^2 e^4 n_e}{(4\pi\epsilon_0)^2 m u^2} \int_{b_{\min}}^{b_{\max}} \frac{db}{b} = -\frac{4\pi Z^2 e^4 n_e}{(4\pi\epsilon_0)^2 m u^2} L_C. \quad (4.42)$$

For an electron gas of non-zero temperature, this expression has to be convolved with a Maxwellian electron velocity distribution of mean  $\sqrt{k_B T_e/m}$ . As shown in figure 4.2, the effect of the electron temperature on the friction force experienced by the ion is considerable, especially at low ion velocities, with a colder electron medium resulting in a much higher ion stopping force.

$L_C$  is named *Coulomb logarithm*. The lower integration limit  $b_{\min}$  can be easily determined from (4.38) by considering the case of maximum momentum transfer between electron and ion.  $\Delta p_{\text{scatt}}$  is maximal for a head-on collision between electron and ion and given by  $\Delta p_{\text{scatt,max}} = 2mu_{\max} = 2m(v_i + v_e)$ . Correspondingly, the lower cut-off on the impact parameter is given by

$$b_{\min} = \frac{Ze^2}{4\pi\epsilon_0 m (v_i + v_e)^2}. \quad (4.43)$$

The upper boundary of the integration is defined by the *screening length* [Wol92]

$$b_{\max} := \lambda_{\text{scr}} = \frac{\langle u \rangle}{\omega_p} = \frac{\langle |\vec{v}_e - \vec{v}_i| \rangle}{\omega_p}, \quad (4.44)$$

where  $\omega_p = \sqrt{e^2 n_e / m \varepsilon_0}$  is the *plasma frequency* of the electron gas. In the common rest frame of the electron and ion beams, electrons and ions have mean thermal velocities of

$$\langle v_i \rangle = \sqrt{\frac{k_B T_i}{M}} \quad \text{and} \quad \langle v_e \rangle = \sqrt{\frac{k_B T_e}{m}}. \quad (4.45)$$

As will be motivated below, we consider only cases where the ion's thermal velocity is significantly lesser than that of the electrons. We may thus approximate  $\langle u \rangle \approx \langle v_e \rangle$ , simplifying (4.44) to

$$b_{\max} = \lambda_{\text{scr}} = \sqrt{\frac{\varepsilon_0 k_B T_e}{n_e e^2}} \equiv \lambda_D. \quad (4.46)$$

$\lambda_D$  is the *Debye length* of the electron plasma, depending on temperature  $T_e$  and density  $n_e$  of the electrons. Electron-ion interaction over distances larger than  $\lambda_D$  is screened by closer electrons, impact parameters  $b > \lambda_D$  can thus be neglected. Combining (4.42), (4.43) and (4.46), and using the mean electron and ion velocities from (4.45), the Coulomb logarithm can be expressed by [Ber04]

$$\begin{aligned} L_C &= \ln \left( \frac{b_{\max}}{b_{\min}} \right) \\ &= \ln \left[ 4\pi \left( \frac{\varepsilon_0 k_B}{e^2} \right)^{3/2} \frac{1}{Z} \sqrt{\frac{T_e}{n_e}} \left( T_e + \frac{m}{M} T_i + 2\sqrt{\frac{m}{M}} \sqrt{T_e T_i} \right) \right]. \end{aligned} \quad (4.47)$$

Due to the small ratio  $m/M$ , the dependence of  $L_C$  on the ion temperature  $T_i$  is only weak. For typical values for the Photoelectron Target of  $n_e = 10^6 \text{ cm}^{-3}$  and  $k_B T_e = 1 \text{ meV}$ , and for common ion charge-to-mass ratios, the Coulomb logarithm evaluates to  $L_C \approx 3 \dots 6$ .

Although equations (4.42) and (4.47) neglect the effects of external fields on the scattering processes, they provide an understanding of the electron cooling force that is sufficiently accurate for our purposes. Taking into account the effects of the magnetic guiding field requires a treatment within the framework of plasma theory which is beyond the scope of this text. A discussion of the cooling force in magnetised beams can be found e.g. in [Pot90].

## 4.2.2 Relaxation Time

As early as in 1940, long before electron cooling was considered as a laboratory tool, the following expression for the relaxation time of an electron-ion plasma of partial

temperatures  $T_e$  and  $T_i$  was derived by Spitzer [Spi62]:

$$\tau_{\text{cool}} = \frac{3(4\pi\epsilon_0)^2 m M}{8\sqrt{2\pi n_e} Z^2 e^4} \frac{1}{L_C} \left( \frac{k_B T_i}{M} + \frac{k_B T_e}{m} \right)^{3/2}. \quad (4.48)$$

If the density of the cold electron gas is significantly higher than that of the hot ionic medium and if  $T_e$  can be considered constant, the ion temperature  $T_i$  decreases exponentially towards  $T_e$  with time constant  $\tau_{\text{cool}}$  [Spi62]. In an electron cooler both of these conditions are fulfilled and (4.48) can serve as an approximation for the electron-ion relaxation time.

Although (4.48) is derived formally from plasma physics [Spi62], its general structure can be understood with the help of the binary collision model developed above. As we derived, an ion of velocity  $u$  with respect to the rest frame of the electron gas will feel a decelerating force  $F = dE/dx$  given by (4.42). Accordingly, its velocity changes as

$$\frac{du}{dt} = \frac{F}{M} = -\frac{4\pi Z^2 e^4 n_e}{(4\pi\epsilon_0)^2 m M u^2} L_C. \quad (4.49)$$

Rearrangement and integration over the decreasing velocity from initially  $u_0$  to a final value of 0 leads to the “stopping time”  $\Delta t_{\text{stop}}$

$$\int_{t(u_0)}^{t(0)} dt = -\int_{u_0}^0 \frac{(4\pi\epsilon_0)^2 m M}{4\pi Z^2 e^4 n_e L_C} u^2 du \quad (4.50)$$

$$\Leftrightarrow \Delta t_{\text{stop}} = t(0) - t(u_0) \approx \frac{(4\pi\epsilon_0)^2 m M}{12\pi Z^2 e^4 n_e L_C} u_0^3. \quad (4.51)$$

Note that, in the last step, we have neglected the dependence of the Coulomb logarithm  $L_C$  on the relative velocity  $u$ .

Disregarding the numerical factors, we recognise that equation (4.51) is of exactly the same structure as (4.48). The only real difference lies in the velocity term: Instead of an arbitrarily chosen discrete initial relative velocity  $u_0$ , (4.48) uses the correct expressions for the mean thermal velocities of ions and electrons.

### 4.2.3 Electron Cooling of Slow Molecular Ions

Over the last two decades, electron cooling has become a standard phase-space cooling technique at ion storage rings. Its application to beams of highly-charged atomic ions is particularly well established. The high ratio  $Z/M$  of highly charged ions (of typically  $0.33 \text{ u}^{-1} \dots 1 \text{ u}^{-1}$ ) ensures short cooling times according to (4.48). In addition, it allows to store these ions in magnetic storage rings at convenient

velocities of  $0.1c$  to  $0.5c$ . This corresponds to kinetic energies of the velocity-matched electron cooler beam of 3 keV to 60 keV, which can be easily produced by electrostatic electron guns like the one discussed in this work. Electron velocities close to the speed of light require acceleration potentials in the order of megavolts which are more difficult to achieve instrumentally. Nevertheless, implementations of such high-energy electron coolers for highly relativistic ion beams are currently underway [Mag06, Fed06].

At the MPIK as well as other institutes, there is a rising interest in storage-ring studies on *molecular* ions. Such ions act as catalytic agents in the chemistry of the interstellar medium [Kre05, Her05]. Moreover, processes involving molecules and molecular ions play important roles in the physics of protostellar cloud collapse and of planet formation in circumstellar disks [Her05, Eva03].

Storage rings are ideal tools for systematic studies of molecular reaction dynamics under conditions similar to those in interstellar or circumstellar media. However, electron cooling of molecular ions is challenging. Neglecting the dependence of  $L_C$  on the other parameters, one sees from (4.48) that the electron cooling time behaves essentially like

$$\tau_{\text{cool}} \sim \frac{M T_e^{3/2}}{Z^2 n_e}. \quad (4.52)$$

As we will show later, the thermal velocity of molecular ions is much smaller than that of the electrons and can therefore be omitted. For molecular ions, the charge-to-mass ratio is limited to very small values. In the case of small molecules, consisting of 2 to 4 atoms, it is typically not possible to strip more than one valence electron without breaking the molecular bonds. Hence, molecular ions stored in the TSR usually carry the lowest possible charge of  $Z = 1$ . In contrast to that, the total mass  $M$  can be quite large, especially for polyatomic molecules. Both of these facts lead to larger values of  $\tau_{\text{cool}}$  compared to highly charged atomic ions. In addition, the resulting low ratio  $Z/M$  also limits the maximum velocity at which the molecular ion can be injected into the storage ring:

$$v_{\text{max}} = \frac{Ze}{M} \rho B_{\text{max}}. \quad (4.53)$$

The quantity  $\rho B_{\text{max}}$  is called *maximum rigidity* of a magnetic storage ring.  $\rho$  is the bending radius of the ion beam trajectory in the deflecting sections of the ring and is thus defined by the geometry of the latter.  $B_{\text{max}}$  is the maximum induction of the main dipole magnets. For the TSR,  $\rho B_{\text{max}} \approx 1.5 \text{ Tm}$ . For electrostatic storage rings, like the *Cryogenic Storage Ring* (CSR) presently under construction at MPIK, (4.53) changes into

$$v_{\text{max}} = \left( \frac{Ze}{M} \rho \mathcal{E}_{\text{max}} \right)^{1/2}, \quad (4.54)$$

where  $\mathcal{E}_{\max}$  is the maximum electric field intensity that can be generated by the ring optics. The dependence of the storage velocity on  $Z/M$  is weaker for the electrostatic ring, which is an advantage of this type of machine. Still, in both cases, the maximum ion velocity decreases with the charge-to-mass ratio.

From equation (3.1) we recall that, at low electron velocities, the current  $I$  of the electron gun becomes limited by its perveance, because the voltage  $U$  applied to the extraction electrode can not be significantly higher than the total acceleration potential difference. In first order approximation  $I \sim n_e$ , hence, at low electron cooling velocities,  $\tau_{\text{cool}}$  rises as the available electron density becomes limited by gun perveance. As already discussed in chapter 3, the perveance limit needs to be considered already for the slowest molecules stored in the TSR. For the future CSR, where electron cooling will be applied at kinetic electron energies as low as a few eV, it will be the single limiting parameter for the cooling electron density [Shor].

Thus, in application of electron cooling to slow molecular ions, all parameters entering (4.48) lead to a rise of  $\tau_{\text{cool}}$  compared to the cooling of highly-charged atomic ions. However, too long cooling times are not acceptable as the ion lifetime in the storage ring is limited by the residual gas collision cross section which also rises at low ion velocity. Therefore, low electron temperature is of particular importance for efficient cooling of slow molecular ion beams. Indeed,  $T_e$  is the only parameter in (4.48) that can partially compensate the loss in electron cooling force originating from the low charge-to-mass ratio of molecules.

#### 4.2.4 $\text{CF}^+$ as a Benchmark for Low-Energy Electron Cooling

Up to this date, one of the slowest molecular ions stored in the TSR is  $\text{CF}^+$ . In April 2007, a slow beam of  $\text{CF}^+$  has been stored and electron cooled in the TSR using the Photoelectron Target. The ion beam was produced by a 3 MV single-pass Van-de-Graaff accelerator. Given the mass of CF of 31 u, this results in a specific kinetic energy of approximately 90 keV/u and an ion beam rigidity of approximately 1.3 Tm. This is close to the highest possible rigidity of 1.5 Tm defined by the maximum induction of the TSR's bending magnets. The electron cooling energy, corresponding to velocity matching of the merged beams, was of only 53 eV.  $\text{CF}^+$  was thus considered an interesting benchmark system for the cooler performance of the Photoelectron Target at low electron energy.

The ion currents injected into the storage ring were well below  $1 \mu\text{A}$ . The TSR's built-in beam diagnostics are designed to operate at significantly higher current intensities and could therefore not be used for reliable observation of the  $\text{CF}^+$  cooling process. Instead, a neutral fragment imaging technique was employed as illustrated

in figure 4.3. A fast imaging detector system, implemented after the TSR dipole magnet which follows the Electron Target, is normally used for investigation of the reaction dynamics of molecular ions recombining with electrons [Nov08]. Upon recombination of  $\text{CF}^+$  with an electron, an excited neutral CF molecule is formed which quickly decays into neutral fragments C and F:



Hence, the process is called *dissociative recombination*. The products leave the closed orbit of the TSR and hit a position-sensitive multi channel plate (MCP) detector placed at a distance of approximately 12 m from the Electron Target section. The neutral fragments hit the MCP within opening cones whose base diameters are defined by the beam velocity, the *kinetic energy release*  $E_{\text{KER}}$  of the dissociative recombination process, and the mass ratio of the carbon and fluorine atoms. At an ion beam energy of 90 keV/u, C and F hit the detector within two circles of diameters of 3 and 2 cm, respectively (c.f. figure 4.3). The spatial resolution of the imaging system is of approximately 0.3 mm [Nov, Stü]. For any decay geometry, the heavier F hits the detector closer to the mean beam axis compared to C. Using the distance to the median of the fragment distribution, the detector system is thus able to identify both atomic fragments originating from a recombination event and to compute the position of the *centre-of-mass* of the two particles on the MCP.

After recombination in the Electron Target, the neutral products are no longer affected by the TSR's beam optics. Hence, the width of the centre-of-mass distribution measured by the fragment imaging detector can be used to derive the *transverse emittance*  $\epsilon_i$  of the stored ion beam in the TSR. The latter is defined as the product of the angular dispersion  $\Omega_i$  and the spatial width  $s_i$  of the ion beam along a given degree of freedom  $i$ . The emittance is related to the *betatron amplitude*  $\beta_i(z)$  of the storage ring by

$$\epsilon_i = \Omega_i s_i = \frac{s_i^2}{\beta_i(z)} \quad \text{for } i \in \{x, y\} , \quad (4.56)$$

where the betatron amplitude depends on the longitudinal coordinate  $z$  along the closed orbit of the storage ring [Beu00].

It turned out soon that the TSR's Electron Cooler was not able to cool the  $\text{CF}^+$  beam to a satisfactory degree. The high transverse temperature of the electron beam produced by the Cooler's thermionic cathode gun combined with the severely perveance-limited electron density at an operating voltage of 60 V lead to a cooling time of more than 20 s. Indeed, for the Cooler's beam parameters of  $k_B T_e \approx 10$  meV and  $n_e \approx 1.7 \cdot 10^6 \text{ cm}^{-3}$ , (4.48) evaluates to  $\tau_{\text{cool}} \approx 30$  s. Due to the low velocity in the TSR, the lifetime of  $\text{CF}^+$  itself was of approximately 4 s only, so that no acceptable phase space cooling could be achieved even by the time the ion current intensity had decreased to practically zero by residual gas collisions.

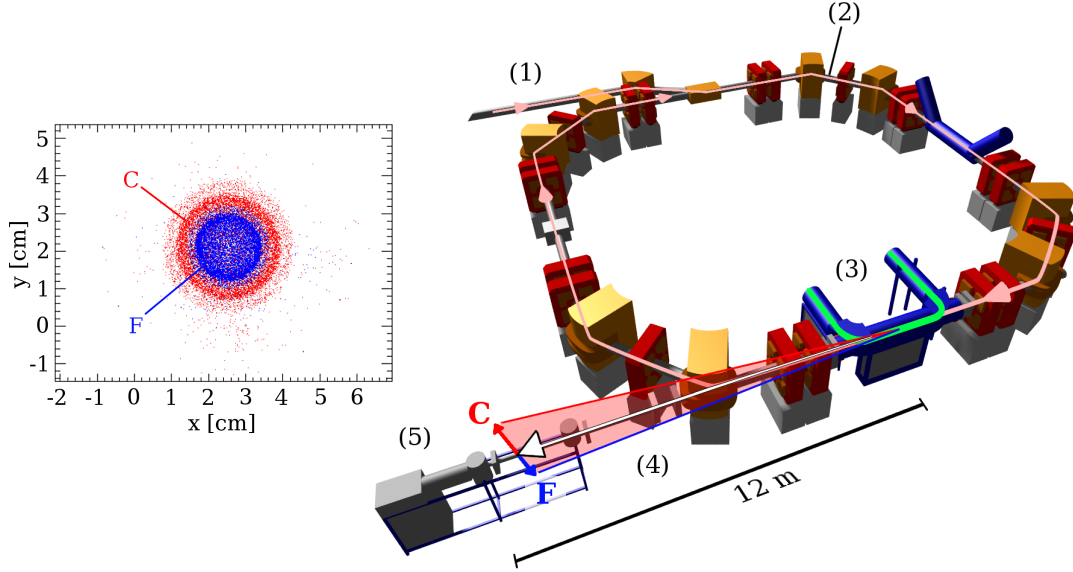


**Figure 4.3:** Principle of the transverse cooling time measurement using the fragment imaging technique. After injection (1), the  $\text{CF}^+$  beam is stored on a closed orbit (2) in the TSR. The Electron Target (3) operates as a cooler of electron energy 53 eV. During electron cooling, a small amount of  $\text{CF}^+$  ions recombines with electrons. The excited CF quickly dissociates into the neutral fragments C and F which leave the closed orbit of the TSR (4). An imaging detector (5) placed at a distance of 12 m from the Electron Target measures the fragments' impact positions on an MCP (scatter plot) and allows to derive the transverse emittance of the original ion beam.

In contrast to that, the Photoelectron Target cooled the  $\text{CF}^+$  beam quite efficiently [Orl07]. Hence, it was used as both, electron target and cooler, throughout the experiments on  $\text{CF}^+$ . The evolution of the beam emittance during electron cooling is shown in figure 4.4. The fragment imaging detector measured the centre-of-mass distribution of C and F on the MCP along the horizontal ( $x$ ) and vertical ( $y$ ) transverse degrees of freedom of the ion beam as a function of storage time in the TSR. In order to prevent saturation of the imaging system, detection started only 1.5 s after ion beam injection into the TSR. Normal distributions of standard deviations  $\sigma_x$  and  $\sigma_y$  were fitted to the centre-of-mass profiles at different storage times. During electron cooling, the width of the centre-of-mass profile shrinks exponentially in both transverse dimensions, and reaches a final width of approximately 1 mm after a few seconds. A fit to the data yields horizontal and vertical cooling times

$$\tau_{\text{cool},x} = (1.45 \pm 0.05) \text{ s} \quad \text{and} \quad \tau_{\text{cool},y} = (1.16 \pm 0.04) \text{ s} . \quad (4.57)$$

Equations (4.48) and (4.47) can be used to derive the electron temperature from these values. As we observe the evolution of the transverse emittance of the ion beam, we identify  $T_e = T_{\perp}$ . The expansion ratio of the photoelectron beam was

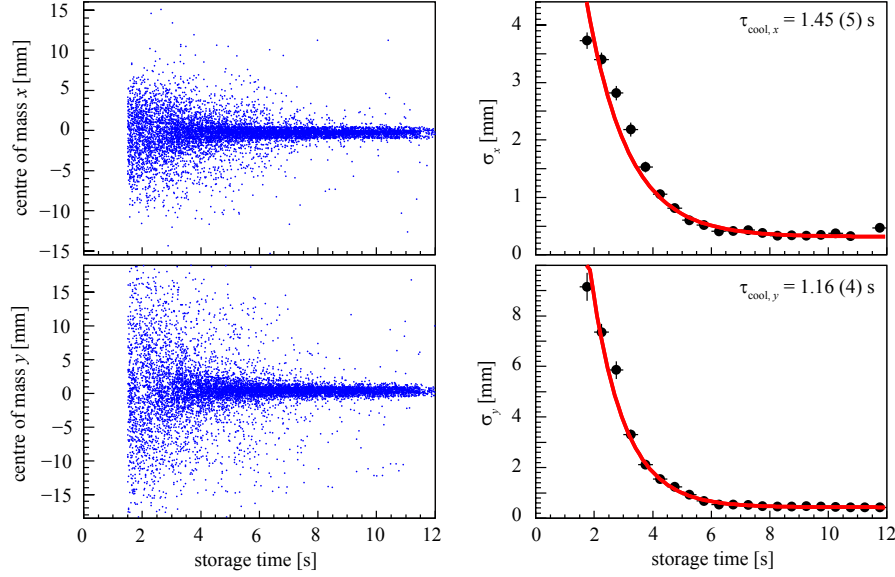


**Figure 4.4:** Electron cooling of a slow beam of  $\text{CF}^+$  stored in the TSR at a specific kinetic energy of approximately 90 keV/u in April 2007. *Left:* Centre-of-mass distribution of C and F fragments on the MCP imaging detector along the horizontal ( $x$ ) and transverse ( $y$ ) degrees of freedom of the ion beam as a function of storage time. *Right:* Standard deviations  $\sigma_{x,y}$  of gaussian fits to the centre-of-mass distributions in both directions as a function of storage time. The solid red line is a fit of the latter assuming exponential shrinking of the beam emittance upon electron cooling. The fitted cooling times  $\tau_{x,y}$  are indicated in the upper right corners.

$\alpha = 20$ , hence we expect a transverse energy spread  $k_{\text{B}}T_{\perp}$  of the electron medium in the order of 1 meV according to (4.15). The initial ion beam temperature is estimated to be 10000 K. Due to the large mass difference between electrons and ions, the ion velocity term in (4.48) is small compared to that of the electrons, so that the influence of the ion temperature on the cooling time is vanishing. The electron target was operated at a current  $I = 0.31$  mA, corresponding to an electron density in the interaction section of  $n_{\text{e}} = 3.5 \cdot 10^6 \text{ cm}^{-3}$ . Inserting the measured values of  $\tau_{\text{cool}}$  into (4.48) and solving the equation for  $k_{\text{B}}T_{\text{e}}$  yields

$$k_{\text{B}}T_{\text{e,eff},x} = (1.5 \pm 0.3) \text{ meV} \quad \text{and} \quad k_{\text{B}}T_{\text{e,eff},y} = (1.3 \pm 0.3) \text{ meV} . \quad (4.58)$$

Note that the value of  $\tau_{\text{cool}}$  obtained from (4.48) has to be scaled by a factor 55.4/1.2, representing the ratio between the TSR's circumference of 55.4 m and the length of the interaction section of 1.2 m.

We call these temperatures “effective” as their derivation relies on the assumption that the physics of the cooling process is entirely described by the simple model developed above. More specifically, we neglect the influence of the geometric size of the ion beam on the electron cooling force. Right after injection, the horizontal

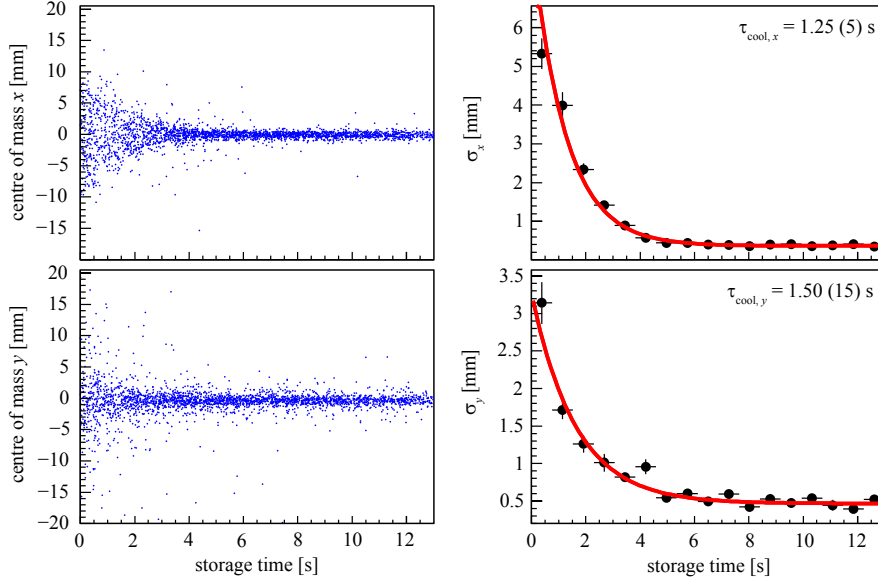


**Figure 4.5:** Electron cooling of  $\text{CF}^+$  performed in February 2008 at an electron current of 0.235 mA, corresponding to an electron density  $n_e \approx 2.9 \cdot 10^6 \text{ cm}^{-3}$ .

diameter of the  $\text{CF}^+$  beam was of approximately 1 cm, i.e. almost as wide as the expanded electron beam. In this case, an imperfect alignment of both beams can lead to a weaker initial cooling force and thus to a longer overall cooling time. In addition, equation (4.48) is valid only for electron cooling in the absence of external fields. The presence of the magnetic guiding field in the target section changes the functional dependence of the energy transfer on the impact parameter  $b$ . According to [Wol92], one expects a relative uncertainty of  $\approx L_C^{-1}$  arising from the simplified calculation of the Coulomb logarithm. Using the operational parameters of the Electron Target and the electron temperature obtained from the measured cooling time,  $L_C$  evaluates in our case to  $\approx 5$ , hence we consider our results to be accurate to 20%.

From the imaging data, we obtain final full widths of the centre-of-mass distributions after electron cooling. A gaussian fit of the data yields standard deviations

$$\sigma_{\text{final},x} = (0.36 \pm 0.02) \text{ mm} \quad \text{and} \quad \sigma_{\text{final},y} = (0.46 \pm 0.02) \text{ mm} \quad (4.59)$$

for the horizontal and vertical transverse directions, respectively. Due to the large distance of 12.24 m separating the imaging detector from the Electron Target, we assume that these widths arise mainly from the projection of the transverse *angular dispersion* of the  $\text{CF}^+$  beam. Neglecting the geometric size of the ion beam, we thus calculate an upper limit for the angular dispersion as

$$\Omega_i = \frac{2\sigma_{\text{final},i}}{12.24 \text{ m}} \quad \text{for } i \in \{x, y\}. \quad (4.60)$$

The horizontal and vertical betatron amplitudes at the location of the Electron Target are  $\beta_x = 3.9 \text{ m}$  and  $\beta_y = 1.5 \text{ m}$ , respectively [Gri07]. According to (4.56),

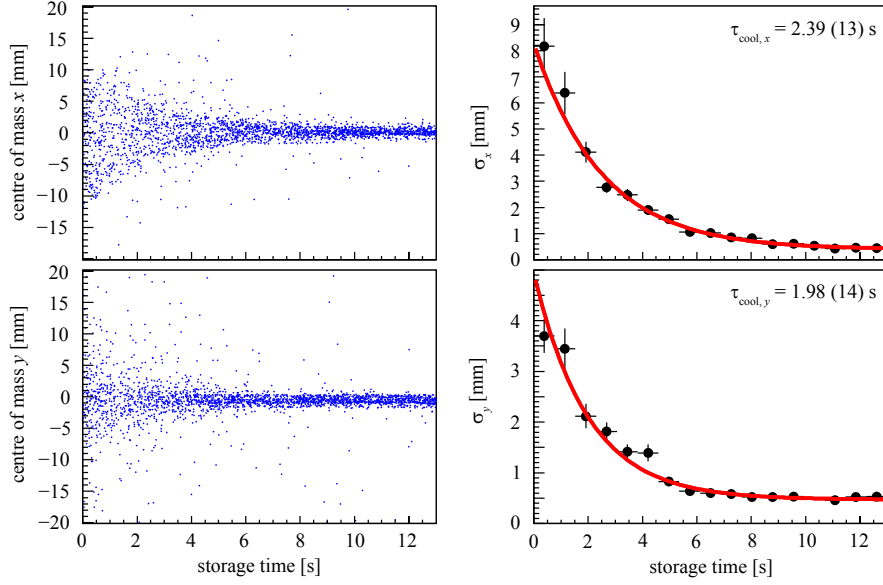


**Figure 4.6:** Electron cooling of  $\text{CF}^+$  performed in February 2008 at reduced electron current of 0.121 mA, corresponding to an electron density  $n_e \approx 1.5 \cdot 10^6 \text{ cm}^{-3}$ .

$\Omega_i \beta_i = s_i$ , we can thus also derive upper limits of the full final width of the ion beam:

$$s_{\text{final},x} = (0.23 \pm 0.02) \text{ mm} \quad \text{and} \quad s_{\text{final},y} = (0.11 \pm 0.01) \text{ mm} . \quad (4.61)$$

Thus, the final width of the stored  $\text{CF}^+$  beam, after a few seconds of electron cooling, is well below 1 mm, which verifies our above assumption. The transverse emittance of the cooled  $\text{CF}^+$  beam evaluates to

$$\epsilon_{\text{final},x} = (0.014 \pm 0.001) \text{ mm mrad} \quad \text{and} \quad \epsilon_{\text{final},y} = (0.009 \pm 0.001) \text{ mm mrad} \quad (4.62)$$

In February 2008, more experiments on  $\text{CF}^+$  were performed at the TSR, providing the opportunity to check the reproducibility of the above findings. Due to technical issues, the Van-de-Graaff accelerator could operate at 2.6 MV only, which lead to an even lower ion-velocity in the TSR, corresponding to an electron cooling energy of 46 eV. Nevertheless, cooling with the Photoelectron Target could be easily established. As shown in figure 4.5, at an electron current  $I = 0.235 \text{ mA}$ , which corresponds to an electron density  $n_e = 2.9 \cdot 10^6 \text{ cm}^{-3}$ , a cooling time similar to the one in the previous experiment has been obtained.

In order to check the validity of the analysis, the electron current was artificially reduced to  $I = 120 \text{ mA}$  ( $n_e = 1.5 \cdot 10^6 \text{ cm}^{-3}$ ). This data is shown in figure 4.6. As expected from the approximate  $1/n_e$ -dependence in equation (4.48), the cooling times rose by approximately a factor of 2.

Table 4.1 shows a compilation of the results of all three  $\text{CF}^+$  cooling experiments. The effective transverse temperatures derived from the different data sets scatter

data set	$\tau_{\text{cool}}$ [s]	$\sigma_{\text{final}}$ [mm]	$n_e$ [ $10^6 \text{ cm}^{-3}$ ]	$L_C$	$k_B T_{e,\text{eff}}$ [meV]	$s_{\text{final}}$ [mm]	$\epsilon_{\text{final}}$ [mm mrad]
04/07: $x$ :	1.45 (5)	0.36 (2)	3.5	5.3	1.5 (3)	0.23 (2)	0.014 (1)
$y$ :	1.16 (4)	0.46 (2)	3.5	5.0	1.3 (3)	0.11 (1)	0.009 (1)
02/08: $x$ :	1.25 (5)	0.42 (2)	2.9	5.0	1.2 (2)	0.27 (2)	0.019 (2)
$y$ :	1.50 (15)	0.52 (3)	2.9	5.2	1.4 (3)	0.13 (1)	0.011 (1)
02/08: $x$ :	2.39 (13)	0.44 (4)	1.5	5.4	1.2 (2)	0.28 (3)	0.021 (3)
$y$ :	1.98 (14)	0.49 (2)	1.5	5.2	1.0 (2)	0.12 (1)	0.010 (1)

**Table 4.1:** Main parameters of the  $\text{CF}^+$  electron cooling tests.  $x$  denotes the horizontal and  $y$  the vertical transverse degree of freedom of the ion beam.  $\tau_{\text{cool}}$  and  $\sigma_{\text{final}}$  are obtained from exponential fits of the standard deviations of the centre-of-mass distribution measured by the fragment imaging system.  $k_B T_{e,\text{eff}}$  are the effective transverse temperatures obtained from (4.48) for the measured values of  $\tau_{\text{cool}}$ . The transverse emittance  $\epsilon$  and the transverse spread  $s$  of the ion beam are computed from (4.56) using  $\Omega = 2\sigma_{\text{final}}/12.24 \text{ m}$ .

within the given uncertainties, which evidences that the 20 %-errorbars are indeed chosen reasonably. However, the average fitted value of the transverse electron energy spread of  $k_B \overline{T}_{e,\text{eff}} = (1.3 \pm 0.2) \text{ meV}$  is significantly larger than the value of approximately  $0.5 \text{ meV}$  which is to be expected for an electron beam produced by a photocathode cooled to  $100 \text{ K}$  and magnetically expanded by a factor  $\alpha = 20$ . Whether this discrepancy is physical, or whether it arises from systematics not taken into account in our simple model of the electron cooling force, is still unclear.

The average temperature obtained from the 2008 data is lower by approximately one standard deviation compared to the 2007 cooling test. This might indicate slightly better electron-ion beam alignment in the more recent experiment which would result in apparently lower electron temperature. Although at the edge of significance, this finding is supported by figure 4.4 where a non-exponential shrinking of the ion beam emittance along the  $x$ -direction can be observed at early storage times.

### 4.3 Electron-Ion Recombination Experiments

While the Photoelectron Target is a valuable tool for cooling of molecular ion beams, its primary purpose is the induction of electron-ion reactions at *non-zero* velocity difference between the merged beams. From November 2006 to January 2009, a total of 25 electron-ion collision experiments have been performed using the Photoelectron Target beam, involving as many as 20 different ionic species in a wide

Ion species	Ion energy [MeV]	$E_{\text{cool}}$ [eV]	$I_e$ [mA]	published in
$^{28}\text{Si}^{3+}$	30	583	0.5	[Sch07]
$^{197}\text{Au}^{25+}$	298	824	0.5	
$^{24}\text{Mg}^{8+}$	94.9	2150	0.5	
$^{25}\text{Mg}^{8+}$	94.9	2067	0.5	
$^{74}\text{Ge}^{28+}$	270	2645	0.3	[Orl09b]
$^{70}\text{Ge}^{28+}$	270	2773	0.3	[Orl09b]
$^{56}\text{Fe}^{17+}$	78.5	773	0.4	
$^{56}\text{Fe}^{17+}$	280	2732	0.4	
$^{56}\text{Fe}^{21+}$	250	2430	0.3	[Kra09]
$^{19}\text{F}^{6+}$	46.4	1350	0.5	
$\text{H}_2^+$	1.0	265	0.5...1	[Nov08]
$\text{H}_3^+$	4.05	735	0.5	[Pet08]
$\text{H}_2^+$	4.9	1327	0.5	
$\text{HF}^+$	4.6	125 *	0.5	[Hof09, Stü]
$\text{CF}^+$	3.0	53 *	0.3	[Nov]
$\text{CF}^+$	2.6	46 *	0.3	[Nov]
$\text{D}_2\text{H}^+$	2.4	327	0.5	
$\text{D}_3\text{O}^+$	4.23	112 *	0.4	[Buh09, Stü]
$\text{CHD}^+$	6.2	231	0.5	
$\text{DCND}^+$	3.1	56 *	0.4	[Men09]

**Table 4.2:** List of ion species on which electron-ion recombination experiments have been performed using the Photoelectron Target, in the period between November 2006 and January 2009. For each species, the table indicates the total kinetic energy at which the ions were stored in the TSR, the corresponding electron cooling energy  $E_{\text{cool}}$ , and the typical Target electron current  $I_e$  that was used in the experiment. A \* denotes experiments where the TSR's Electron Cooler could not be used so that the Photoelectron Target had to be used for beam cooling.

spectrum of charge-to-mass ratios. Table 4.2 lists all ion beams used in electron-ion collision experiments, together with the total kinetic energy at which the ions were stored in the TSR and the corresponding electron cooling energy of the Target beam. The table illustrates the versatility of the Photoelectron Target as an experimental tool. For the reasons discussed in the preceding section, the electron cooling energies required for atomic and molecular beams differ by approximately one order of magnitude. For all experiments denoted by ‘\*’, the stored ion beams were so slow and short-lived that usage of the TSR's Electron Cooler was not possible, as discussed in the previous section. Hence, in these experiments, the Photoelectron Target had to be used for phase-space cooling of the ion beam, in addition to its main task of inducing electron-ion collision reactions. As table 4.2 shows, this was the case for

all molecular ions of masses greater than 20 u.

Measurements on simple di- and triatomic molecular ions like  $\text{H}_2^+$ ,  $\text{HF}^+$ ,  $\text{CF}^+$  and  $\text{H}_3^+$  allowed to derive high-precision rate coefficients for dissociative recombination [Pet08, Nov08] and ion pair formation [Hof09] of these species upon electron impact. In addition, the fragment imaging technique discussed above permitted to identify molecular breakup geometries [Nov08] and final-state branching ratios [Nov] for these reactions. Recently, measurements on complex molecules like  $\text{D}_3\text{O}^+$  or  $\text{DCND}^+$  have become possible by installation of a new neutral-fragment detector system which is sensitive to both position and mass of particles emerging from dissociative recombination events. The ability to identify particle masses allows to study in detail molecular breakup reactions of much higher final-state multiplicity [Buh09, Men09].

The high energy resolution that can be achieved in electron-ion recombination studies employing the cold photoelectron beam has been demonstrated in several experiments performed during the time frame of this work. Precise measurements of *dielectronic recombination* (c.f. section 4.3.3) allow e.g. to probe structure calculations for complex atomic systems with one [Sch07] or many [Kra09, Or109b] valence electrons.

Of particular interest are recombination reactions taking place at *low* collision energies which are not accessible to laboratory-frame experiments. At these low collision energies, the electron temperature in the centre-of-mass frame of the merged beams becomes the limiting factor for the energy resolution of the setup. The following section focusses on accurate determination of the energetic resolving power of the Photoelectron Target, especially at low electron-ion collision velocity.

### 4.3.1 Recombination at Low Collision Velocity

Non-zero electron-ion collision energies are generated by detuning the mean velocity of the target electron beam  $\vec{v}_e$  with respect to that of the stored ion beam  $\vec{v}_i$ :

$$\vec{u} = \vec{v}_e - \vec{v}_i. \quad (4.63)$$

Ideally, the inclination angle between both beams is zero. In this case the electron-ion collision energy  $E_{\text{cm}}$  in the centre-of-mass frame of electron and ion can be calculated in the non-relativistic approximation as

$$\begin{aligned} E_{\text{cm}} &= \frac{1}{2} m u^2 \\ &= \left( \sqrt{E_e} - \sqrt{\frac{m}{M} E_i} \right)^2, \end{aligned} \quad (4.64)$$

where  $E_e$  and  $E_i$  are the mean kinetic energies in the laboratory frame of electron and ion, respectively. Note that we have identified the reduced mass of the collision process with the electron mass  $m$ . Due to the large difference between the ion mass  $M$  and the electron mass  $m$ , this is a reasonable approximation. The relativistically correct expression for the collision energy that is used for data analysis can be found e.g. in [Spr04].

The collision energy vanishes for

$$E_e = E_{\text{cool}} := \frac{m}{M} E_i \quad (4.65)$$

which we refer to as the “cooling energy”. Expanding (4.64) up to the second order around  $E_e = E_{\text{cool}}$ , we obtain

$$E_{\text{cm}} \approx \frac{M}{m} \frac{(E_e - E_{\text{cool}})^2}{4E_i}, \quad (4.66)$$

valid for small velocity detuning of the Electron Target beam. Disregarding the energy dependence of the electron beam’s space charge potential, the laboratory frame energy detuning  $(E_e - E_{\text{cool}})$  of the electron beam is defined by the voltage difference  $\Delta U$  applied to the electron gun compared to the gun potential at cooling velocity. Hence, for small detuning, the collision energy in the centre-of-mass frame of the merged electron-ion beam relates to the measured quantity  $\Delta U$  as  $E_{\text{cm}} \sim (\Delta U)^2$ .

Due to this square dependence, very small collision energies can be measured with high accuracy. E.g. for an electron cooling energy of 2 keV, a measured detuning of the electron gun by 10 V translates to an electron-ion collision energy of approximately 10 meV. This ability to generate very low collision energies with high precision and accuracy is a unique feature of the merged-beams technique.

### 4.3.2 Merged-Beams Energy Resolution

Form (4.66) follows that experimental uncertainties  $\delta E_e$  and  $\delta E_i$  in determination of the laboratory frame energies of electrons and ions propagate to  $E_{\text{cm}}$  as

$$\begin{aligned} \delta E_{\text{cm}} &= \sqrt{\left(\frac{dE_{\text{cm}}}{dE_e} \delta E_e\right)^2 + \left(\frac{dE_{\text{cm}}}{dE_i} \delta E_i\right)^2} \\ &= \frac{M}{4mE_i} \left(E_e - \frac{m}{M} E_i\right) \sqrt{4E_i^2 (\delta E_e)^2 + \left(E_e + \frac{m}{M} E_i\right)^2 (\delta E_i)^2}. \end{aligned} \quad (4.67)$$

More specifically, one expects the accuracy of the collision energy  $E_{\text{cm}}$  in the centre-of-mass frame to improve linearly with decreasing energy detuning  $(E_e - E_{\text{cool}})$  of

the target electron beam in the laboratory frame. At the point of velocity matching, i.e. at  $E_e = E_{\text{cool}}$ , the impact of the laboratory frame energy uncertainties on the determination of  $E_{\text{cm}}$  vanishes. However, at small detuning velocities, the resolving power of the setup becomes limited by other factors.

### Ion Beam Dragging

The generation of a non-zero relative velocity  $\vec{u}$  between electrons and ions by detuning the Electron Target beam to  $E_e \neq E_{\text{cool}}$  leads to a friction force applied to the stored ions given by (4.42). As shown in figure 4.2, this force has a maximum at small velocity detuning between the two beams. As a consequence, the ion beam is *accelerated* towards the velocity of the electron beam. We refer to this unwanted behaviour as “dragging” of the stored ions by the Electron Target beam. In experiments with a single merged-beam section, ion dragging can be reduced by fast switching of the electron beam energy  $E_e$  between the cooling point  $E_{\text{cool}}$  and the energy corresponding to the collision velocity of interest. As has been demonstrated in [Les07], the switching of the electron gun voltage can be done within a few ms, even for energy detuning ( $E_e - E_{\text{cool}}$ ) in the order of magnitude of a keV.

While the fast switching of the electron beam energy can prevent exposure of the ion beam to a net dragging force to a large extent, electron-induced changes of the ion energy  $E_i$  remain the dominating uncertainty on the collision energy  $E_{\text{cm}}$  in merged beam experiments employing a single merged electron beam [Kie04]. In the twin merged-beam setup at the TSR, the presence of the dedicated Electron Cooler fixes the mean energy  $E_i$  of the ion beam even for small velocity detuning of the Electron Target [Spr04, Les07]. The effect of ion-beam dragging on the collision energy resolution is thus negligible for measurements where both electron beams can be used.

### Electron Temperature

At small detuning velocity, the precision in the determination of the electron-ion collision energy is limited by the thermal energy spread of the electrons in the centre-of-mass frame of the merged beams. In the restframe of the ion, the velocities of the electrons are distributed following an anisotropic Gaussian

$$f(\vec{v}_e, u) = \sqrt{\frac{m^3}{(2\pi k_B)^3 T_{\parallel} T_{\perp}^2}} \exp\left(-\frac{m(v_{\parallel} - u)^2}{2k_B T_{\parallel}} - \frac{mv_{\perp}^2}{2k_B T_{\perp}}\right). \quad (4.68)$$

$v_{\parallel}$  and  $v_{\perp}$  are the longitudinal and transverse components of the velocity vectors of the electrons in the mean rest frame of the electron beam.  $u$  is the relative velocity between electrons and ions.  $T_{\parallel}$  and  $T_{\perp}$  are the longitudinal and transverse temperatures of the electron beam in the comoving frame as defined earlier.

Let  $\sigma_{\text{rec}}(u)$  be the cross-section for electron-ion recombination as a function of the collision velocity  $u$ . We define the velocity-dependent *recombination rate coefficient*  $\alpha_{\text{rec}}$  as

$$\alpha_{\text{rec}}(u) := \langle u \sigma_{\text{rec}}(u) \rangle = \int_0^{+\infty} \sigma_{\text{rec}}(v_e) v_e f(\vec{v}_e, u) d^3 v_e . \quad (4.69)$$

The recombination rate coefficient is related to the production rate  $R_p$  of recombined ions measured by a counting detector at the exit of the interaction section [Kil92]

$$\alpha_{\text{rec}} = \frac{R_p}{N_i n_e \eta} \gamma_i , \quad (4.70)$$

with  $N_i$  being the total number of stored ions,  $n_e$  the electron density and  $\eta$  the ratio between the length of the interaction section and the circumference of the TSR.  $\gamma_i$  is the Lorentz factor for the stored ion beam which is important only for fast highly charged ion beams.

For a resonant recombination reaction taking place with probability  $\sigma_0$  at a discrete collision velocity  $u_0$ , i.e. for  $\sigma_{\text{rec}}(u) = \sigma_0 \delta(u - u_0)$ , the convolution (4.69) can be calculated analytically and yields [Kil92]

$$\alpha_{\text{rec},\delta}(u) = \frac{\sigma_0 u_0}{2m \langle v_e \rangle_{\perp}^2 \zeta} \exp\left(\frac{u_0^2 - u^2 \zeta^{-2}}{2 \langle v_e \rangle_{\perp}^2}\right) \cdot \left[ \operatorname{erf}\left(\frac{u_0 + u \zeta^{-2}}{\sqrt{2} \langle v_e \rangle_{\parallel} \zeta^{-1}}\right) + \operatorname{erf}\left(\frac{u_0 - u \zeta^{-2}}{\sqrt{2} \langle v_e \rangle_{\parallel} \zeta^{-1}}\right) \right] . \quad (4.71)$$

where  $\langle v_e \rangle_{\parallel}$  and  $\langle v_e \rangle_{\perp}$  are the mean thermal velocities of the electrons along the longitudinal and transverse directions as defined in (4.45). The parameter  $\zeta$  is defined as  $\zeta := (1 - T_{\parallel}/T_{\perp})^{1/2}$ .

Using (4.64), (4.71) can be expressed in terms of the electron-ion collision energy  $E_{\text{cm}}$ . The resulting function is shown in figure 4.7. The experimental resonance profile is of asymmetric shape, reflecting the anisotropy of the electron velocity distribution in the centre-of-mass frame of the merged beams. The contributions of the transverse and longitudinal electron temperatures to the overall width of the resonance curve (4.71) can be found by considering the asymptotic behaviours  $T_{\perp} \rightarrow 0$  and  $T_{\parallel} \rightarrow 0$ , respectively. For  $T_{\perp} \rightarrow 0$ , the full width  $\Delta E_{\perp}$  at half maximum (FWHM) of the resonance is defined only by the transverse electron temperature  $T_{\perp}$  [Tok02]:

$$\Delta E_{\perp} = k_B T_{\perp} \ln 2 . \quad (4.72)$$

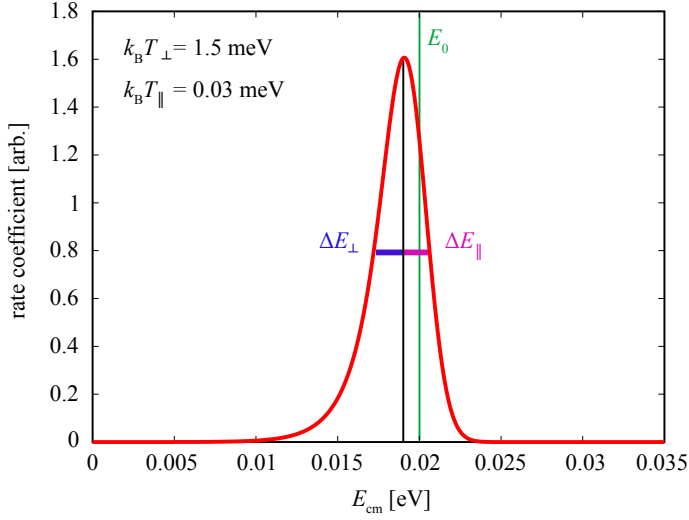


**Figure 4.7:** A singular resonance in the recombination cross section, convolved with an electron energy distribution of longitudinal temperature  $k_B T_{\parallel} = 30 \mu\text{eV}$  and transverse temperature  $k_B T_{\perp} = 1.5 \text{ meV}$ . The resonance energy is  $E_0 = 20 \text{ meV}$ . The low-energetic broadening of the resonance ( $\Delta E_{\perp}$ ) is defined by  $T_{\perp}$ , the high energetic one ( $\Delta E_{\parallel}$ ) by  $T_{\parallel}$ .

For  $T_{\perp} \rightarrow 0$  the linewidth is dominated by  $k_B T_{\parallel}$

$$\Delta E_{\parallel} = \sqrt{16k_B T_{\parallel} E_{\text{cm}} \ln 2}, \quad (4.73)$$

which depends on the centre-of-mass collision energy  $E_{\text{cm}}$ . The total width of the resonance is given by  $\Delta E_{\perp} + \Delta E_{\parallel}$ . As shown in figure 4.8, for decreasing collision energy, the total linewidth improves proportionally to  $\sqrt{E_{\text{cm}}}$  for collision energies significantly larger than  $k_B T_{\perp}$ , but then converges to  $\Delta E_{\perp} = k_B T_{\perp} \ln 2$ . Hence, for low electron-ion collision energies, the experimental resolution of the merged beams setup is limited by the transverse temperature of the Electron Target beam.

### 4.3.3 Dielectronic Recombination of $\text{F}^{6+}$

As shown above, the impact of the longitudinal electron temperature on the energy resolution of the Electron Target dominates at collision energies  $E_{\text{cm}} \gg k_B T_{\perp}$ . In order to be able to observe the effect of both, longitudinal and transverse, electron energy spreads, one needs to look at a resonant recombination process taking place at very low collision energy.

#### Dielectronic Recombination

*Dielectronic recombination* (DR) of lithiumlike  $\text{F}^{6+}$  is a commonly used benchmark system with suitable low-energetic features in its recombination cross-section [Gwi00, Tok02, Spr04, Les07]. Dielectronic recombination is the resonant capture

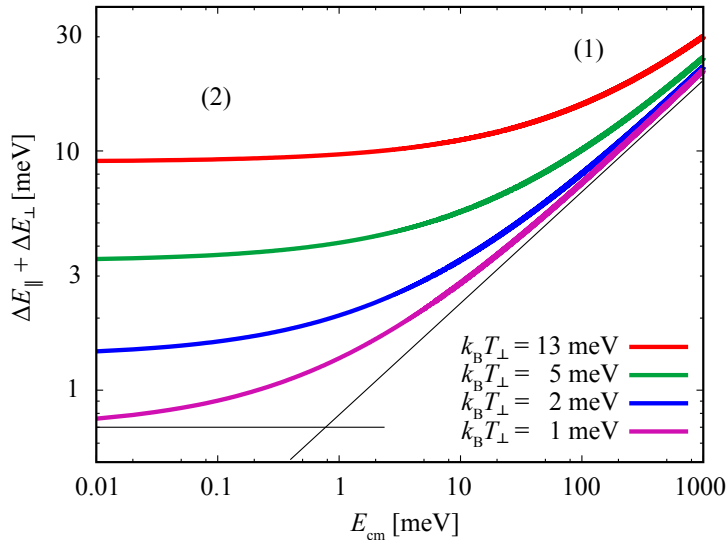
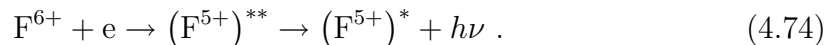


**Figure 4.8:** Full width of a singular resonance in the recombination rate coefficient as a function of electron-ion collision energy  $E_{\text{cm}}$  for different transverse electron temperatures. For  $E_{\text{cm}} \gg k_{\text{B}}T_{\perp}$ , the FWHM behaves  $\sim \sqrt{E_{\text{cm}}}$  (1). As the collision energy vanishes, the linewidth converges towards  $k_{\text{B}}T_{\perp} \ln 2$  (2).

of an electron by the  $\text{F}^{6+}$  ion in an inverse Auger process:



The intermediate state  $(\text{F}^{5+})^{**}$  is formed by excitation of the electronic shell of the lithium-like ionic core from  $1s^22s$  to  $1s^22p$  with simultaneous capture of the initially free electron into a high Rydberg state of the core potential. This doubly excited state is autoionising, and has to stabilise via photon emission in order to conclude the recombination process. The recombination is complete if a state  $(\text{F}^{5+})^*$  has been reached whose energy is lower than the ionisation potential of  $\text{F}^{5+}$ . The intermediate doubly excited state can be formed only if the sum of the Rydberg binding energy  $E_{\text{Ryd}}$  and the kinetic energy of the free electron  $E_{\text{cm}}$  matches the core excitation energy  $E_{\text{core}}$ , i.e. if

$$E_{\text{core}} = E_{\text{Ryd}} + E_{\text{cm}}. \quad (4.75)$$

For  $\text{F}^{6+}$ ,  $2s \rightarrow 2p_j$  core excitation energies  $E_{\text{core}}$  lie around 14 eV [NIS09b], while the binding energy of a Rydberg electron of principal quantum number  $n = 6$  above the ionic core evaluates – in a simple hydrogenic approximation – to  $E_{\text{Ryd}} \approx 13.6$  eV. One thus expects DR resonances at collision energies  $E_{\text{cm}} \approx 0.4$  eV or below. DR of  $\text{F}^{6+}$  has been studied extensively at electron cooler storage rings and is remarkably well understood theoretically. Experiment as well as Relativistic-Many Body Perturbation Theory (RMBPT) calculations of the Rydberg potentials unveiled a complex DR resonance structure at low collision energies, with the lowest auto-ionising states lying at energies as low as 7 meV and 10 meV, respectively [Tok02, Les07].

### $F^{6+}$ as an Electron Temperature Benchmark

In February 2007, a beam of  $F^{6+}$  was stored in the TSR in order to determine the energy resolution of the Photoelectron Target. The beam was produced at a total kinetic energy of 46.4 MeV using the 12-MV Tandem-Van-de-Graaff accelerator of the MPIK.

After the beam was stored in the TSR and cooled by the Electron Cooler, the Electron Target was detuned from the cooling energy  $E_{\text{cool}} \approx 1350$  eV in order to generate low collision energies between stored ions and Target electrons according to (4.64). As we were interested only in DR resonances at collision energies below 0.2 eV, only a small detuning voltage of less than 30 V was necessary. During the detuning of the Electron Target, the energy of the Electron Cooler beam was kept at 1350 eV, so that the effect of ion-dragging by the Target can be neglected.

The current intensity of the photoelectron beam was set to  $I \approx 0.48$  mA. The production rate of  $F^{5+}$  ions by recombination in the Target section was measured by a scintillation detector following the next TSR bending magnet. Details about this detection scheme are given in [Les07]. From the background-subtracted product rate  $R_p$ , the recombination rate coefficient can be calculated using (4.70). A thorough description of the data reduction process in merged beam experiments at the TSR can be found e.g. in [Les07] or in [Les08].

In order to observe the effect of transverse electron temperature, the  $F^{6+}$  recombination rate coefficient was measured using two different magnetic expansion ratios of the Electron Target. The results of these experiments are shown in figure 4.9. According to [Tok02], three resonant states contribute to the DR cross-section in the collision energy range below 70 meV, corresponding to double excitations of the intermediate product  $F^{5+}$  of  $(2p_{3/2} 6p_{1/2})_1$ ,  $(2p_{3/2} 6p_{1/2})_2$ , and  $(2p_{1/2} 6d_{3/2})_2$ . The strengths, energies and natural widths of these states are shown in table 4.3. For the energies and strengths of the second and third resonances we adopt the values published by Lestinsky in [Les07], which we consider the most accurate experimental data on DR of  $F^{6+}$  to date. The lowest resonance at 7 meV has a very large natural width and is practically not visible in the experiment. Its resonance position and strength, just as the widths of all three states, are taken from [Tok02].

The convolution of these three resonances with the anisotropic thermal electron energy distribution as well as a theoretical *radiative recombination* (RR) rate coefficient [Hof00] were used as a fit model to describe the experimental data. The only stable isotope of fluorine is  $^{19}\text{F}$  and carries a nuclear spin of 1/2. Hence, the  $2s_{1/2}$  groundstate of  $F^{6+}$  splits into two hyperfine levels of quantum numbers  $F = \{0, 1\}$ . Multiconfiguration Dirac-Fock (MCDF) calculations published by Boucard predict

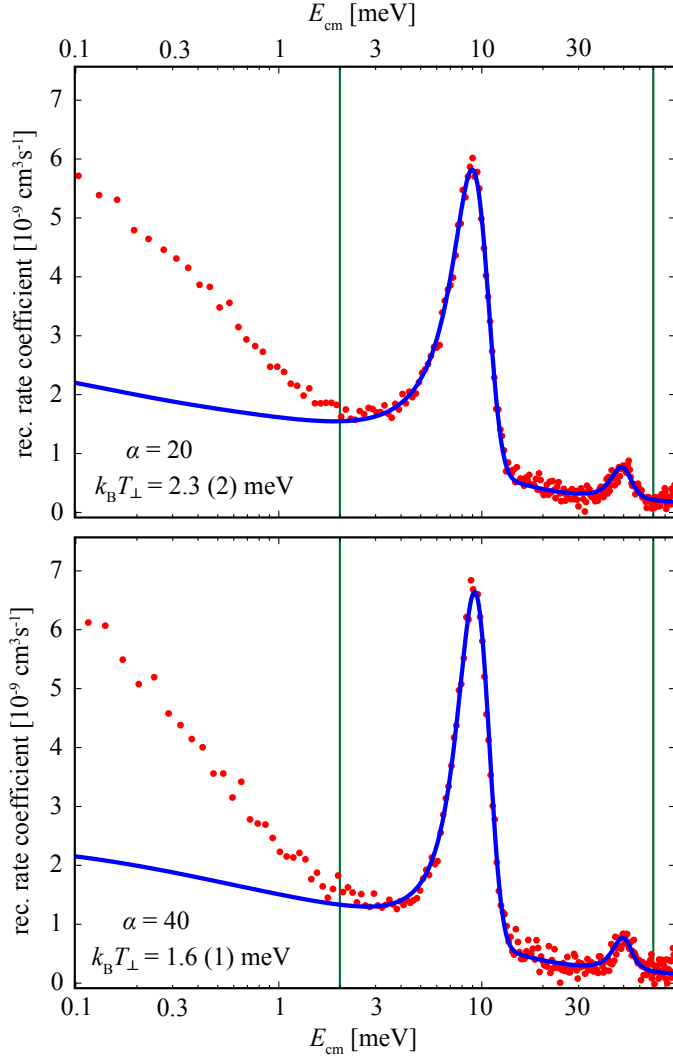


**Figure 4.9:** Recombination rate coefficient of  $F^{6+}$  forming  $F^{5+}$ , measured in February 2007 using the Photoelectron Target. The data (red dots) was fitted with a combination of a theoretical radiative recombination rate coefficient and of the DR resonances given in table 4.3, convolved with the transverse and longitudinal thermal energy spreads of the electron beam (solid blue line). Electron beam expansion factors  $\alpha$  of 20 (top) and 40 (bottom) were applied. The vertical green lines indicate the boundaries of the fit region of interest.

the magnitude of this hyperfine splitting to be  $\Delta E_{\text{HFS}} = 0.366$  meV [Bou00]. The corresponding splitting of the DR resonances from table 4.3 into hyperfine doublets has been taken into account in the fit routine. As  $\Delta E_{\text{HFS}}$  is small compared to the 300 K radiation field experienced by the ions, the hyperfine levels are assumed to be equally populated, such that the relative intensities of the hyperfine components are defined by the statistical weights of the hyperfine levels, which are of  $1/4$  ( $F = 0$ ) and  $3/4$  ( $F = 1$ ), respectively. Due to the small value of  $\Delta E_{\text{HFS}}$  and the large difference in statistical weight of the two components, the additional broadening of the DR resonances caused by hyperfine structure is virtually zero, and its impact on the fit results is vanishing.

The only free parameters in the fit procedure were the longitudinal and transverse electron temperatures,  $T_{\parallel}$  and  $T_{\perp}$ , as well as global scaling and offset constants. For

excited F <sup>5+</sup> state	energy [meV]	width [meV]	strength [10 <sup>-20</sup> cm <sup>2</sup> eV]
(2p <sub>3/2</sub> 6p <sub>1/2</sub> ) <sub>1</sub>	6.9	25.8	415.09
(2p <sub>3/2</sub> 6p <sub>1/2</sub> ) <sub>2</sub>	10.31	0.1	388.9
(2p <sub>1/2</sub> 6d <sub>3/2</sub> ) <sub>2</sub>	52.4	8.7	67.6

**Table 4.3:** Autoionising states of F<sup>5+</sup> of energies below 70 meV. The line positions and strengths of the resonances at 10 meV and 52 meV are experimental values adopted from [Les07]. The remaining parameters result from RMBPT calculations and have been published in [Tok02].

an expansion ratio of  $\alpha = 20$ , corresponding to an electron density in the interaction zone of  $n_e \approx 10^6 \text{ cm}^{-3}$ , the fit yields

$$k_B T_{\perp}^{(\alpha=20)} = (2.3 \pm 0.2) \text{ meV} \quad \text{and} \quad k_B T_{\parallel}^{(\alpha=20)} = (92 \pm 8) \mu\text{eV} \quad (4.76)$$

for the transverse and longitudinal electron energy spreads, respectively. For  $\alpha = 40$ , corresponding to  $n_e \approx 5 \cdot 10^5 \text{ cm}^{-3}$ , we find

$$k_B T_{\perp}^{(\alpha=40)} = (1.6 \pm 0.1) \text{ meV} \quad \text{and} \quad k_B T_{\parallel}^{(\alpha=40)} = (87 \pm 7) \mu\text{eV} . \quad (4.77)$$

These values are surprisingly high. The fitted transverse temperatures are much higher than the values of 0.5 meV and 0.25 meV, respectively, that are expected from (4.15) for a photocathode beam of an initial temperature of  $\approx 100 \text{ K}$ . In addition, the longitudinal energy spread is significantly higher than the value  $k_B T_{\parallel} \approx 43 \mu\text{eV}$  that has been measured for the thermionic cathode of the Electron Target [Les07].

The latter fact can be explained by a process known as *intra-beam scattering*. In order to accelerate the data acquisition rate, both of the above measurements were performed at a relatively high stored ion-current in the TSR of approximately  $47 \mu\text{A}$  in average. At such a high ion density, Coulomb interaction between the particles can heat the ion beam significantly above the longitudinal temperature defined by the Electron Cooler, leading to an additional thermal velocity spread in the recombination process [Ste96].

This hypothesis was tested in a second DR experiment on F<sup>6+</sup> performed in May 2007. The above measurements were repeated – this time all at an expansion factor  $\alpha = 40$  – for a set of 4 different ion current intensities. The corresponding fitted transverse and longitudinal electron temperatures are shown in table 4.4. The data shows a clear correlation between the ion current intensity in the TSR and the apparent value of the longitudinal electron temperature, while the transverse temperature does not change as a function of ion density. As the transverse electron temperature is much higher than the longitudinal one, it hides the small additional broadening caused by the higher velocity spread of the ion beam.

ion current ( $\mu\text{A}$ )	$k_{\text{B}}T_{\perp}$ (meV)	$k_{\text{B}}T_{\parallel}$ ( $\mu\text{eV}$ )
48	1.2 (1)	107 (9)
20	1.3 (1)	69 (6)
9	1.3 (1)	56 (5)
5	1.3 (1)	48 (4)

**Table 4.4:** Apparent values of the transverse and longitudinal electron temperature for different ion current intensities. The fitted value of the longitudinal electron temperature depends strongly on the ion current intensity, indicating intra-beam scattering processes in the stored  $\text{F}^{6+}$  beam at high ion density.

For stored ion currents lower than  $9\ \mu\text{A}$ , the temperature fit routine yields values

$$k_{\text{B}}T_{\perp}^{(\alpha=40)} = (1.3 \pm 0.1)\ \text{meV} \quad \text{and} \quad k_{\text{B}}T_{\parallel}^{(\alpha=40)} = (48 \pm 4)\ \mu\text{eV}. \quad (4.78)$$

This measurement of  $k_{\text{B}}T_{\parallel}^{(\alpha=40)}$  is in agreement with the value of approximately  $43\ \mu\text{eV}$  given in [Les07]. The fitted transverse electron temperature has improved compared to (4.77), indicating slightly better alignment of the Electron Target to the stored ion beam. It is also lower by a factor of approximately 3 compared to the beam temperature for the Electron Target operated with the thermionic cathode published in [Spr04] and [Les07]. Still, it is significantly higher than expected for the photoelectron beam.

The  $\text{F}^{6+}$  recombination rate coefficient and the corresponding fit model are shown in figure 4.10. The depicted data has been measured at an ion current of  $20\ \mu\text{A}$ ,

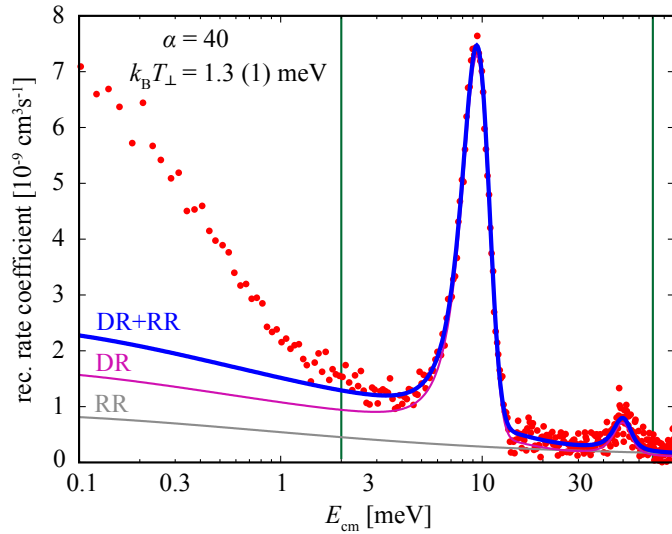


**Figure 4.10:** Recombination rate coefficient of  $\text{F}^{6+}$  forming  $\text{F}^{5+}$ , measured in May 2007 using the Photoelectron Target. The data (red dots) was fitted with a combination of a theoretical radiative recombination (RR) rate coefficient and of the DR resonances given in table 4.3, convolved with the transverse and longitudinal thermal energy spreads of the electron beam (solid blue line). The vertical green lines indicate the boundaries of the fitted region of interest.

at an electron beam expansion ratio  $\alpha = 40$  and at a photoelectron current  $I = 0.48$  mA. The figure also shows the individual contributions of the radiative (RR) and dielectronic (DR) recombination rate coefficients to the overall fit function. As for the earlier measurements, the DR resonance parameters were kept fixed at the values given in table 4.3, and only the electron temperatures were used to fit the data.

## 4.4 Discussion

In this chapter we have discussed the principles of electron cooling and electron-ion recombination. It has been shown that the temperatures of the electron beam in its comoving frame are key parameters in both of these typical applications of a merged-beam setup. Moreover, it has been demonstrated experimentally that a cold electron beam is a *necessity* for electron cooling of slow, molecular ions. Thermionic electron guns, like that implemented in the TSR's Electron Cooler, fail to efficiently cool ion beams of low charge-to-mass ratio. Hence, for electron cooling at the future Cryogenic Storage Ring CSR, targeted mainly at studies of large molecular ions, a photocathode is the electron source of choice [Shor].

It has also been shown that the energy resolution obtained in electron-ion recombination experiments using the Electron Target in operation with the photocathode is significantly higher compared to operation with the thermionic electron gun. Together with the dedicated cooler/target principle, this renders the TSR the highest resolving merged electron-ion beams facility worldwide.

It is known that the energy spread of the electron cloud emitted by the NEA GaAs photocathodes is of approximately (10...15) meV [Orl05]. Given magnetic expansion ratios  $\alpha$  of typically 20 to 40, one thus expects transverse temperatures in the interaction section of (0.25...0.75) meV. In the present experimental analysis, we fail to match these expectations. Both, the analysis of the cooling times of  $\text{CF}^+$ , and that of the dielectronic recombination spectrum of  $\text{F}^{6+}$ , indicate values of the transverse electron temperatures which may be the best available at any Electron Cooler to date, but which are significantly higher than we had hoped for.

While, in the case of  $\text{CF}^+$  cooling, the discrepancy between theory and measurement might be explained by the simplicity of our model of the cooling time, DR of  $\text{F}^{6+}$  is a proven and widely accepted method of determining electron beam temperatures. As has been mentioned earlier, the temperature of the photocathode in operation is not directly measurable, and is therefore not known precisely. The cooling power of the liquid nitrogen circuit or the thermal conductance between the

GaAs cathode and the gun coldhead might be lower than estimated, which could result in an initial electron temperature higher than the expected (100...150) K. However, it is impossible that *all* of the discrepancy between measured and expected transverse temperature arises from a physically too high temperature of the cathode material alone. E.g. the value of  $k_B T_{\perp}^{(\alpha=20)} = (2.3 \pm 0.2) \text{ meV}$  obtained from one of the  $F^{6+}$  measurements mentioned above would imply a temperature of the GaAs crystal of nearly 600 K which can impossibly be true.

One contribution to an apparently higher electron temperatures could be spatial instability of the electron and/or ion beam in the interaction section. As has been discussed earlier in this chapter, an instability of e.g.  $\theta = 0 \pm 5 \cdot 10^{-4}$  in the angle between electron and ion beam would lead to an energy-dependent contribution to the uncertainty of the transverse electron-ion collision energy which is of the same order of magnitude than the expected transverse electron temperature. In the case of the  $F^{6+}$  DR measurement laid out above, the additional transverse energy broadening arising from such an angular instability would be of approximately 0.34 meV according to equation (4.34). Sources of such instabilities might e.g. be spatial variations of the guiding field induction in the interaction section solenoid. The latter has been designed with specification  $\delta B/B < 10^{-4}$  [Spr04]. However, measurement of the induction distribution in the interaction section at this level of accuracy is technically difficult. Hence, fulfilment of this specification has not been verified experimentally up to now. Other potential sources of misalignments might be time-dependent instabilities of the beam optics of the Electron Target or of the TSR which would equally contribute transverse energy spreads according to (4.31).

Such effects leading to *apparently* higher electron temperature become important only in operation of the Electron Target with the photoelectron gun and are difficult to trace, as the setup is used with a different set of operational parameters in almost every experimental run. While their origins are still unclear, it is obvious, that the *magnitudes* of such non-thermal contributions to the energy resolution must be of 1 meV or lower, which means that, in operation of the Electron Target with the thermionic cathode, they remain hidden in the thermal energy spread of the latter. Identification and possibly removal of these new lower limits on the resolving power of the Electron Target setup remains a challenge for the future.



# Chapter 5

## A Robust Pulsed Electron Source for HITRAP

The past chapters were devoted to the use of GaAs photocathodes in the state of Negative Electron Affinity, which allows the production of electron beams of very low temperature. In chapter 2 we have shown that these cathodes may alternatively be used as electron emitters of *positive electron affinity*. Although this mode of operation does not allow thermalisation of electrons in the GaAs bulk, it is characterised by a low but stable quantum efficiency that can be exploited by reflection mode illumination of the photocathode. In this chapter we present a pulsed electron gun based on a PEA GaAs photocathode that has been developed for implementation at the Cooler Penning Trap of the HITRAP project. We show that this source meets the requirements for efficient filling of the Penning Trap with short, intense electron bunches. In contrast to the NEA GaAs photoelectron source of the TSR Electron Target, the pulsed PEA electron gun is designed to operate over periods of several months without requiring cathode maintenance.

### 5.1 The HITRAP Facility

The HITRAP facility is currently in construction at the Helmholtz Centre for Heavy-Ion Research (GSI). HITRAP is designed to decelerate, trap and cool highly charged ions produced in the GSI accelerator facilities. Subsequently it will deliver them to precision trap experiments [Her06]. Highly charged ions, up to bare uranium ( $U^{92+}$ ), will be produced in GSI's UNILAC linear accelerator and SIS-18 synchrotron storage ring. Production of highly charged ions requires high kinetic energies, as electron stripping efficiencies are strongly energy-dependent. E.g. bare uranium is produced

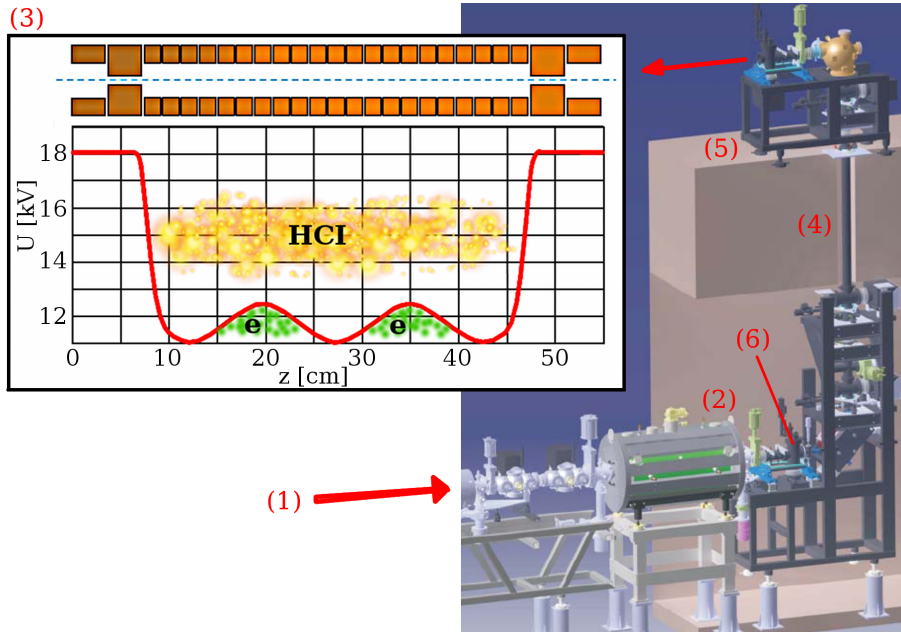


**Figure 5.1:** The HITRAP Cooler Trap setup. Ions from the IH and RFQ decelerator structure (1) are injected into the Penning trap (2) at an energy of 6 keV/u. The latter stores highly charged ions and cooling electrons simultaneously in a nested trap potential (3). After electron and resistive cooling, a cold (4 K) ion bunch is extracted from the Cooler Trap (4) and delivered to precision experiments (5). The electron gun used to fill the Cooler Trap is located in a beam diagnostic chamber (6) on the extraction side of the trap. The picture is partly taken from [Mae08].

at GSI by electron stripping of  $U^{73+}$  in a copper foil at a kinetic ion energy of 400 MeV/u [Dah04].

After production, the ions will be stored and decelerated to a specific kinetic energy of 4 MeV/u in the Experimental Storage Ring (ESR) of GSI. As synchrotron deceleration enlarges the emittance of the ion beam, electron cooling will be applied at several intermediate ion energies. Eventually, bunches of highly charged ions are extracted from the ESR and decelerated further in the HITRAP decelerator complex. The latter consists of an Interdigital H-type linear decelerator (IH) slowing the ion bunch down to an energy of 0.5 MeV/u and of a Radio-Frequency Quadrupole (RFQ) cavity decelerating down to 6 keV/u [Kos09]. At this energy, the ions are caught in a Penning Trap, where they are cooled to a temperature of 4 K before being delivered to subsequent experiments [Mae08].

The Cooler Trap and its extraction line are shown in figure 5.1. The trap is a multi-ring cylindrical Penning Trap, which confines particles radially by a magnetic field of induction 6 T produced by a superconducting solenoid. Axial confinement is ensured by two high-voltage endcap electrodes which lie on a potential of +7 kV with

respect to the trapping volume. The length of the latter will be of approximately 400 mm. In order to facilitate trapping of the ion beam bunch, the base voltage of the trap will be biased at approximately +11 kV with respect to the transfer beam line upon ion injection. This results in deceleration of the ions as they enter the trapping volume and gives the high-voltage supply more time to “close” the trap by lifting the potential of the entrance electrode before the ion bunch reflects at the far endcap [Mae08].

The multi-ring configuration of the Cooler Trap permits to store positively and negatively charged particles simultaneously. As shown in figure 5.1, 21 intermediate ring electrodes can be used to introduce small positive potential hills, so-called “nested traps”, within the main negative trapping well. These positive nested traps will be used to store low-energetic electrons in the Penning Trap prior to ion injection. Such simultaneous trapping of positively and negatively charged particles has already been implemented successfully at antihydrogen experiments at CERN [Amo04, Gab99]. The electrons will then cool the hot ion bunch down to a temperature corresponding to  $k_B T = 10$  eV [Ber04]. In contrast to a storage ring electron cooler, the electron gas in the trap is not continuously renewed. However, the heat transferred from the ionic to the electronic medium is efficiently dissipated by synchrotron emission of the electrons in the intense magnetic field [Mae08]. In order to prevent ion loss by recombination, electrons will be expelled from the Penning trap by reconfiguration of the ring electrode potentials as soon as a thermal ion energy of 10 eV is reached [Mae08]. Resistive cooling will then dissipate the remaining heat of the ion gas until an ion temperature of 4 K is reached [Kos09].

The repetition rate at which HITRAP can deliver cold ion bunches to experiments is limited by the cycling time of the ESR. Presently, synchrotron deceleration and electron cooling of highly charged ions in the storage ring take 17 s to 42 s, depending on the ion species. In order not to further limit the overall duty cycle, the ion cooling processes in the Cooler Trap are specified to take place on much shorter timescales: Electron cooling to 10 eV should be accomplished in approximately 1.5 s and the resistive cooling process is to have a time constant of approximately 3.7 s [Kos09].

## 5.2 The Electron Source

An electron gun based on a PEA GaAs photocathode will be employed to fill the Penning trap with cooler electrons. In contrast to a DC filling procedure [Gor03], the Penning trap will be filled in a so-called “ballistic” way, where all electrons are delivered at once, in a single intense particle bunch short enough to fit into the

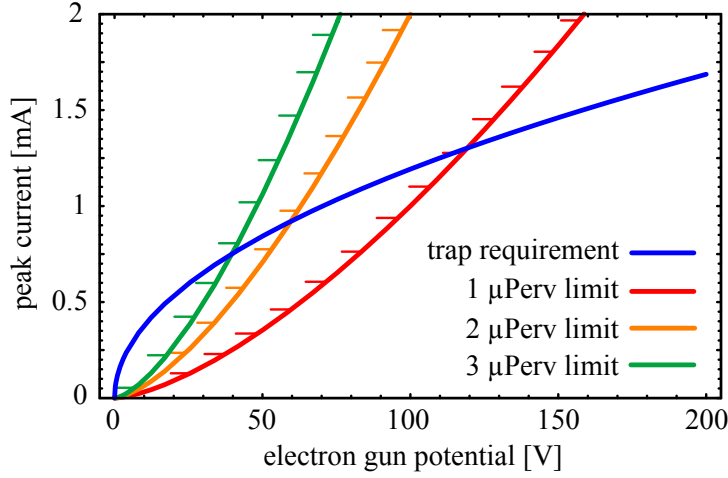


**Figure 5.2:** Electric boundary conditions for operation of the pulsed electron gun at the Cooler Trap. The solid blue line represents the required peak current in the electron pulse according to (5.3) for single-shot ballistic filling of the Penning trap. The red, orange and green curves represent the maximally extractable electron current for values of the gun perveance of 1, 2, and 3  $\mu\text{Perv}$ , respectively.

Penning trap. For a photocathode, bunching is easily achieved by illuminating the cathode with an intense, bunched light source, such as a pulsed laser or a flash lamp. In addition, a photoelectron source has the advantage of being able to operate at room temperature. In contrast to thermionic cathodes, operation of a photocathode therefore does not lead to local deterioration of the vacuum conditions against which the ion transfer line and the Cooler Trap would otherwise have to be protected using a voluminous differential pumping setup. The design of the gun has been elaborated by D. A. Orlov. During this work, a prototype of the electron source has been built and taken into operation in a test setup at the MPIK.

### 5.2.1 Electric Considerations

The design goals of HITRAP include the ability to deliver bunches of up to  $10^5$  bare uranium nuclei. Numerical simulations of the electron cooling process performed by Maero have shown that  $10^9$  electrons are necessary to cool such an intense ion bunch within the specified time [Mae08]. The trap is to be filled with electrons in a single shot, i.e. all  $10^9$  particles have to be emitted in one pulse short enough to fit inside the Penning trap. Hence, the maximum duration  $\Delta t_{\text{fill}}$  of the trap filling procedure is related to the electron velocity  $v_e$  in the trapping volume:

$$\Delta t_{\text{fill}} = \frac{2l}{v_e}, \quad (5.1)$$

where  $l$  is the length of the trap potential. After the time  $\Delta t_{\text{fill}}$ , electrons reflected at the far endcap electrode have reached the trap entrance again. In order to store the electron bunch, the entrance electrode has to be lifted to negative potential at this moment, making further electron injection impossible. If the base potential of the

Cooler Trap is grounded during electron filling,  $v_e$  is given by the cathode potential  $U$  of the electron gun, thus

$$\Delta t_{\text{fill}} = 2l \left( \frac{2eU}{m} \right)^{-1/2} . \quad (5.2)$$

E.g. for a cathode potential  $U = 50$  V, the maximum filling time amounts to  $\Delta t_{\text{fill}} \approx 190$  ns. If  $N_e$  electrons are to be delivered within this time, the peak current in the pulse is approximately given by

$$I_{\text{peak}} = \frac{N_e e}{\Delta t_{\text{fill}}} = \frac{N_e e}{2l} \left( \frac{2eU}{m} \right)^{1/2} . \quad (5.3)$$

Hence, we see that trap filling at higher electron gun voltage also requires higher emission currents of the photocathode. As discussed in chapter 2, PEA GaAs photocathodes can be expected to have quantum efficiencies of only (0.1...1) % in the ultraviolet spectral region. Therefore, emission of high peak electron currents would require high UV light intensity to be delivered to the cathode. While, from this point of view, it is advantageous to operate the electron gun at low cathode voltage, we recall from equation (3.1) that the maximum peak current that can be extracted from the electron gun is limited by its perveance  $P$  to

$$I_{\text{max}} = P U^{3/2} . \quad (5.4)$$

Hence the ability to operate the pulsed electron gun at low cathode voltage  $U$  – and thus at low peak emission current according to (5.3) – requires a high perveance.

Figure 5.2 illustrates the electric boundary conditions for efficient Cooler Trap filling using a pulsed photoelectron gun. The blue line represents, according to (5.3), the peak electron current, as a function of the cathode potential, necessary for the delivery of  $N_e = 10^9$  electrons into the trap volume of length  $l = 0.4$  m [Kos09]. The other curves show the perveance limits of the electron current as a function of the extraction voltage for gun perveances of 1, 2 and 3  $\mu\text{Perv}$ . At given perveance, the area above the corresponding curve is excluded by (3.1).

### 5.2.2 Electron Gun Design

Figure 5.3 shows how the pulsed electron gun will be implemented at the Cooler Trap according to the design by D. A. Orlov. The gun will be mounted in the ion beam diagnostic chamber at the exit of the Cooler Trap. As its position must not interfere with the trajectories of ions extracted from the trap, it is mounted off-axis of the extraction beam line, at an angle of  $35^\circ$  with respect to the axis of the Cooler

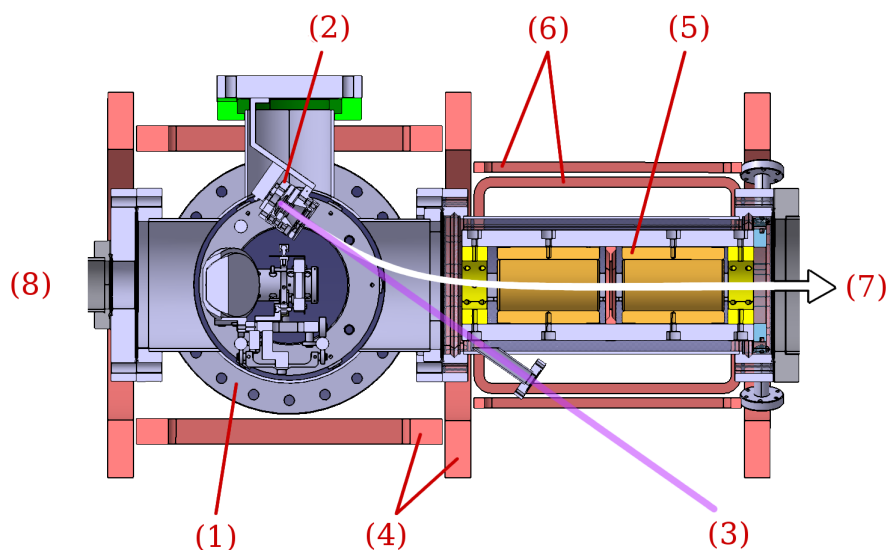


**Figure 5.3:** The beam diagnostic chamber (1) following the Cooler Trap. The electron gun (2) is irradiated by a pulsed UV light source (3). An arrangement of magnetic coils (4) surrounding the diagnostic box steers the electron beam into a solenoid section (5) guiding it into the Cooler Trap. Further correction coils surrounding the solenoid allow to steer the electron beam into the aperture of the trap endcap electrode (7). The electron gun is mounted off-axis, in order not to block the ion beam extraction line (8).

Trap. Electron emission is induced by a pulsed light beam shone onto the photocathode surface through a vacuum viewport in the opposing chamber wall. Using a saddle-coil arrangement of magnetic coils surrounding the diagnostic chamber, the electron bunches are steered into the direction of the Cooler Trap. A transfer section surrounded by a solenoid coil generating a field induction of (100...200) G then guides the electrons towards the Penning trap entrance. Correction coils surrounding the solenoid section permit to align the electron beam to the trap electrode aperture.

The electron gun has to be of very compact design in order to fit into the restrained volume of the beam diagnostic chamber. As can be seen in the left drawing in figure 5.4, the entire device fits onto a CF-63 vacuum blind flange. It employs a GaAs photocathode operated in PEA mode as discussed in chapter 2. The GaAs sample is of the same type than that used in the TSR Electron Target (c.f. figure 2.2). PEA operation requires the cathode to be illuminated in reflection mode using ultraviolet excitation light of 4.4 eV photon energy or more. Assuming a quantum efficiency of the PEA photocathode of 0.1%, a UV photon pulse of a total energy of approximately  $1 \mu\text{J}$  is necessary in order to emit the required amount of  $10^9$  electrons. This energy is easily achievable by standard 262-nm pulsed laser devices. Initial test have revealed that the excitation light can alternatively be deliv-

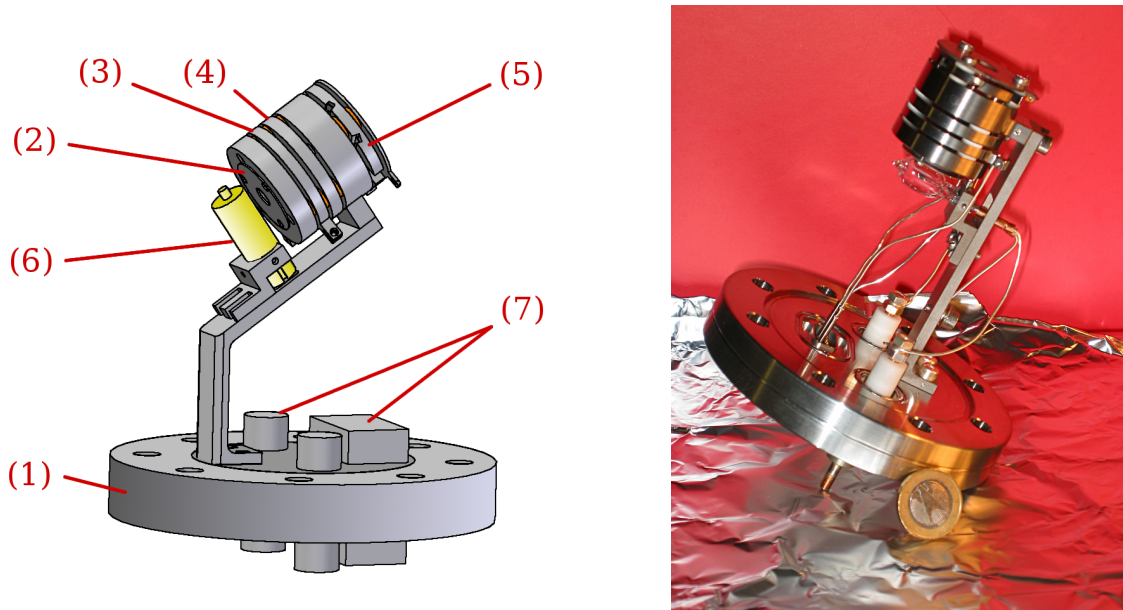


**Figure 5.4:** *Left:* Drawing of the pulsed electron gun designed for operation at the Cooler Trap. The entire gun fits on a single CF-63 blind vacuum flange (1). The PEA GaAs photocathode is statically fixed to the main gun electrode (2). The latter is followed by a pierce shield (3) and an extraction electrode (4) which can be independently biased. Cesium dispensers (5) allow *in-situ* activation of the GaAs surface. A halogen lamp (6) can be used to clean the cathode surface by radiative heating. The flange features electric feedthroughs (7) for the gun electrode potentials as well as for the lamp and Cs dispenser power supplies. *Right:* Photograph of the gun prototype tested at MPIK. Unlike the final design, the prototype does not have to be mounted off-axis in the test vacuum chamber, it is therefore not inclined with respect to the plane of the vacuum flange.

ered by a xenon flash lamp (*Hamamatsu L9455*). The latter device is considerably cheaper than a laser source, while still emitting a few  $\mu\text{J}$  of ultraviolet light per pulse according to the manufacturer.

The GaAs photocathode is statically fixed to the main gun electrode, i.e. no in-vacuum replacement of the photocathode is foreseen. The design goal is to operate the electron source practically maintenance-free for several months. As visible in figure 5.4, the electron gun features a cesium dispenser (*SAES Getters Cs<sub>2</sub>CrO<sub>4</sub>*) which allows *in-situ* activation of the GaAs surface to the state of reduced positive electron affinity discussed in chapter 2. A halogen lamp is mounted next to the rear side of the electron gun and allows to clean the GaAs surface by radiative heating, similar to the heat-cleaning facility implemented in the preparation chamber of the TSR photocathode setup.

The electron gun is of Pierce geometry. The photocathode sample is embedded into the main gun electrode which can be lifted to negative potentials of a few hundred volts. The pierce shield and the extraction ring electrode are fixed between

the cathode and the grounded gun support using ceramic spacers. All electrodes can be biased independently. The CF-63 flange, on which the electron gun is mounted, is equipped with low-voltage electric feedthroughs supplying the electrode potentials, as well as with two high-current feedthroughs connected to the halogen lamp and to the Cs dispenser, respectively.

A prototype of the pulsed electron gun has been built and tested at MPIK. It is visible in the photograph on the right side of figure 5.4. In contrast to the final design that will be implemented at HITRAP, the prototype does not need to be fixed at an angle with respect to the test vacuum chamber. Thus, its support is not inclined with respect to the plane of the vacuum flange. Otherwise the two electron guns are identical.

### 5.3 Tests of the Electron Gun Prototype

The electron gun prototype has been taken into operation in a test vacuum setup at MPIK, which simulates the future operating conditions in the HITRAP diagnostic chamber. Coils surrounding the vacuum chamber immerse the electron gun in an axial magnetic guiding field of (0.01...0.02) T. An ion getter pump (*Varian StarCell*) and NEG strips (*SAES Getters*) lower the residual gas pressure to approximately  $2.5 \cdot 10^{-10}$  mbar. A UV-grade viewport (*Caburn-MDC VP-100S*) allows to irradiate the GaAs photocathode in reflection mode. Correction coils can be used to create a weak (0...10 G) magnetic steering field transverse to the main guiding field and allow to direct the electron beam onto a Faraday cup.

Before being mounted into the electron gun, the GaAs photocathode underwent the standard surface cleaning procedure by etching in HCl solution which has been described in chapter 2. In contrast to operation at the TSR Electron Target, the cleaned cathode was not protected by a pure nitrogen atmosphere upon transfer to the vacuum setup. After pumping and bakeout of the test chamber, the photocathode has been annealed using the radiative oven included in the electron gun.

#### 5.3.1 Spectral Response

The spectral response of the photocathode has been measured using the experimental setup also used for emission spectroscopy of cathodes in the TSR preparation chamber. After alignment of the electron beam onto the Faraday cup, the current through the latter was measured as a function of the irradiated photon energy. The very low emission current (typically lower than 1 pA) was measured using a lock-in

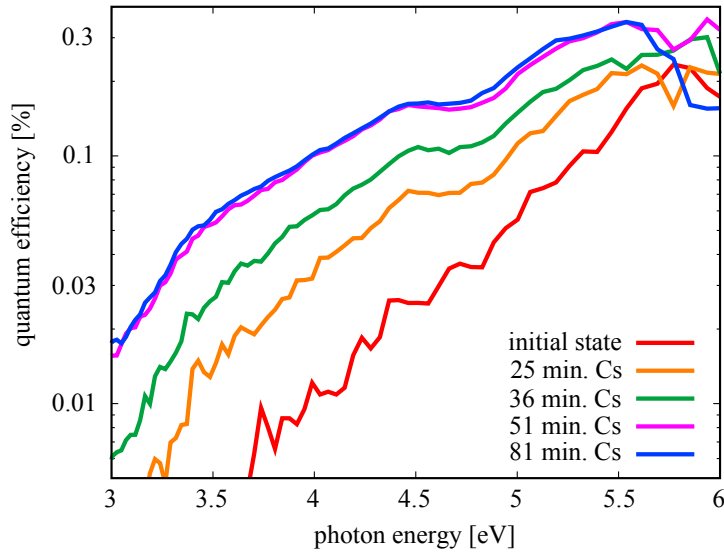


**Figure 5.5:** Spectral response of the PEA photocathode upon activation using the built-in Cs-dispensers of the electron gun.

amplifier. Details about this measurement scheme have been given in chapter 3.

Figure 5.5 shows the spectral evolution of the photocathode upon activation with the cesium dispenser of the electron gun. The dispenser was operated at a current of 4.8 A, and the spectral response of the GaAs surface was measured at different times during the Cs exposure. The red curve corresponds to the response of the initially bare GaAs surface. One sees that the quantum efficiency of the cathode decreases exponentially at photon energies below 5.5 eV. Cesium exposure lowers the electron emission threshold energy and a quantum efficiency enhancement at energies above 4.4 eV becomes apparent (orange and green curves). As discussed in chapter 2, this is characteristic for a PEA GaAs photocathode. After approximately 50 minutes of Cs activation (magenta curve), the quantum efficiency reaches a saturation level. Further exposure (blue curve) does not change the spectral response of the cathode anymore. The final quantum efficiency in the photon energy range between 4.4 eV and 5.0 eV lies between 0.1 % and 0.2 %.

For maintenance-free long-time operation at the HITRAP Cooler Trap, the quantum efficiency of the photocathode should be stable over long periods of time. As the Cooler Trap has to be filled with electrons only once per ESR synchrotron cycle, a single electron pulse will be extracted from the gun every (17...42) s only. Hence, the *average* electron current is very low and we expect the lifetime of the photocathode to be limited mainly by current-independent reaction of the Cs-layer with residual gas molecules.

The robustness of the activation layer with respect to residual gas degradation has been tested by artificial deterioration of the vacuum conditions in the test

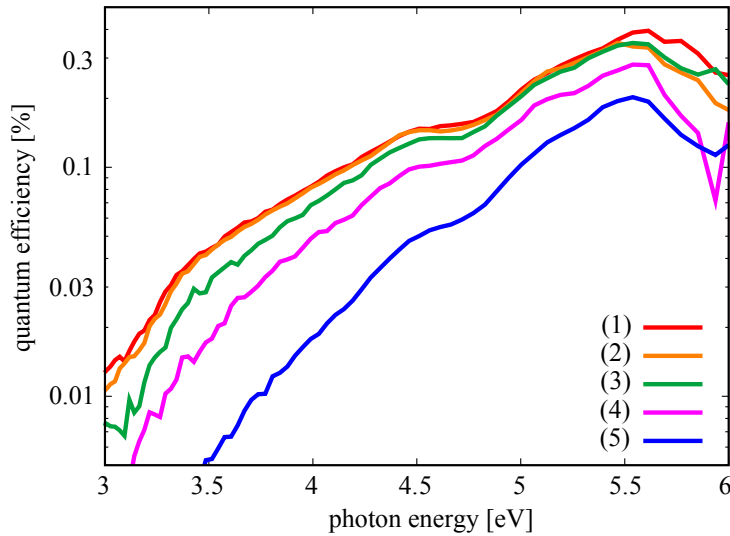


**Figure 5.6:** Spectral response of the PEA photocathode upon various degradations of the vacuum conditions in the gun test chamber. Shown are the spectral responses after three days under optimal UHV conditions (1), after switching off the ion-getter pump for 19 hours (2), after 24 hours of NEG activation (3), and after opening the turbomolecular pump valve for 1.5 h (4) and 24 hours (5), respectively.

chamber. The evolution of the photocathode response during these tests is shown in figure 5.6. The red curve (1) shows the quantum efficiency of the photocathode three days after activation in ultra high vacuum of  $2.5 \cdot 10^{-10}$  mbar. In order to allow the residual gas pressure to rise, the ion-getter pump was temporarily disabled. Under these conditions the pressure rose quickly to a value of approximately  $2 \cdot 10^{-8}$  mbar which was sustained for 19 hours. Assuming the pumping speed of the ion pump to be the same for all relevant chemical agents, this simulates a cathode age of approximately 1500 hours at the original UHV conditions. The orange curve (2), representing the spectral response of the (Cs)GaAs surface after this accelerated aging, is practically identical to (1). In order to deteriorate the vacuum conditions even further, a NEG module was activated. This process, normally done only during chamber bakeout, lead to a quick rise of the residual gas pressure by another three orders of magnitude to a value of approximately  $10^{-5}$  mbar, which lasted for 24 h. As shown by the green curve (3) in figure 5.6, this rough treatment caused a slight decrease of the quantum efficiency of the photocathode in the energy range between 4.4 eV and 5.0 eV. However, the quantum efficiency remained well above the 0.1% mark. Finally, the valve to the turbomolecular pump was opened. The pipe leading to the latter was not baked, opening of the valve thus contaminated the vacuum setup with a high partial pressure of  $\text{H}_2\text{O}$ , estimated to approximately  $10^{-8}$  mbar. Water is known to be very harmful to the Cs layers of GaAs photocathodes [Wad90]. Correspondingly, the measured electron emission current quickly decreased. 1.5 hours after opening the turbomolecular pump valve, the UV quantum efficiency had decreased to below 0.1% (magenta curve, 3), and after 24 hours, the cathode had degraded almost to the state before Cs activation (blue curve, 5).

Under normal circumstances, the presence of significant amounts of  $\text{H}_2\text{O}$  can be excluded in a UHV setup. These measurements thus indicate very good long-time

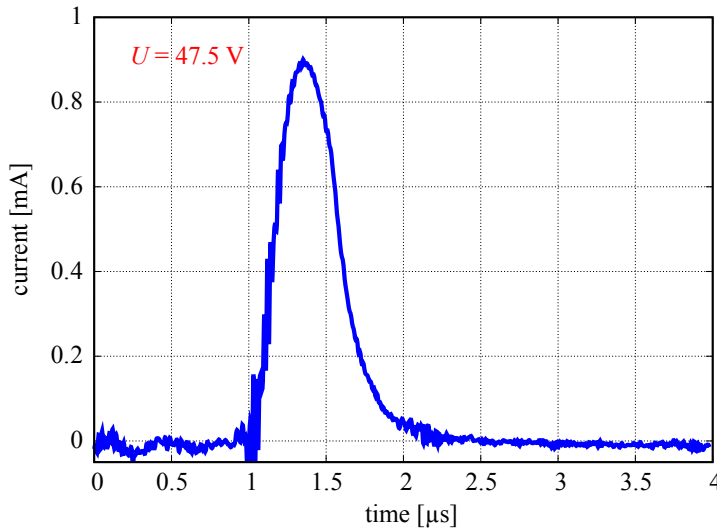


**Figure 5.7:** Electron pulse extracted from the prototype gun irradiated by the flash lamp at an extraction voltage of 47.5 V.

stability of the PEA quantum efficiency of the pulsed electron gun under realistic vacuum conditions in the  $10^{-10}$  mbar range as well as high robustness against possible short-term vacuum degradations. Considering that Cs activation in the pulsed gun is performed without supporting oxygen exposure of the GaAs surface, the stable value of the PEA quantum efficiency of (0.1... 0.2) % is in reasonable agreement with the earlier findings at the TSR photocathode setup reported in chapter 2. In particular, it confirms that the ultraviolet quantum efficiency of the PEA GaAs photocathode is higher by at least one order of magnitude compared to that metal photocathodes [Dow09].

### 5.3.2 Pulsed Operation

Operation of the electron gun in pulsed mode has been tested by irradiating the photocathode using a xenon flash lamp (*Hamamatsu L9455*) of high UV intensity. The corresponding electric current pulses emitted by the electron gun have been measured by discharging the Faraday cup through resistors of  $510\ \Omega$  or  $52.5\ \Omega$ . The resulting time-dependent potential difference over the resistor was measured using a digital oscilloscope (*Tektronix TDS-380*). Since the repetition rate of the pulsed electron gun is low, each voltage pulse could be recorded using a computer system communicating with the oscilloscope via its RS-232 serial interface. At known resistance, the measured voltage pulse can be used to calculate the time-dependent current intensity. Time integration over the signal yields the total electric charge contained in the pulse.

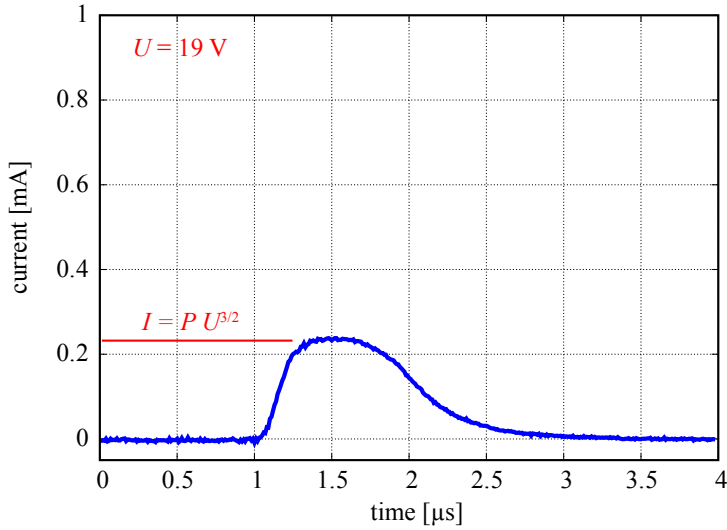


**Figure 5.8:** Electron pulse extracted from the prototype gun irradiated by the flash lamp at an extraction voltage of 19 V.

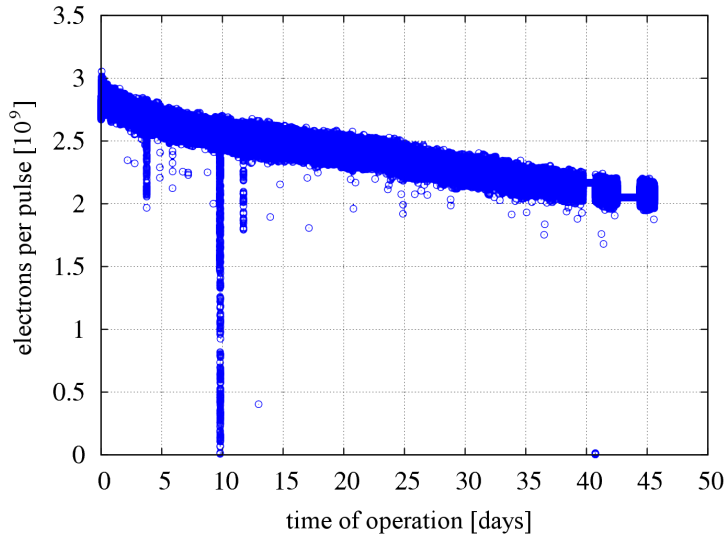
### Pulse Shape and Gun Perveance

Figure 5.7 shows the shape of a typical electron bunch emitted by the electron gun. The full width at half maximum of the measured current pulse is approximately 430 ns, in reasonable agreement with the length of the light pulse of approximately 400 ns as stated by the manufacturer of the flash lamp. For the electron gun voltage of 47.5 V, which was applied during this measurement, the maximum filling time of the HITRAP Cooler Trap amounts to approximately 200 ns according to (5.2), i.e. the electron bunch emitted by irradiation with the flash lamp is too long by approximately a factor of 2. However, integration of the current signal yields a number of electrons of

$$N_e = (2.8 \pm 0.2) \cdot 10^9 \quad (5.5)$$

contained in the pulse. Hence, in combination with the flash lamp, the pulsed electron gun delivers more electrons per bunch than the  $10^9$  which are required for operation of the Cooler Trap. Thus, even trapping of only a part of the bunch length is likely to be sufficient to fill the trap with the required number of electrons. Alternatively, illumination of the photocathode with a pulsed 262-nm laser is possible, which will yield much shorter bunch lengths as well as even larger numbers of electrons due to the higher intensity of the laser pulses.

The perveance of the electron gun can be determined by gradually reducing the extraction voltage of the electron gun. At the point where the extracted current becomes limited by perveance, saturation effects cause a change in the shape of the current pulse recorded at the Faraday cup. This effect is clearly visible in figure 5.8. At a gun voltage reduced to 19 V, the extracted current saturates at approximately 0.23 mA, whereas at an extraction potential of 47.5 V, approximately 0.9 mA are



**Figure 5.9:** Long time test of the prototype pulsed electron gun. For approximately 1.5 months, an electron bunch was extracted from the gun every 8 seconds by irradiation with the xenon flash lamp.

extracted from the gun with no sign of current saturation. Using this method, the perveance of the pulsed electron gun has been determined to

$$P = (3.0 \pm 0.2) \mu\text{Perv} . \quad (5.6)$$

This high perveance ensures high flexibility in operation of the pulsed electron source. As can be seen from figure 5.2, it allows to operate the electron gun at voltages as low as 40 V and at peak electron currents well below 1 mA.

### Operational Tests

In order to test the reliability of the pulsed electron source over long periods of operation, a long-time test was performed, during which a bunch of electrons was extracted from the cathode every 8 seconds for approximately 1.5 months. This emission rate is at least twice as high as will be required in operation at HITRAP. Nevertheless, the pulsed intensity proved very stable over this time. As can be seen in figure 5.9, the average number of electrons per bunch dropped from initially  $2.8 \cdot 10^9$  to approximately  $2.1 \cdot 10^9$  in 45 days of continuous operation. This suggests a usable lifetime of several months before the cathode has to be reactivated.

Preliminary tests have shown that reactivation of the degraded cathode can be performed *in operation*, by simple Cs exposure of the degraded photocathode surface. In a test measurement shown in figure 5.10, the partially degraded cathode was exposed to the cesium dispensers for approximately 4 hours without prior cleaning of the GaAs surface by radiative heating. The number of electrons extracted per pulse rose from approximately  $2.7 \cdot 10^9$  to  $2.9 \cdot 10^9$ . Although more careful analysis

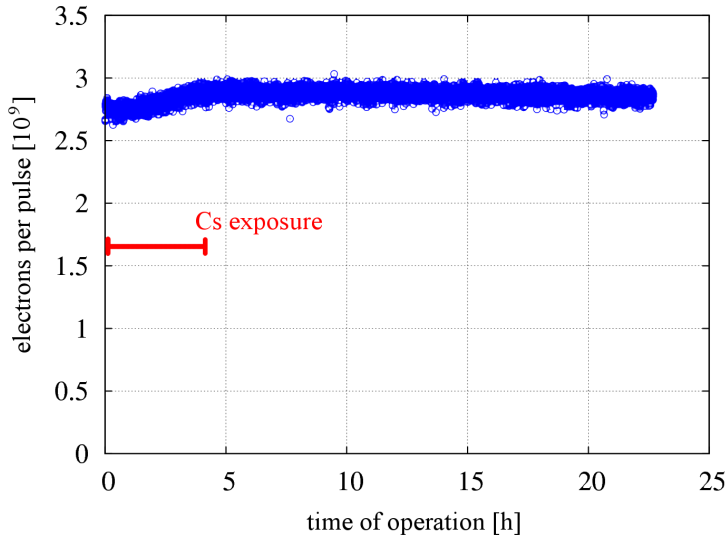


**Figure 5.10:** In-operation Cs reactivation of the PEA photocathode. The red line indicates the period during which the PEA photocathode was exposed to Cs flux from the dispensers.

has to reveal how often this simple re-cesiation can be applied successfully, it is an interesting option for cathode activation, since, in contrast to the radiative oven, the vacuum distortion caused by operation of the cesium dispensers is minimal. Thus, in operation at the Cooler Trap, this simple reactivation procedure could possibly be applied without compromising the operation of the HITRAP transfer line.

## 5.4 Outlook

The test measurements performed with the prototype PEA photoelectron gun promise successful operation as a pulsed electron source at the Cooler Trap of HITRAP. Following the experience at the test setup, no significant changes seem necessary to the original design of the electron source. The latter will thus be implemented at HITRAP, as soon as the commissioning of the Cooler Trap starts.

It is projected to operate the pulsed electron gun by illumination with the same xenon flash lamp that was used in the test measurements described in this chapter. As has been discussed, the pulse length of approximately 400 ns defined by the time constant of the flash discharge is longer than the trap filling time as given by (5.2). A straight forward approach would be to store only the intense central part of the electron pulse, or to generate shorter, more intense bunches using a pulsed 262 nm Laser beam. Another possibility would be deceleration of the electron bunch below the energy emitted by the gun, increasing the filling time given by (5.2). To a certain degree, the latter effect occurs automatically: At the moment of entering the high magnetic field of the Penning trap, the electron beam is magnetically compressed

by a factor of  $\alpha \approx 1/300$ . As a consequence, the space charge potential of the electron beam rises strongly, slowing the particles accordingly. However, the same effect could also lead to unwanted *reflection* of a part of the electron bunch at its own space charge potential if the initial velocity of the bunch is too low.

In presence of an intense trap field, the optimal electron bunch length might thus differ from the naive calculation according to (5.2) and longer pulses, of lower initial density and space charge, might even be beneficial. At this point, we conclude that the present design, as has been tested in this work, allows for a good flexibility in the search for an optimal trap filling procedure. However, the latter can only be elaborated once the pulsed electron source has been installed at the Cooler Trap.



# Chapter 6

## Summary

A cold electron gun based on NEA GaAs(Cs,O) photocathodes has been introduced as a reliable tool in atomic and molecular collision experiments. It has been used at the Electron Target of the Test Storage Ring (TSR) at the Max-Planck-Institute for Nuclear Physics over a long period of operation, in which the GaAs photocathode has replaced its thermionic counterpart in 2006 and has been used in a total of 25 merged electron-ion beam experiments performed at the TSR since.

We have shown that, during this work, the reliability and performance of the GaAs photoelectron gun has been significantly enhanced. The maximum current that can be extracted from the electron gun, while maintaining acceptable lifetimes of the (Cs,O) activation layers of the photocathodes, has been increased from approximately 0.2 mA to more than 1 mA. Now, useful cathode operation times of approximately 24 h can be expected at this current. At lower extraction currents, cathode lifetimes of 90 h have been measured. This improvement in cathode reliability has been achieved by identification and minimisation of the main mechanisms leading to degradation of the (Cs,O) activation layers. Apart from current-induced deterioration of the vacuum conditions next to the electron gun, we have identified that bombardment of the cathode surface by residual gas particles ionised in the Electron Target beam plays a significant role in degradation of the cathode quantum efficiency. Except for ionisation events taking place directly in the acceleration region of the electron gun, ion backstreaming to the photocathode can be efficiently prevented by a low-voltage screening electrode.

A sensitive electron emission spectroscopy setup has been implemented, which allows to measure the spectral response of photocathodes in a wide band of wavelengths, from the infrared to the near ultraviolet (200 nm). Spectral response measurements provide in-vacuum diagnostics of the state of the GaAs surface and have

been applied to optimise the atomic hydrogen cleaning procedure implemented by Weigel [Wei04].

The hydrogen radical source has been calibrated using data published for a similar setup [Tsch00, Tsch08]. While previous studies [Mar03, Bay05] found a steady decrease of the maximum achievable quantum efficiency of the photocathode as a function of the integrated atomic hydrogen exposure, we did not observe this effect. We explain this by the fact that our setup is based on a low-energetic, thermal hydrogen cracker, while the previous experiments employed radiofrequency plasma hydrogen sources. We presume that the relatively high-energetic atoms produced by these latter sources damage the GaAs photocathodes by introduction of crystal defects that lower the photoelectron escape probability. In our analysis, we do observe a slow, irreversible decrease of the quantum efficiency of cathodes grown by metal-organic chemical vapour deposition (MOCVD), in contrast to GaAs samples grown by liquid-phase epitaxy (LPE) which do not suffer from this effect. Analysis by coworkers at the Institute of Semiconductor Physics in Novosibirsk has demonstrated that this degradation process is not related to atomic hydrogen exposure, but caused by development of lattice dislocations within the photocathode heterostructure. Probably this arises from the repeated mechanical stress to which the cathodes are subjected upon thermal cleaning. Although a detailed explanation of this behaviour cannot be given yet, it is an interesting finding that MOCVD crystals seem more vulnerable to development of lattice dislocations than their LPE-grown counterparts, although MOCVD permits to grow semiconductors of better thickness homogeneity and sharper layer interfaces.

The advantages of the cold electron beams emitted from NEA GaAs photocathodes become apparent especially at low beam energies. Slow electron beams will be a requirement for operation of the Cryogenic Storage Ring (CSR) presently under construction at the MPIK, where electron cooling of heavy molecular ions will be applied at energies down to one electronvolt. In TSR experiments on slow beams of  $\text{CF}^+$  ions, the superior transverse cooling force of the photoelectron beam compared to the TSR Electron Cooler, which employs a thermionic cathode, has been demonstrated. At a cooling energy of only 46 eV, the Photoelectron Target was able to cool the heavy molecular beam within a few seconds, reaching final beam diameters of well below 1 mm. Despite the low charge-to-mass ratio of  $\text{CF}^+$  of  $Z/M = 1/31$ , and despite the perveance-limited electron density, cooling times of 1.5 s or below have been measured. In contrast, the cooling time achieved by the Electron Cooler was of more than 20 s, much longer than the ion lifetime in the storage ring, and thus not suitable to prepare the  $\text{CF}^+$  beam into an experimentally useful equilibrium state. For the future CSR, photocathodes are thus the only viable option for generation of the cooler electron beam.

As benchmarks for the resolving power of the Photoelectron Target in electron-ion collision experiments, we have performed dielectronic recombination measurements on  $F^{6+}$ . At a magnetic expansion ratio of  $\alpha = 40$  and a beam energy of 1350 eV, a transverse energy spread of the photoelectron beam of  $k_B T_{\perp} = 1.3(1)$  meV has been measured. While this value is very good for an electron cooler, it is significantly higher than the value of approximately 0.3 meV that one naively expects for a photocathode cooled to (100...150) K. As possible reasons for this discrepancy we have considered instabilities in the alignment of electron and ion beams in the Electron Target's interaction section as have been discussed in the final section of chapter 3. The low transverse temperature of the photoelectron beam ensures very good energy resolution of the Electron Target in the region of low velocity detuning, where the sensitivity of the merged-beams technique is highest.

Besides their ability to emit very cold electron beams when prepared to the state of negative electron affinity, photocathodes have the advantageous feature that no heating of the emitter material is required. This makes them optimal electron sources for vacuum-critical applications. Spectral response measurements performed at the photocathode setup of the TSR provided evidence that *degraded* GaAs(Cs,O) photocathodes feature a low, but very stable residual quantum efficiency in the ultraviolet range between 4.4 eV and 5.0 eV photon energy. This residual quantum efficiency is explained by formation of a stable state of reduced Positive Electron Affinity (PEA) at the cathode surface. Although much lower than that of NEA cathodes as used in the Electron Target, the ultraviolet quantum efficiency of these PEA photocathodes has been measured to be at least an order of magnitude higher than for metal cathodes.

Based on this principle, an ultraviolet-driven, pulsed PEA photoelectron source prototype for the HITRAP Cooler Trap has been built and taken into operation. It has been demonstrated that this electron gun satisfies the requirements for efficient filling of the Cooler Penning Trap with single electron bunches. The stability of the bunch intensity has been measured over a period of 1.5 months. The measurement indicates that several months of practically unattended operation of this electron source can be anticipated, as required by the design goal. The quantum efficiency of the statically mounted PEA GaAs photocathode of the electron gun prototype has been shown to be very stable at a value greater than 0.1 % for a photon wavelength of 262 nm. This confirms the earlier findings from the TSR setup and allows to operate the pulsed electron gun even at relatively low excitation light intensity.



# Bibliography

- [All95] R. Alley, H. Aoyagi, J. Clendenin, J. Frisch, C. Garden, E. Hoyt, R. Kirby, L. Klaisner, A. Kulikov, R. Miller, G. Mulhollan, C. Prescott, P. Sgez, D. Schultz, H. Tang, J. Turner, K. Witte, M. Woods, A. D. Yeremian, M. Zolotarev, *The Stanford linear accelerator polarized electron source*, Nucl. Instr. Methods Phys. Res., Sect. A **365** (1995), 1
- [Alp95] V. L. Alperovich, A. G. Paulich, H. E. Scheibler, A. S. Terekhov *Evolution of Electronic Properties at the p-GaAs(Cs,O) Surface during Negative Electron Affinity State Formation*, Appl. Phys. Lett. **66** (1995), 2122
- [Amo04] M. Amoretti *et al.*, *The ATHENA antihydrogen apparatus*, Nucl. Instrum. Methods Phys. Res., Sect. A **518** (2004), 679
- [Bar07] R. Barday, *Untersuchungen zur Lebensdauer von NEA-Photokathoden bei der Extraktion sehr hoher mittlerer Ströme*, dissertation, University of Mainz (2007)
- [Bay05] M. Baylac, P. Adderley, J. Brittan, J. Clark, T. Day, J. Grames, J. Hansknecht, M. Poelker, M. Stutzman, A. T. Wu, A. S. Terekhov, *Effects of Atomic Hydrogen and Deuterium Exposure on High Polarization GaAs Photocathodes*, Phys. Rev. ST AB **8** (2005), 123501
- [Bel06] P. M. Bellan, *Fundamentals of Plasma Physics*, Cambridge University Press (2006)
- [Ber04] J. Bernard, J. Alonso, T. Beier, M. Block, S. Djekić, H.-J. Kluge, C. Kozhuharov, W. Quint, S. Stahl, T. Valenzuela, J. Verdú, M. Vogel, G. Werth, *Electron and positron cooling of highly charged ions in a cooler Penning Trap*, Nucl. Instr. Methods Phys. Res., Sect. A **532** (2004), 224
- [Beu00] M. Beutelspacher, *Systematische Untersuchungen zur Elektronenkühlung am Heidelberger Schwerionenspeicherring TSR*, dissertation, University of Heidelberg (2000)

- [Bis93] U. Bischler, E. Bertel, *Simple Source of Atomic Hydrogen for Ultrahigh Vacuum Applications*, J. Vac. Sci. Technol. **11** (1993), 458
- [Bou00] S. Boucard, P. Indelicato, *Relativistic many-body and QED effects on the hyperfine structure of lithium-like ions*, Eur. Phys. J. D **8** (2000), 59
- [Buh09] H. Buhr, M. B. Mendes, O. Novotný, M. H. Berg, D. Bing, M. Grieser, C. Krantz, S. Menk, S. Novotny, D. A. Orlov, A. Petrignani, J. Stützel, O. Heber, M. L. Rappaport, D. Schwalm, D. Zajfman, A. Wolf, *Highly excited  $D_2O$  from dissociative recombination of  $D_3O^+$* , Contrib. to ICPEAC 09 (2009)
- [Dah04] L. Dahl, W. Barth, T. Beier, W. Vinzenz, C. Kitegi, U. Ratzinger, A. Schempp, *The Hitrap Decelerator for Heavy Highly-Charged Ions*, Proc. of LINAC 04 (2004), 39
- [Dan94] H. Danared, G. Andler, L. Bagge, C. J. Herrlander, J. Hilke, J. Jeansson, A. Källberg, A. Nilsson, A. Paál, K.-G. Rensfelt, U. Rosengård, J. Starker, M. af Ugglas, *Electron Cooling with an Ultracold Electron Beam*, Phys. Rev. Lett. **72** (1994), 3775
- [Dik88] N. S. Dikansky, V. I. Kudelainen, V. I. Lebedev, V. A. Meshkov, V. V. Parkhomchuk, A. A. Sery, A. N. Skrinsky, B. N. Sukhina, *Ultimate possibilities of electron cooling*, preprint, Institute of Semiconductor Physics, Novosibirsk (1988)
- [Dow09] D. H. Dowell, J. F. Schmerge, *Quantum efficiency and thermal emittance of metal photocathodes*, Phys. Rev. ST Accel. Beams **12** (2009), 074201
- [Drou85] H.-J. Drouhin, C. Hermann, G. Lampel, *Photoemission from Activated Gallium Arsenide*, Phys. Rev. B **31** (1985), 3859
- [Dur96] D. Durek, R. Hoffmann, T. Reichelt, M. Westermann, *The Degradation of a NEA Surface by Poisoning Gases*, Proc. SPIN 96 (1996), 677
- [Eva03] N. J. Evans II, L. E. Allen, G. A. Blake *et al.*, *From Molecular Cores to Planet-forming Disks: An SIRTf Legacy Program*, Publ. Astron. Soc. Pac. **115** (2003), 965
- [Fed06] A. V. Fedotov, B. Gålnander, V. N. Litvinenko, T. Lofnes, A. Sidorin, A. Smirnov, V. Ziemann, *Experimental Studies of the Magnetized Friction Force*, Phys. Rev. E **73** (2006), 066503
- [Fis72] D. G. Fischer, R. E. Enstrom, J. S. Escher, B. F. Williams, *Photoelectron Surface Escape Probability of  $(Ga,In)As:Cs-O$  in the 0.9 to  $\sim 1.6 \mu m$  Range*, J. Appl. Phys. **43** (1972), 3815

- [Gab99] G. Gabrielse, D. S. Hall, T. Roach, P. Yesley, A. Khabbaz, J. Estrada, C. Heimann, H. Kalinowsky, *The ingredients of cold antihydrogen: Simultaneous confinement of antiprotons and positrons at 4 K*, Phys. Lett. B **455** (1999), 311
- [Gor03] V. Gorgadze, T. A. Pasquini, J. Fajans, J. S. Wurtele, *Injection into Electron Plasma Traps*, AIP Conf. Proc. **692** (2003), 30
- [Gri07] M. Grieser, private communication
- [Gus98] A. Gustavsson, M.-E. Pistol, L. Montelius, L. Samuelson, *Local Probe Techniques for Luminescence Studies of Low-Dimensional Semiconductor Structures*, J. Appl. Phys. **84** (1998), 1715
- [Gwi00] G. Gwinner, A. Hoffknecht, T. Bartsch, M. Beutelspacher, N. Eklöw, P. Glans, M. Grieser, S. Krohn, E. Lindroth, A. Müller, A. A. Saghir, S. Schippers, U. Schramm, D. Schwalm, M. Tokman, G. Wissler, A. Wolf, *Influence of Magnetic Fields on Electron-Ion Recombination at Very Low Energies*, Phys. Rev. Lett. **84** (2000), 4822
- [Her06] F. Herfurth, T. Beier, L. Dahl, S. Eliseev, S. Heinz, O. Kester, C. Kozhuharov, G. Maero, W. Quint, *Precision measurements with highly charged ions at rest: The HITRAP project at GSI*, Int. J. Mass Spectrom. **251** (2006), 266
- [Her05] E. Herbst, *Molecular ions in interstellar networks*, J. Phys.: Conf. Ser. **4** (2005), 17
- [Hof09] J. Hoffmann, *Ionic Fragmentation Channels in Electron Collisions of Small Molecular Ions*, dissertation, University of Heidelberg (2009)
- [Hof00] A. Hoffknecht, C. Brandau, T. Bartsch, C. Böhme, H. Knopp, S. Schippers, A. Müller, C. Kozhuharov, K. Beckert, F. Bosch, B. Franzke, A. Krämer, P. H. Mokler, F. Nolden, M. Steck, T. Stöhlker, Z. Stachura, *Recombination of bare  $Bi^{83+}$  ions with electrons*, Phys. Rev. A **63** (2000), 012702
- [Ide94] Y. Ide, M. Yamada, *Role of  $Ga_2O$  in the Removal of GaAs Surface Oxides by Atomic Hydrogen*, J. Vac. Sci. Technol. A **12** (1994), 1858
- [Jan90] G. H. Jansen, *Coulomb Interactions in Particle Beams*, Boston Academic Press (1990)
- [Kam01] M. Kamaratos, *Adsorption Kinetics of the Cs-O Activation Layer on GaAs (100)*, Appl. Surf. Sci. **185** (2001), 66

- [Kam91] M. Kamaratos, E. Bauer, *Interaction of Cs with the GaAs(100) Surface*, J. Appl. Phys. **70** (1991), 7564
- [Kie04] S. Kieslich, S. Schippers, W. Shi, A. Müller, G. Gwinner, M. Schnell, A. Wolf, E. Lindroth, M. Tokman, *Determination of the 2s-2p excitation energy of lithiumlike scandium using dielectronic recombination*, Phys. Rev. A **70** (2004), 042714
- [Kil92] G. Kilgus, D. Habs, D. Schwalm, A. Wolf, N. R. Badnell, A. Müller, *High-resolution measurement of dielectronic recombination of lithiumlike  $Cu^{26+}$* , Phys. Rev. A **46** (1992), 5730
- [Kir67] P. Kirstein, G. Kino, W. Waters, *Space-Charge Flow*, McGraw-Hill (1967)
- [Kos09] S. Koszudowski, *Developments for the HITRAP Cooler Trap and mass measurements around  $A = 96$  at SHIPTRAP*, dissertation, University of Heidelberg (2009)
- [Kra09] C. Krantz, D. A. Orlov, D. Bernhardt, C. Brandau, J. Hoffmann, A. Müller, T. Ricsóka, S. Ricz, S. Schippers, A. Wolf, *Low-lying dielectronic resonances of Fe XXII for accurate energy determination of autoionising Rydberg levels on boronlike cores*, J. Phys.: Conf. Ser. **163** (2009), 012059
- [Kra92] P. Krause, *Temperaturrelaxation in magnetisierten Elektronenstrahlen*, dissertation, University of Heidelberg (1992)
- [Kre05] H. Kreckel, M. Motsch, J. Mikosch, J. Glosík, R. Plašil, S. Altevogt, V. Andrianarijaona, H. Buhr, J. Hoffmann, L. Lammich, M. Lestinsky, I. Nevo, S. Novotny, D. A. Orlov, H. B. Pedersen, F. Sprenger, A. S. Terekhov, J. Toker, R. Wester, D. Gerlich, D. Schwalm, A. Wolf, D. Zajfman, *High-Resolution Dissociative Recombination of Cold  $H_3^+$  and First Evidence for Nuclear Spin Effects*, Phys. Rev. Lett. **95** (2005), 263201
- [Lan89] J. P. Landesman, R. Mabon, G. Allan, M. Lannoo, C. Priester, J. E. Bonnet, *Electronic and Chemical Properties of Hydrogen Exposed GaAs(100) and (100) Surfaces Studied by Photoemission*, J. Vac. Sci. Technol. B **7** (1989), 882
- [Les08] M. Lestinsky, E. Lindroth, D. A. Orlov, E. W. Schmidt, S. Schippers, S. Böhm, C. Brandau, F. Sprenger, A. S. Terekhov, A. Müller, A. Wolf, *Screened Radiative Corrections from Hyperfine-Split Dielectronic Resonances in Lithiumlike Scandium*, Phys. Rev. Lett. **100** (2008), 033001

- [Les07] M. Lestinsky, *High Resolution Electron Collision Spectroscopy with Multicharged Ions in Merged Beams*, dissertation, University of Heidelberg (2007)
- [Lie87] D. Liesen, *Electron Cooling of Heavy Ion Beams*, Phys. Scr. **36** (1987), 723
- [Mae08] G. Maero, *Cooling of highly charged ions in a Penning trap for HITRAP* dissertation, University of Heidelberg (2008)
- [Mag06] S. Nagaitsev, D. Broemmelsiek, A. Burov, K. Carlson, C. Gattuso, M. Hu, T. Kroc, L. Prost, S. Pruss, M. Sutherland, C. W. Schmidt, A. Shemyakin, V. Tupikov, A. Warner, *Experimental Demonstration of Relativistic Electron Cooling* Phys. Rev. Lett. **96** (2006), 044801
- [Mar03] T. Maruysama, D.-A. Luh, A. Brachmann, J. E. Clendenin, E. L. Garwin, S. Harvey, R. E. Kirby, C. Y. Prescott, R. Prepost, *Atomic Hydrogen Cleaning of Polarized GaAs Photocathodes*, Appl. Phys. Lett. **82** (2003), 4184
- [Mat83] S. Matsuo, M. Kiuchi, *Low Temperature Chemical Vapor Deposition Method Utilizing an Electron Cyclotron Resonance Plasma* Jpn. J. Appl. Phys. **22** (1983), 210
- [Men09] M. B. Mendes, H. Buhr, O. Novotný, M. H. Berg, D. Bing, M. Froese, M. Grieser, C. Krantz, S. Novotny, D. A. Orlov, A. Petrigiani, J. Stützel, O. Heber, M. L. Rappaport, D. Schwalm, D. Zajfman, A. Wolf, *Highly excited DCN/CND from dissociative recombination of DCND<sup>+</sup>*, Contrib. to ICPEAC 09 (2009)
- [Mil73] A. G. Milnes, *Deep Impurities in Semiconductors*, Wiley & Sons (1973)
- [NIS09a] The National Institute of Standards and Technology, *Electron Impact Cross Sections for Ionization and Excitation*, <http://physics.nist.gov/PhysRevData/Ionization/Xsection.html> (2009)
- [NIS09b] The National Institute of Standards and Technology, *Atomic Spectra Database*, <http://physics.nist.gov/PhysRefData/ASD/index.html> (2009)
- [Nov] O. Novotný, to be published
- [Nov08] S. Novotny, *Fragmentation of molecular ions in slow electron collisions*, dissertation, University of Heidelberg (2008)
- [Ole80] D. Olego, M. Cardona, *Photoluminescence in Heavily p-doped GaAs. I. Temperature and Hole-Concentration Dependence*, Phys. Rev. B **22** (1980), 886

- [O'Ne85] T. M. O'Neil, P. G. Hjorth, *Collisional dynamics of a strongly magnetized pure electron plasma*, Phys. Fluids **28** (85), 3241
- [Orl09a] D. A. Orlov, C. Krantz, A. Wolf, A. S. Jaroshevich, S. N. Kosolobov, H. E. Scheibler, A. S. Terekhov, *Long Term Operation of High Quantum Efficiency GaAs(Cs,O) Photocathodes using Multiple Re-cleaning by Atomic Hydrogen*, J. Appl. Phys. **106** (2009), 054907
- [Orl09b] D. A. Orlov, C. Krantz, D. Bernhardt, C. Brandau, J. Hoffmann, A. Müller, T. Ricsóka, S. Schippers, A. Shornikov, A. Wolf, *High resolution low-energy dielectronic recombination rate coefficients of berillium-like germanium: QED test bench for two-valence-electron systems*, J. Phys.: Conf. Ser. **163** (2009), 012058
- [Orl07] D. A. Orlov, H. Fadil, M. Grieser, C. Krantz, J. Hoffmann, O. Novotný, S. Novotny, A. Wolf, *Electron Cooling with Photocathode Electron Beams Applied to Slow Ions at TSR and CSR*, Proc. of COOL 07 (2007), 230
- [Orl05] D. A. Orlov, F. Sprenger, M. Lestinsky, U. Weigel A. S. Terekhov, D. Schwalm, A. Wolf, *Photocathodes as Electron Sources for High Resolution Merged Beam Experiments*, J. Phys.: Conf. Ser. **4** (2005), 290
- [Orl04] D. A. Orlov, U. Weigel, D. Schwalm, A. S. Terekhov, A. Wolf, *Ultra-Cold Electron Source with a GaAs-Photocathode*, Nucl. Instr. Methods Phys. Res., Sect. A **532** (2004), 418
- [Orl01] D. A. Orlov, M. Hoppe, U. Weigel, D. Schwalm, A. S. Terekhov, A. Wolf, *Energy Distributions of Electrons Emitted from GaAs(Cs,O)*, Appl. Phys. Lett. **78** (2001), 2721
- [Orl00] D. A. Orlov, V. É. Andreev, A. S. Terekhov, *Elastic and Inelastic Tunneling of Photoelectrons from the Dimensional Quantization Band at a  $p^+$ -GaAs-(Cs,O) Interface into Vacuum*, JETP Lett. **71** (2000), 151
- [Pas96] S. Pastuszka, A. S. Terekhov, A. Wolf, *'Stable to Unstable' Transition in the (Cs,O) Activation Layer on GaAs(100) Surfaces with negative Electron Affinity in Extremely High Vacuum*, Appl. Surf. Sci. **99** (1996), 361
- [Pas96b] S. Pastuszka, U. Schramm, M. Grieser, C. Broude1, R. Grimm, D. Habs, J. Kenntner, H.-J. Miesner, T. Schüßler, D. Schwalm, A. Wolf *Electron cooling and recombination experiments with an adiabatically expanded electron beam*, Nucl. Instr. Methods Phys. Res., Sect. A **369** (1996), 11
- [Pet08] A. Petrigiani, H. Kreckel, M. H. Berg, S. Altevogt, D. Bing, H. Buhr, M. Froese, J. Hoffmann, B. Jordon-Thaden, C. Krantz, M. B. Mendes,

- O. Novotný, S. Novotny, D. A. Orlov, S. Reinhardt, A. Wolf, *Spectroscopy and dissociative recombination of the lowest rotational states of  $H_3^+$* , submitted to J. Phys.: Conf. Ser., preprint: arXiv:0810.0405v1
- [Pfl01] D. G. Pflug, M. Schattenburg, H. I. Smith, A. I. Akinwande, *Field emitter arrays for low voltage applications with sub 100 nm apertures and 200 nm period*, IEEE Electron Devices Meeting 2001 (2001), 8.5.1
- [Pie80] D. T. Pierce, R. J. Celotta, G.-C. Wang, W. Unertl, A. Galejs, C. Kuyatt, S. Mielczarek, *GaAs Spin Polarized Electron Source*, Rev. Sci. Instrum. **51** (1980), 478
- [Pie40] J. R. Pierce, *Rectilinear Flow in Electron Beams*, Appl. Phys. Lett. **11** (1940), 548
- [Pot90] H. Poth, *Electron Cooling: Theory, Experiment, Application*, Phys. Rep. **196** (1990), 135
- [Raz95] M. Razeghi, *The MOCVD Challenge, Volume 2: A Survey of GaInAsP-GaAs for Photonic and Electronic Device Applications*, Institute of Physics Publishing (1995)
- [Sav03] D. W. Savin, S. M. Kahn, G. Gwinner, M. Grieser, R. Repnow, G. Saathoff, D. Schwalm, A. Wolf, A. Müller, S. Schippers, P. A. Závodszy, M. H. Chen, T. W. Gorczyca, O. Zatsarinny, M. F. Gu, *Dielectronic Recombination of Fe XXI and Fe XXII via  $N = 2 \rightarrow N' = 2$  Core Excitations*, Astrophys. J. Suppl. Ser. **147** (2003), 421
- [Sch07] E. W. Schmidt, D. Bernhardt, A. Müller, S. Schippers, S. Fritzsche, J. Hoffmann, A. S. Jaroshevich, C. Krantz, M. Lestinsky, D. A. Orlov, A. Wolf, D. Lukić, D. W. Savin, *Electron-ion recombination of Si IV forming Si III: Storage-ring measurement and multiconfiguration Dirac-Fock calculations*, Phys. Rev. A **76** (2007), 032717
- [Sch65] J. J. Scheer, J. van Laar, *GaAs-Cs: A New Type of Photoemitter*, Solid State Commun. **3** (1965), 189
- [Shor] A. Shornikov, dissertation, University of Heidelberg, to be published
- [Sin06] C. K. Sinclair, *DC photoemission electron guns as ERL sources*, Nucl. Instr. Methods Phys. Res., Sect. A **557** (2006), 69
- [Sin03] C. K. Sinclair, *Very High Voltage Photoemission Electron Guns*, Proc. of the 2003 Particle Accelerator Conf. (2003), 76

- [Spi77] W. E. Spicer, *Negative Affinity 3-5 Photocathodes: Their Physics and Technology*, Appl. Phys. A **12** (1977), 115
- [Spi62] L. Spitzer Jr., *Physics of Fully Ionized Gases*, Second Edition, Wiley & Sons (1962)
- [Spr04] F. Sprenger, *Production of Cold Electron Beams for Collision Experiments with Stored Ions*, dissertation, University of Heidelberg (2004)
- [Ste96] M. Steck, K. Beckert, H. Eickhoff, B. Franzke, F. Nolden, H. Reich, P. Spädtke, T. Winkler, *Suppression of intrabeam scattering in cooled heavy ion beams*, Hyperfine Interact. **99** (1996), 245
- [Stü] J. Stützel, dissertation, University of Heidelberg, to be published
- [Ter02] O. E. Tereshchenko, A. S. Terekhov, D. Paget, P. Chiaradia, J. E. Bonnet, R. Belkhou, A. Taleb-Ibrahimi, *Local-Order of Chemically-prepared GaAs(100) Surfaces*, Surf. Sci. **507** (2002), 411
- [Ter96] A. S. Terekhov, V. L. Alperovich, M. A. Kirillov, D. A. Orlov, A. G. Paulish, I. V. Savchenko, H. E. Scheibler, *Evolution of Surface Electronic Properties of GaAs Photocathodes during Degradation*, Proc. of SPIN 96 (1996), 755
- [Ter95] A. S. Terekhov, D. A. Orlov, *Photoelectron Thermalization Near the Unpinned Surface of GaAs(Cs,O) Photocathodes*, Proc. of SPIE 2550 (1995), 157
- [Tok02] M. Tokman, N. Eklöv, P. Glans, E. Lindroth, R. Schuch, G. Gwinner, D. Schwalm, A. Wolf, A. Hoffknecht, A. Müller, S. Schippers, *Dielectronic recombination resonances in  $F^{6+}$* , Phys. Rev. A **66** (2002), 012703
- [Tsch08] K. G. Tschersich, J. P. Fleischhauer, H. Schuler, *Design and Characterization of a Thermal Hydrogen Atom Source*, J. Appl. Phys. **104** (2008), 034908
- [Tsch00] K. G. Tschersich, *Intensity of a Source of Atomic Hydrogen based on a Hot Capillary*, J. Appl. Phys. **87** (2000), 2565
- [Var67] Y. P. Varshni, *Temperature Dependence of the Energy Gap in Semiconductors*, Physica **34** (1967), 149
- [Wad90] T. Wada, T. Nitta, T. Nomura, M. Miyao, M. Hagino, *Influence of Exposure to CO, CO<sub>2</sub> and H<sub>2</sub>O on the Stability of GaAs Photocathodes*, Jpn. J. Appl. Phys. **29** (1990), 2087

- [Wei04] U. Weigel, *Cold Intense Electron Beams from Gallium Arsenide Photocathodes*, dissertation, University of Heidelberg (2004)
- [Wol00] A. Wolf, G. Gwinner, J. Linkemann, A. A. Saghiri, M. Schmitt, D. Schwalm, M. Grieser, M. Beutelspacher, T. Bartsch, C. Brandau, A. Hoffknecht, A. Müller, S. Schippers, O. Uwira, D. W. Savin, *Recombination in Electron Coolers*, Nuc. Instr. Methods Phys. Res., Sect. A **441** (2000), 183
- [Wol92] A. Wolf, *Wechselwirkung zwischen hochgeladenen Ionen und freien Elektronen in einem Ionenspeicherring: dynamische Reibung und Rekombination*, professorial dissertation, University of Heidelberg (1992)
- [Wol91] A. Wolf, J. Berger, M. Bock, D. Habs, B. Hochadel, G. Kilgus, G. Neureither, A. Müller, U. Schramm, R. Schuch, D. Schwalm, E. Szmola, M. Wagner, *Experiments with Highly-Charged Ions in the Storage Ring TSR*, Z. Phys. D: At., Mol., Clusters **21** (1991), 69
- [Yam94] M. Yamada, Y. Ide, *Direct Observation of Species Liberated from GaAs Native Oxides during Atomic Hydrogen Cleaning*, Jpn. J. Appl. Phys. **33** (1994), 671



# Acknowledgements

The work presented in this text would not have been possible without the selfless help and support I received from many people and which I gratefully acknowledge.

First, I would like to thank Prof. Dr. Andreas Wolf, who accepted me as a doctoral student in his workgroup at the Max-Planck-Institute for Nuclear Physics and allowed me to carry out this work under his wise, cautious and always helpful supervision.

At the same time, I wish to thank Prof. Dr. Thomas Stöhlker, who so kindly and spontaneously agreed to assume the role of second referee for this work.

Many thanks go to Dr. Dmitry Orlov, who guided my steps in day-to-day laboratory life with great enthusiasm and expertise. I never learned more about physics from a single person than in these three years I was allowed to work with him.

I thank my former colleague Dr. Jens Hoffmann for introducing me to the data acquisition system of the Electron Target, and for passing on to me the art of liquid helium cooling of the Target's superconducting coil. I owe much to Dr. Oldrich Novotný who was ready to devote some of his precious  $\text{CF}^+$  beamtime to the cooling force measurements presented in this work. I am thankful towards Prof. Dr. Stefan Schippers and Dr. Eike Schmidt who unveiled the mysteries of the data reduction software TSRalpha to me. I also gratefully acknowledge the help of Dr. Michael Lestinsky in debugging the hyperfine-split fit routine applied to the DR measurements of  $\text{F}^{6+}$ . Special thanks go to my office mate Andrey Shornikov who was always ready to help out in the time-consuming process of photocathode activation.

Dr. Roland Repnow, Dr. Robert von Hahn, Manfred König and their accelerator crew managed to conjure even the most exotic ion species out of their sources and accelerators. And no experiment at the TSR would be possible without the "lords of the ring" Dr. Manfred Grieser and Kurt Horn. To them goes all the credit for storing even the most stubborn of ion beams in the machine.

I wish to thank Karl Hahn and his coworkers at the accelerator workshop for their self-sacrificing support in all those situations where broken pumps, detectors or vacuum flanges had to be repaired “right now”. I thank Oliver Koschorreck for his enthusiastic support with all electronics-related problems. I also thank Volker Mallinger, head of the central institute workshop, for accepting my reluctance to use SolidWorks and my filing of hand-drawn sketches that were not even remotely DIN-compliant.

I greatly appreciate the help by Dr. Frank Köck in configuring Linux on the new data-acquisition backend computer of the Electron Target. The same is true for Rolf Epking’s skillful support with the Windows-NT-based part of the Target control system.

Many thanks go to Julia Stützel who burdened herself with the laborious task of proof-reading this text, a task she fulfilled with great skill and patience. I also wish to thank her for all those recreative conversations at the coffee maker, which, amongst others, made sure my blood caffeine level never dropped below a critical value.

Finally, I thank Fabienne, for her decision to stand at my side, for her caring support along all these years, and for all those things printed words cannot contain.

